ABSTRACT

Title of dissertation: FLUCTUATIONS ON METAL SURFACES AND MOLECULE/METAL INTERFACES

Chenggang Tao, Doctor of Philosophy, 2007

Dissertation directed by: Professor Ellen D. Williams

Department of Physics

We combine the tools of statistical mechanics with direct imaging at the atomic scale, using scanning tunneling microscopy (STM) to observe and characterize intrinsic fluctuation properties on surfaces and interfaces, and further explore how these properties are affected by current, the electromigration problem.

Fluctuation properties of steps and islands on metal surfaces, twin boundaries on metal nanowires, are investigated and the underneath mass transport mechanisms are determined. Then we has studied how mass transport properties are affected by undesirable impurity on surfaces or deposited molecules, especially we focus on island shape change and fluctuations of molecule/metal interfaces. For the organic-metal system, we further investigate related electromigration properties, and find island migration and step bend due to wind force. Finally, organic thin films are also investigated, including the novel 2D chiral structure, and phase boundary fluctuations in an organic thin film.

All these studies not only are important in the fundamental physics, but also provide basic and useful information for designing and building future organic electronic devices.

FLUCTUATIONS ON METAL SURFACES AND MOLECULE/METAL INTERFACES

By

Chenggang Tao

Dissertation submitted to the Faculty of the Graduate School of the
University of Maryland, College Park, in partial fulfillment
of the requirements for the degree of
Doctor of Philosophy
2007

Advisory Committee:
Professor Ellen D. Williams, Chair
Professor Theodore L. Einstein
Professor Janice E. Reutt-Robey
Professor John D. Weeks
Assistant Professor Min Ouyang

Dedication

To my parents: Lamei Duan and Zhuxiang

Acknowledgements

I would like to express my deep appreciation to my research advisor, Ellen Williams, for her guidance and support. She has encouraged me to independently and bravely try a lot of ways in research. She has taught me quite a lot of physics, but perhaps even more importantly she has taught me a way of doing research.

I would like to thank Ted Einstein for his help. When I have unsolved theoretical problems, I always stop by his office. As a "guest" student, I would like to thank Janice Reutt-Robey for many discussions in her group meeting. I thank Min Ouyang for much happy chatting. I also like to thank John Weeks and Mike Fuhrer for their kind help.

I am grateful to have the opportunity to work with research scientists, post-doctoral follows and graduate students in the Williams group, the Einstein group, the Reutt-Robey group and the Weeks group. In particular, I benefit a lot from discussion and collaboration with Tim Stasevich, Dan Dougherty, Alex Bondarchuk, and Tosh Degawa. Especially, I would like to thank Bill Cullen for his help in experiments.

Contents

List of figures

List of tables

Chapter 1 Introduction

1.1 Motivation

As fabrication technology develops, the size of electronic devices already reaches to the nanometer scale. To fabricate devices at this scale, there are two strategies, which are called “top-down” design and “bottom-up” design. “Top-down” design employs a variety of sophisticated lithographic and etching techniques to pattern substrates and circuits often for semiconductor devices. But the conventional lithographic processes become challenging as the feature size decrease to few nanometers. So the other approach, “bottom-up”, was proposed and has made a lot of accomplishment. This “bottom-up” strategy is to build small structures in an opposite way, from the atoms or molecules to a functional system. The building blocks usually include molecules, nanoparticles and nanowires.

For all nanoscale devices, the surface to volume ratio is large. This means the features on surfaces, like steps and islands, can dramatically affect the stability and transport properties of the devices. For sensor devices, surface defects serve as preferring binding and reaction sites for chemically or physically adsorbed molecules or particles. In some extreme cases, for instance, some organic field effect transistors (FETs), in which the active part is the self-assembled molecular monolayer or multilayer, can be tuned the

transport properties by changing the molecular/substrate interface or by controlling the arrangement of molecules in the layer(s).

Since from an economic point of view a practical device should work at room temperature, the thermal effect becomes a big issue at the nanoscale. On surfaces, thermal effects are manifested directly as thermal fluctuations of defects on surfaces, like step and island fluctuations, or phase boundary fluctuations in self-assembled molecular monolayers or multilayers. In principle, thermal fluctuations correspond to the step or phase boundary motion due to mass transport. Usually the size of this type of motion is from several angstroms to a few nanometers, with time constants from picosecond to second. Considering the size of nanoelectronic devices, we can imagine that thermal fluctuations may affect reliability of the devices, change the electrical properties, or even cause device failure. On the other hand, thermal fluctuations also directly contribute signal to transport measurements, like noise.

Researchers in the traditional surface science field have put intense effort on thermal dynamics of metal surfaces. Since the promising next generation of electronic devices are very likely to include hybrid systems such as metal electrodes and organic molecules, (e.g. C_{60} or pentacene), they have recently stimulated the interest of theorists and experimentalists [1, 2]. This trend in applied physics inspires us to focus on thermal fluctuation properties of metal/molecule interfaces and phase boundaries in the organic monolayer or multilayer, taking advantage of the traditional surface science technologies and theories. Furthermore, to study the dynamic properties of the devices at the ON status, we have been applying current through these systems, to investigate the electromigration proplems at atomic resolution. Of course, more ambitious projects are to

explore the explicit connections between the transport properties and the surface structures and dynamics of devices.

Considering the spatial and temporal scale of the fluctuations, scanning tunneling microscopy (STM) is a suitable tool to track interface and phase boundary fluctuations. STM can extract fluctuations as a function of the displacement and time.

As in social science, where history can predict the future; in science, any new discovery is based on the past experimental and theoretical knowledge. At first we should know the theoretical background for thermal fluctuations and related experiments. So in the following sections we will introduce basic theory and then review experimental progress on surface dynamics, especially focusing on those experiments done by STM.

1.2 Surfaces and steps

A surface is a boundary between two macroscopic objects with different properties. In the simple case, we consider crystalline surfaces. Typically a solid sample is far from its macroscopic equilibrium crystal shape (ECS), because slow relaxation of long wavelength modes of the surface motion makes real solids unlikely to reach their equilibrium shape. On the other hand, the slow relaxation of long wavelength modes allows us to apply surface thermodynamics to locally study surfaces, which are “near equilibrium”.

At zero temperature, the ECS for crystalline materials is determined by minimization of the total surface energy. This can be described by lattice models by simply counting the number of neighboring bonds broken for a surface in a given orientation. The Wulff construction gives the solution to how to minimize the overall

surface free energy for the given constraint of constant volume [3, 4]. A useful result of this construction is that the distance of a facet from the center of the ECS is proportional to its surface free energy per unit area

$$R_i = (constant)\gamma_i, \qquad (1.1)$$

where γ_i is the surface free energy per unit area.

For real solids, surfaces are not perfectly flat, due to defects, like steps and islands. For a vicinal surface, now the projected surface free energy is the sum of the surface free energy of the flat surface, γ_0, and the step free energy, β, which is the free energy per unit length to create an isolated step.

At finite temperature, the steps wander and fluctuate due to thermal excitation of kinks and their motion along the step edges. Then the configurational entropy, S_0, should be included into the step free energy

$$\beta = \beta_0 - TS_0, \qquad (1.2)$$

where β_0 is the step free energy at zero temperature. The step free energy decreases with increasing temperature.

In order to reduce the length and kink density, we an easily imagine, a step tends to straighten. To describe this tendency, a measurable parameter, the step stiffness, $\tilde{\beta}$, is introduced. The step stiffness is related to the step free energy by [5]

$$\tilde{\beta} = \beta + \frac{\partial^2 \beta}{\partial \theta^2}. \qquad (1.3)$$

The second term is the energy to bend the step. The relation between the step free energy, the step stiffness and the kink energy have been evaluated analytically for a number of simple lattice models [6].

1.3 Langevin theory for step dynamics

The above thermodynamic arguments provide us basic information about the ECS and those parameters to govern the ECS. But this information can not explain how the equilibrium morphology changes with time. To understand these questions, we need to consider the transport mechanism of individual atoms on the surfaces. In principle, the time dependence can be understood by the surface motion, in terms of mass transport driven by chemical potential difference.

From a continuum perspective, the surface morphology evolution can be considered as changes of the local height due to removing or adding an atom. This local height determines the continuum surface Hamitonian $H[z(x, y)]$. Then the local surface chemical potential can be defined as the free change due to an atom attachment or detachment to the continuum surface, which is given as $(\delta H[z(x,y)]/ \delta z(x,y))\Omega_v$ (Ω_v is the atomic volume).

In practice, it is difficult to use such a 2D Hamitonian to describe general step configurations. Instead, theorists have successfully used a quasi-1D model to write the step free energy in the following form [7-9]

$$H\{x_n\} = \sum_n \int dy[\frac{\tilde{\beta}}{2}(\frac{\partial x_n}{\partial y})^2 + V(w_n(y))], \qquad (1.4)$$

where $x_n(y)$ represents a quasi-1D step and $w_n \equiv x_{n-1}(y) - x_n(y)$. $V(w_n(y))$ is the interaction between two neighboring steps. Considering mass transport along step edges, one case is that the step position changes due to atom attachment or detachment to the step edge (AD). It is straightforward to obtain the corresponding step chemical potential

$$\mu_n(y) \equiv -\Omega_s \frac{\delta H}{\delta x_n(y)} = \Omega_s \left[\tilde{\beta} \frac{\partial^2 x_n}{\partial y^2} + V'(w_n(y)) - V'(w_{n-1}(y)) \right], \qquad (1.5)$$

where Ω_s is the area occupied by an atom, $V'(w)$ is the derivative of the step interaction energy $V(w)$ with respect to the step spacing w. For simplicity, we consider an isolated step, for which the step interaction energy $V(w)$ is zero. Therefore, the local chemical potential $\mu(y)$ is given by

$$\mu(y) = \Omega_s \tilde{\beta} \frac{\partial^2 x}{\partial y^2}. \qquad (1.6)$$

Using linear kinetics, the assumption that the velocity of a step is proportional to the local gradient of the free energy produced by its motion [10], can be used to describe step motion. For the AD case, the local step exchanges adatoms with the neighboring terrace, which serves as a reservoir with constant chemical potential. The local step thus moves according to the chemical potential difference between the step and the reservoir. The arbitrary zero for the step chemical potential is selected such that a straight line has zero chemical potential. Therefore, for the AD case, the chemical potential of the reservoir, μ_{res}, is zero when there is no net attachment or detachment. Thus the step velocity is

$$\frac{\partial x(y)}{\partial t} = \frac{\Gamma_a}{\Omega_s kT} \left[\mu(y) - \mu_{res} \right] = \frac{\Gamma_A \tilde{\beta}}{kT} \frac{\partial^2 x}{\partial y^2}, \qquad (1.7)$$

where Γ_a is the mobility of the step-edge, as defined by Bartelt *et al.* [6, 11].

The AD case is only one of the three extreme cases for mass transport along step edges. At low temperature, the mass exchange between the step edge and neighboring terrace is forbidden due to large Ehrlich-Schwoebel barrier, and thus adatoms can only diffuse along step edges, which is called step edge diffusion limit (SED). For this SED

case, the mass of each terrace is locally conserved and the normal velocity of the step is determined by the gradient of chemical potentials along the step edge

$$\frac{\partial x(y)}{\partial t} = -\frac{\Gamma_h}{\Omega_s kT}\frac{\partial^2 \mu(y)}{\partial y^2} = \frac{\Gamma_h \tilde{\beta}}{kT}\frac{\partial^4 x}{\partial y^4}, \qquad (1.8)$$

where Γ_h is the effective mobility of the step due to atomic motion along the step-edge.

As mentioned at the beginning, at finite temperature, a step fluctuates due to thermal excitation. So step motion is not only determined by the step free energy change as analyzed above, but is also subject to the step-edge fluctuations. Roughly speaking, these two procedures are competing against each other. In order to reduce the step free energy, a step tends to straighten to minimize the number of kinks. On the other hand, the thermal excitation roughens the step edge. In order to take into account this stochastic nature of step fluctuations, a noise terms should be added into the above equations for describing step motion (Eq. 1.7-8). This is the basic spirit of the Langevin theory. Then for the AD case, the Langevin theory can be written as [11]

$$\frac{\partial x(y)}{\partial t} = \frac{\Gamma_a \tilde{\beta}}{kT}\frac{\partial^2 x}{\partial y^2} + \eta. \qquad (1.9)$$

The second term is a noise term. For AD processes, it is easy to imagine that the noise is uncorrelated with zero mean in both space and time. This noise is often called "white" noise, and can be explicitly written as [11, 12]

$$\langle \eta(y,t)\eta(y',t') \rangle = D\delta(y-y')\delta(t-t'). \qquad (1.10)$$

where D is the noise magnitude, which is expected as a constant, but not an independent phenomenological parameter. Similar to the case of a randomly forced Brownian particle, the strength of the random force (corresponding to the noise magnitude here) is proportional to the friction coefficient (corresponding to the step mobility here) of the

fluid in which the particle is suspended [13]. The relation between D and the step mobility Γ_a is $D=2\Gamma_a$. The strict proof can be seen in Bartelt *et al.*'s work [11, 12].

For the SED case, the Langevin formalism can be similarly written as [11]

$$\frac{\partial x(y)}{\partial t} = -\frac{\Gamma_h \tilde{\beta}}{kT}\frac{\partial^4 x}{\partial y^4} + \eta. \qquad (1.11)$$

In the SED case, since mass can only diffuse along the step edge, that means atoms are hopping from one site to another site on the step edge. So the noise must be correlated:

$$\langle \eta(y,t)\eta(y',t') \rangle = -2\Gamma_h \delta(y-y')\delta''(t-t'). \qquad (1.12)$$

Eq. 1.9 and Eq. 1.11 are explicit expressions of the Langevin theory for AD and SED cases respectively, which describe isolated step fluctuations. Basically, this is the theoretical background for most of the experimental analysis in this thesis.

1.4 Review of progress in experiments

Before STM was invented in 1982 [14, 15], there had been a long experimental history to investigate local surface structures. The invention of field ion microscopy (FIM) is the first milestone to analyze the local atomic structures on surfaces [16]. FIM can directly observe free adatoms on a sharp tip surface. But the disadvantage of this technology is the requirement for the shape of the samples, and only few metal can be made into sharp tips. On the other hand, this special shape also limits the investigated area, in which the typical diameter of the tip is less than 50 nm. Due to its near atomic resolution, transmission electron microscopy (TEM) was once used to track atom motions on surfaces, especially for small samples, e. g., nanoparcles [17, 18]. Similar to FIM, in TEM measurement there also is restriction on samples, which need to be thin enough to

let electrons pass through. In addition, an intrinsic problem of TEM measurements for dynamics is that the high-energy electron beam can interfere with the thermodynamical and kinetic properties being measured. Other real space imaging techniques, like scanning electron microscope (SEM) and low-energy electron microscope (LEEM), are often used for many metallic and semiconducting samples. The advantages of these two techniques are that there is no special limitation on samples and that the scan areas can be up to several hundred microns. So especially LEEM is still widely used for surface dynamics and kinetics study [19, 20]. Of course, if we talk about the large scan area, immediately we can realize the main disadvantage of LEEM and SEM is the spatial resolution. The resolution of the best LEEM now is still larger than 10 nm, and the typical resolution of SEM is from 1 to 10 nm.

The invention of STM is a big breakthrough for surface science. It provides surface scientists the ability to "see" individual atoms and molecules on surfaces [21, 22]. Furthermore, due to its weak interaction with surfaces and high speed [23-25], STM is an ideal tool for surface dynamics study. Depending on temperature and studied materials, atom motion on surfaces may be slow or fast compared with the STM recording speed. For the former case, an STM image is the snapshots of the surface structure, and atomic motion can be revealed by analyzing the changes in successive images, or a so-called "movie". In the latter case, the surface structure changes during STM recording of a single image or even a single line. So the STM images (or temporal pseudo-images which will described in detail in the following chapter) include not only the spatial information, but also temporal information. We need to use theoretical models, as described above, to extract the underlying information of diffusion process. For example, by studying the

correlation functions of step fluctuations, we can determine whether the mass transport is determined by periphery diffusion (step edge diffusion, SED case) or by step-edge attachment/detachment (AD case).

For metal surfaces, the atom hopping or attachment/detachment processes (with time constant τ_h and τ_a, respectively) usually are faster than the scan speed, and the observed step edges or islands edges should be frizzy. The first observations of the frizzy appearance were reported by Kuk *et al*. on steps on clean Cu(110) [26], and then confirmed by Wintterlin *et al.* for the same system [27]. Afterward, similar frizzy phenomena were observed on Ag(111) [28, 29], Cu(100) [30], Cu(111) [31] and many other metal surfaces. As we discussed in the preceding theoretical section, there are two limiting cases for step fluctuations, AD and SED respectively. The temporal correlation functions of steps, *G(t)*, which can be directly calculated form temporal pseudo-images obtained by STM, have exponential growth behaviors for both cases, but with different exponents: ½ for the AD case and ¼ for the SED case. Here we give some examples. At room temperature, for steps on Ag(111) and Cu(111), the dominant mass transport mechanism is step edge diffusion [32, 33]. The AD case has been observed for steps along the [110] direction on Au(110) and Ag(110) [34-36]. When temperature changes, we can imagine, for the SED case, adatoms have more energy to overcome the active energy barrier to leave steps, and then the step fluctuations are dominated by attachment/detachment. Thus there is a transition temperature. The transition temperature for steps on Ag(111) is 450 K , and 600 K on Cu(111) [25, 33]. More complete summaries can be found in these two comprehensive review papers [25, 37].

In addition to step edges, edges of monolayer adatom or vacancy islands also appear frizzy. For islands, the mass transport at the edges causes island shape fluctuations and decay. Morgenstern *et al*. observed frizzy island edges and island decay of monolayer islands on Ag(111), due to atomic diffusion [38, 39]. When the island size is small, typically with diameter less than 20 nm, they found the interesting Brownian motion of islands. The equilibrium shape of islands is temperature dependent. At low temperature, islands on (111) and (100) of fcc metals are quasi hexagonal and square respectively, e. g. Cu(111), Ag(111), Cu(100) [31, 40]. At high temperature, the corresponding equilibrium island shape becomes circular. This shape change can be well explained by Wulff construction [41], because the free energy becomes more anisotropic at high temperatures. By quantitatively analyzing the equilibrium island shape and the shape fluctuations, fundamental surface properties, like the kink energy and step stiffness, can be extracted [25, 40].

1.5 Short introduction on electromigration

As summarized above, STM provides a temporal measure of surface morphology, and mass transport mechanism on surface may be decided from measurement of step fluctuations, island-shape fluctuations or island decay. All these studies are intimately related to stability, reliability or even shape control of devices, which are especially important for nanoelectronics. Talking about an electronic device, all these studies are done when the device is at OFF status. Naturally, another important question is what will happen when the device is at ON status. To answer this question leads us to another topic, electromigration, which has a long history, and was once intensively investigated.

Electromigration is the phenomenon that the electrical current biases atom migration. The systematic investigation of electromigration began in 1950s with the development of very large-size integrated (VLSI) circuits. The following useful table summarizes the relation between atom migration and the current directions. (Table from H. Yasunaga *et al.*[42])

Table 1
Comparison of electromigrations (a and c denote the direction towards the anode and cathode, respectively)

Properties	Electromigration		
	In bulk	In film	On semiconductor surface
Direction			
Al	a	a	a or c
Ag	a	a	c
Au	a	a	a
In	a	a	c
Sn	a	a	c
Current density (A/cm^2)	10^4	10^6	10
Electric field (V/cm)	10^{-2}	1	10
Morphology	Damaged		Growth of layer

From this table we can obtain a basic scenario of electromigration. The direction of the "metallic" electromigration is always opposite to the current direction. But on semiconductor surfaces, the mass migration is possible to be along the current direction, or in opposite direction. The reason is, in metal bulks or metallic thin film surfaces, the charge carriers are only electrons, so the wind force is always opposite to the direction of electrical current; but in semiconductor, the wind force has two components, one is hole wind force and another electron wind force, then the mass transport direction depends one both of these components.

It is not difficult to observe the final effect of electromigration since bulk sample or thin films are damaged with large-scale morphology change. More useful but more difficult to investigate is what is happening at the initial stage of electromigration at the atomic scale, and how to track the motion of a few hundred atoms or even a single atom.

Our group has been exploring the problems since the 1990s [43, 44]. These beautiful results have shown how current slows down the step bunching and creates antibands on Si(111) surfaces. As the device size keeps becoming smaller, especially due to the popular applications in organic electronic devices of the nanogaps between electrodes, in recent years we can see the renaissance of study on metallic electromigration [45, 46].

1.6 Organization of this thesis

The above is a brief review on surface dynamics theory, STM study on surface thermodynamics and electromigration. These experimental achievements and theoretical background are the basis of the work in this thesis. As mentioned in the motivation section, our work are not only continues to push further in solving the thermodynamic problems on the traditional metal surfaces, but also connects this to the very important application problem, electromigration, and extend the field to the organic molecule/metal interfaces and phase boundaries in organic self-assembled monolayers, which all are intimately related to those promising near further organic electronic devices. The following is the organization of this thesis.

In chapter 2, we will introduce the scanning tunneling microscopes we have been using for carrying out results in this thesis. The main two STMs for experiments are the variable-temperature STM by Omicron and the JEOL STM. I also modified one of our homemade STMs when I first jointed in our group, through which I will introduce the main functional parts of a STM. In addition, we will briefly summarize other related techniques, such as low energy electron diffraction (LEED) and scanning electron

microscopy (SEM). Some other experimental setups for sample preparation will also be introduced.

In chapter 3, we will discuss thermodynamics on pure metal surfaces, including step fluctuations on Ag thin films and the surfaces of Ag nanowires. Using the steps on Ag(111) surfaces as a statistical model, we will address the challenging problem, generalized survival, which is closely related to the reliability of materials and devices in nanoscale. Then we will introduce the thermodynamic properties on surfaces of Ag nanowires. We have determined the morphology of Ag nanowires, and revealed the mechanism governing the mass transport on Ag nanowire [47, 48].

In chapter 4, we will extend the thermodynamic study from the metal surface to a more complicated system, molecule/metal interfaces. At first, we will characterize how C_{60} molecules affect the neighboring bare step fluctuations. The main part in this chapter is the dynamics of C_{60}/Ag interfaces, which can be considered as a prototype of the molecule/electrode interfaces in any future devices using organics molecules as the active parts [49-51].

In chapter 5, we will talk about the self-assembled monolayers of C_{60} and acridine-9-carboxylic acid (ACA). We found a chiral structure formed by these two components on Ag(111) due to C_{60} crystallizing the 2D gas phase of ACA molecules. The ordered/disordered (2D gas) phase boundaries also fluctuate at room temperature. We have characterized the thermodynamic properties [52, 53].

In chapter 6, we will discuss how current affects the mass transport on metal surfaces and molecule/metal interfaces. We have pushed our work further to track the

biased motion of a single pit, single monolayer island, and single decorated steps due to the applied current.

In chapter 7, I will summarize the thesis and suggest some possible future work.

Chapter 2 Observation of fluctuations with scanning tunneling microscopy

In order to characterize step and phase boundary fluctuations, it is necessary to develop a technique to observe the motion of step edges or phase boundaries real time. As mentioned in Chapter 1, typically the motion is at atomic scale, so it requires the experimental tool has at least nanometer resolution. On the other hand, for thermal dynamical processes, the measurement should not disturb the objects; or in a practical way, the effect due to the measurement can be ignored. Thanks to its high resolution and weak interaction with the surfaces, scanning tunneling microscopy (STM) is a suitable tool for this task.

In this chapter, we will first introduce STM, including the basic principle and the brief history of STM development. Then we will describe the experimental setups for all the experiments discussed in the following chapters.

2.1 Introduction to scanning tunneling microscopy

STM was invented by G. Binnig and H. Rohrer in 1982 at IBM's lab in Zurich [14, 15], for which they shared the 1986 Nobel Prize in physics. This invention opened a door to explore surfaces at atomic level in real space.

The basic structure of STM is illustrated schematically in Fig. 2.1. The instrument consists of a sharp conducting tip which is scanning with respect to a flat conducting surface. When a voltage V is applied between tip and sample, a current will flow through

the gap between tip and sample due to the quantum tunneling effect, and this current can be measured as a function of (x, y) location, and then a 3D image z(x, y) of the surface can be recorded.

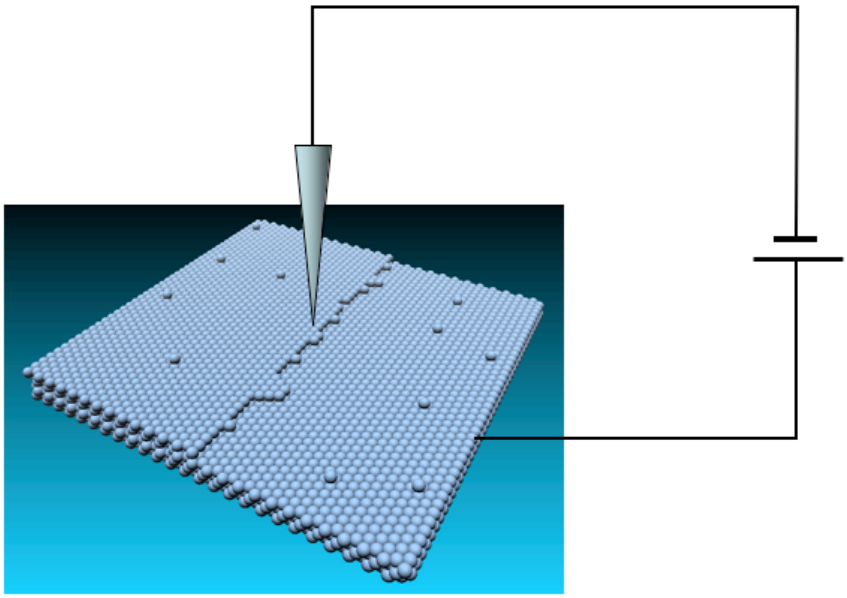

Fig. 2.1 Schematical illustration of the STM.

In order to understand the STM images, at first we need to know how to calculate the tunneling current. For simplicity, we consider only metal tips and metal surfaces. Then this is a question to calculate the tunneling current through metal-insulator-metal junctions. The most extensively used theory for this is the time-dependent perturbation approach developed by Bardeen in 1961 [54]. The presumptions of Bardeen's approach are (1) the distance between the tip and the sample is small enough that there is overlap between the tails of their density of states, (2) the distance is also large enough to make the overlap weak and both sides have their own independent density of state which is not affected by this weak overlap, (3) in the tunneling barrier each of their wavefunctions falls exponentially to zero. Then the tunneling matrix M is determined by a surface

integral on a separation surface between the tip and the sample

$$M = \frac{\hbar}{2m}\int dS \bullet (\chi^* \nabla\psi - \psi^* \nabla\chi), \qquad (2.1)$$

where χ and ψ are the wavefunctions of the tip and the surface respectively. Then the rate of electron transfer is determined by the Fermi golden rule [55]. With a negative sample bias $-V$, the probability of an electron in the state χ at energy level E_χ from the tip tunneling to a state ψ at energy level E_ψ of the surface is $\frac{2\pi}{\hbar}|M|^2 \delta(E_\chi - eV - E_\psi)$. The tunneling current is the sum of electron transfer from all the states. Explicitly, with a sample bias –V, the total tunneling current is calculated as [56]

$$I = \frac{4\pi e}{\hbar}\int \left[f(E_F - eV + \varepsilon) - f(E_F + \varepsilon) \right] \rho_s(E_F - eV + \varepsilon)\rho_t(E_F + \varepsilon)|M|^2 d\varepsilon, \qquad (2.2)$$

where $f(E) = \frac{1}{1 + e^{\frac{E - E_F}{k_B T}}}$ is the Fermi distribution function, and ρ_s and ρ_t are the local density of state (DOS) of the tip and the surface respectively. Using a low temperature approximation for the Fermi distribution function, simply a step function, and according to Bardeen's formula, the tunneling matrix element does not change, so Eq. (2.2) can be simplified as:

$$I = \frac{4\pi e}{\hbar}|M|^2 \int_0^{eV} \rho_s(E_F - eV + \varepsilon)\rho_t(E_F + \varepsilon) d\varepsilon. \qquad (2.3)$$

Assuming the vacuum barrier is a square barrier, the bias is very small compared with the sum of the work functions of the tip and the sample (ϕ_s and ϕ_t), and then using a WKB approximation, the tunneling matrix can be written as [56, 57]

$$|M|^2 = e^{-2s\sqrt{\frac{2m}{\hbar}\left(\frac{\phi_s + \phi_t}{2}\right)}}. \qquad (2.4)$$

Finally, we evaluate the tunneling current as following

$$I \approx \frac{4\pi e}{\hbar} e^{-2s\sqrt{\frac{2m}{\hbar}\left(\frac{\phi_s+\phi_t}{2}\right)}} \int_0^{eV} \rho_s(E_F - eV + \varepsilon)\rho_t(E_F + \varepsilon)d\varepsilon. \qquad (2.5)$$

From this simplified Bardeen formula, we can clear see that the tunneling current is determined by the distance between the tip and the surface, the DOS of the tip and the surface. Using a *s*-wave-model proposed by Tersoff and Hamann [58, 59], the DOS of the tip is a constant (*s* wave), it is straightforward to obtain the DOS of the surface by differentiating Eq. (2.5)

$$\frac{dI}{dV} \propto \rho_s(E_F - eV). \qquad (2.6)$$

dI/dV is just the dynamic tunneling conductance. Thus, it is proportional to the local density of state (LDOS) of the surface.

From this theory background, we know the tunneling current is a function of the bias voltage *V*, and the distance between the tip and the surface, *s*. In practice, we can use a feedback loop to keep the tunneling current constant at a fixed bias V by controlling the distance *s* as a constant. To keep the distance *s* constant, technically we can use a *z* (meaning the direction vertical to the surface) piezo to control position of either the tip or the sample. By recording the voltage of the *z* piezo as a function of (x, y), we can map the height of the surface. To strictly understand the height here, we need to consider the density of state of the measured surface and the tip. For metal surfaces, the dominating tunneling current are from the delocalized *s* or *p* surface states, we can intuitively to understand the 'bumps' or 'holes' in the topography image as the presence or absence of surface atoms. But we need to keep in mind that this understanding is not always true, especially for semiconductor surfaces, where STM measured the dangling bands of the

surface atoms.

2.2 STM setups

From the above theoretical introduction, we know in principle how a STM works, but there are a lot of experimental details needed to know in order to build and operate a real STM. In this section we will introduce each functional parts of a STM via the home-built STM, which I spent first few month in our lab to fix. Then we will introduce two commercial STM: Omicron VTSTM and JEOL SPM 4500A.

2.2.1 STM structure

Fig. 2.2 shows the home-built STM body. In this picture, we can see the main mechanical structure and components of a STM: a tip, a scanner and an inchworm. These three pieces are main parts of a STM. Together with a sample holder, all these components are mounted on a large copper block, which can be suspended from springs during operation. In the order of distance to the sample, we will introduce all these components.

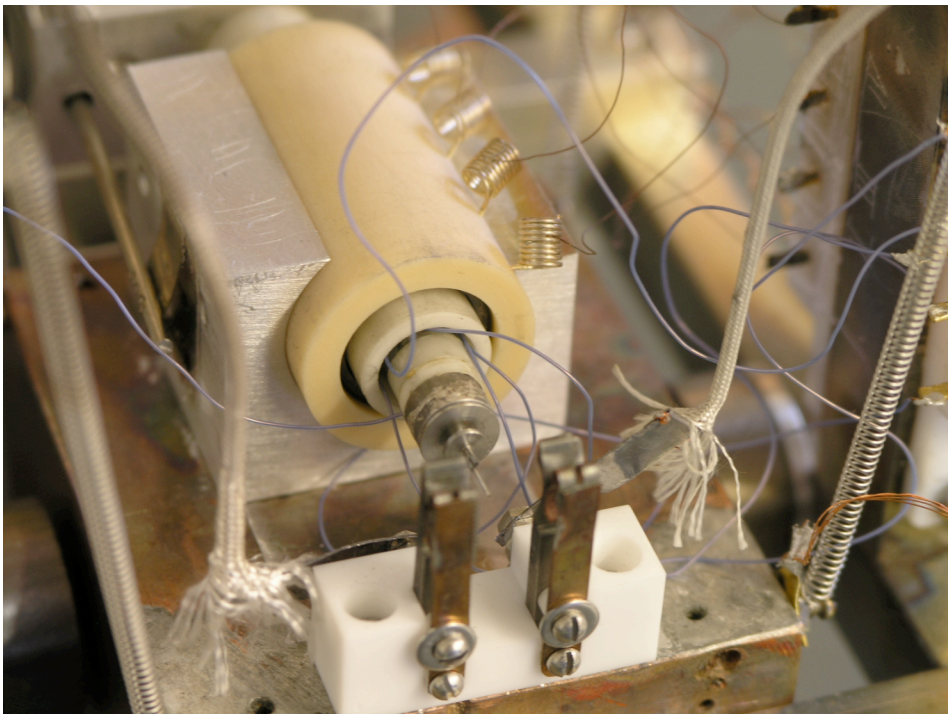

Fig. 2.2 Home-built STM

Since the basic signal of STM is the tunneling current between the tip and the sample surface, the geometry and chemical identity of the tip is crucial for a STM, which influence both topographic and spectroscopic measurements. For an ideal tip, there is a single metallic atom on at the sharp end. But in practice it is extremely difficult to control down to a few atoms. Fortunately in experiments even some rugged or dull tips could obtain pretty decent topographic images. This is duo to the strong dependence of the tip-sample distance. According to the tunneling theory in preceding sections, with a typical work function of 4 eV for metal, the tunneling current increases by a factor of 10 when the tip-sample distance decreases by 1 Å. So it is possible one atom at the apex of the trip contributes most of the tunneling current since the typical lattice constant of metal is about 3 Å (3.16 Å for W). Of course, this also requires atomically flat sample surfaces. In our experiments, the measured objects are steps, big molecules (for instance, C_{60}) and 3D

structures (nanowires), to avoid "double tip" effect, so we need high-quality tips, not only sharp, but also robust.

The most common materials of STM tips are tungsten or platinum-iridium, due to their hard, refractory and easy to fabricate properties. Platinum-iridium is advantageous in air because it does not oxidize. To test the home-built in air, platinum-iridium tips were often used. However, tungsten is most commonly used in UHV, since it is relatively inexpensive and easily etched to produce the desired tip shapes. In the VTSTM system, most tips are tungsten. For fabricate a tungsten tip, in our lab, following instructions from A. Melmed, we typically roughly etch a straight tungsten wire in 2 M KOH solution with a carbon counter electrode at about 6 VAC bias to generate a tip cone. The next step is to finely etch the tip using a similar (3-5 VAC) voltage but with a 0.5 N solution of KOH. Like blowing a bubble, the solution is suspended in a fine loop of Pt wire. The loop is moved forward over the end of the tip under an optical microscope. The etching voltage is applied during the loop is moved backward. After fine etching the tip is rinsed in very clean (HPLC grade) water for about 20 seconds. After this procedure, the tungsten tip is transfer into the UHV chamber. Before using it to scan a surface, we usually use an electron beam to remove the "wet" oxide layer covering the tip. The similar procedure can also be used to fabricate platinum-iridium tips.

In order to obtain a topographic image, a device is needed to move the tip across the sample surface while controlling the tip-sample distance. This device is called a scanner. The requirements of a good scanner are: (1) high resolution – the necessary resolution is less than 1 Å in the lateral direction and 0.01 Å in vertical direction; (2)

orthogonality – movement of each of the three axes should be independent; (3) linearity – the amount of movement should be proportional to the applied voltage; (4) mechanical rigidity – a rigid scanner will have a high resonant frequency, which is desirable for both vibration isolation and feedback performance; and (5) large range – to cover as large a sample area as possible [60].

Piezoelectric materials meet these requirements. The commercial piezoelectric ceramic PZT is used in most STM scanners. The geometries of scanners can be bar or tube. For comparable mechanical strength, the thickness of the tube wall can be thinner than the thickness of a bar. Therefore, a smaller voltage is necessary for the same piezo displacement with a tube than with a bar. Other advantages of a tube are high sensitivity, high resonant frequency, compact and simple structure. So the single piezoelectric tube scanner has become most popular. As shown in Fig. 2.2, the home-built STM employs a tube scanner (PI Ceramic). Fig. 2.3. shows the single piece. There are four electrodes outside to actuate lateral motion (X, Y directions) and an inside electrode to actuate vertical motion (Z direction). In Z direction, the relation between the displacement and the applied voltage is

$$\Delta Z = d_{31} l \frac{V}{d}, \qquad (2.7)$$

where l is the tube length, d the wall thickness and d_{31} the strain coefficient. The typical value of d_{31} is ~ 1×10^{-10} m/V. The lateral displacement is proportional to l^2V/dD, where D is the tube diameter.

Fig. 2.3 Piezoelectric tube scanner

In order to perform scanning, at first the tip-sample distance should be in the tunneling region. This can be achieved by moving either the tube scanner (on wich the tip mounted) or the sample. In the home-built STM, we use the first strategy: use a clamp-step device to position the tip close into the tunneling distance from the sample, which is fixed. The clamp step device is often called an inchworm (Burleigh), as shown in Fig. 2.4. There is a large white cylinder outside, which is a large piezoelectric body. Inside there are two piezoelectric cramps holding a ceramic shaft, on which the scanner is mounted. The shaft "walks" likes an inchworm: clamping the front end of the shaft, expanding the body, clamping the rear end while leasing the front end, and then contracting the body. The shaft moves forward step by step. Of course, changing the clamping order, the shaft can move backward. In this way, the tip on the scanner can be positioned into the tunneling region. There are two other types of devices to position the tip or the sample: stick-slip and screw, which will be introduced in detail when we introduce the commercial VTSTM and JEOL SPM in the following sections.

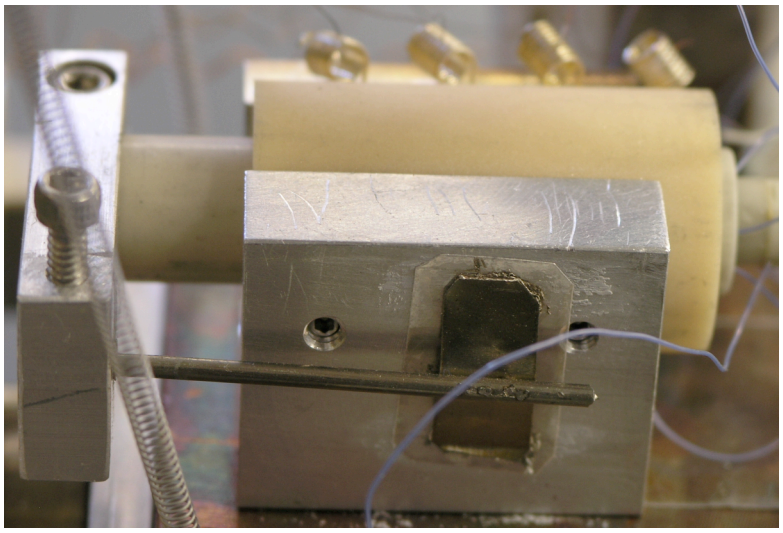

Fig. 2.4 Inchworm

In Fig. 2.2, we can see that the whole STM stage and the sample holder are mounted on a copper block, which is suspended by springs. This design is for vibration isolation. Considering the resolution and sensitivity of STM, the problem of isolating the microscope from vibrations in the external world should never be underestimated.

A typical lowest resonant frequency of a UHV STM is between 1 and 2KHz. So the vibration isolation stage must have a resonant frequency of less than a few Hertz. Given the floor vibration amplitude is a few thousand angstroms and the resolution in the vertical direction of a STM is ~ 0.01 Å, we need a vibration isolation factor of at least 10^{-5}. A spring suspension stage can meet this requirement. In addition to a spring suspension stage, there is a magnet damping applied in the STM. Even hardly seen in Fig. 2.2, in fact there are strong rare-earth magnets attached to the stationary frame near the copper block. If the copper block moves in any direction, the magnets induce eddy currents in the block that provide excellent damping for low-frequency vibrations which can not be effectively damped by a spring suspension stage. This combination system of spring suspension and

magnetic damping is very popular in STMs. The Omicron VTSTM also uses this type of vibration isolation systems.

Above mechanical parts are basic blocks for a STM. In order to coordinate them into a system, carefully designed control electronics is needed. A block diagram of the circuit of the home-built STM is shown in Fig. 2.5.

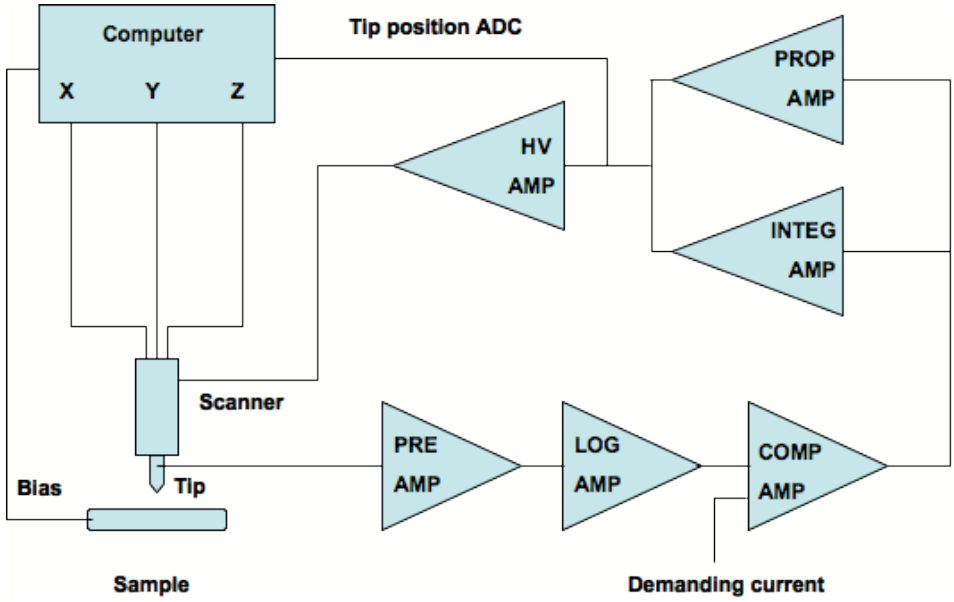

Fig. 2.5 Block diagram of STM circuit

After approaching the tip close to the sample in the tunneling distance, the tunneling current is measured by a preamplifier, which is adjustable from 10^6 to 10^9 V/A in the RHK controller (RHK SPM 100). As we talked in the theoretical part, the tunneling current is exponentially dependent on the distance between the tip and the sample, and then it can be linearized by a logarithmic amplifier to improve the dynamic range. The measured tunneling current is then compared with a demanded current, which is an important adjustable parameter. The resultant error signal is sent back to the feedback amplifiers, usually consist of a proportional amplifier and an integral amplifier.

The feedback signal finally fed back into a high-voltage amplifier, which generate a amplified voltage signal to control the Z (vertical) motion of the scanner (the tip). One point needed to point out is: in the STM feedback system, the familiar PID feedback loop system is not used, because the differential amplifier can cause instabilities. More detailed discussions can be found in J. A. Stroscio or C. J. Chen's books [56, 60].

2.2.2 Omicron VT STM

As mentioned in the first chapter and at the beginning of this chapter, most of the fluctuation measurements have been done in the Omicron VT STM system. Fig. 2.6. shows the whole STM stage.

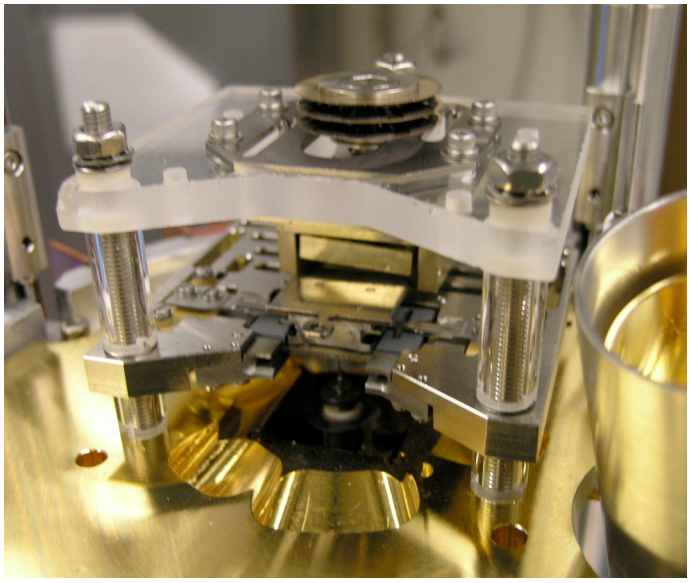

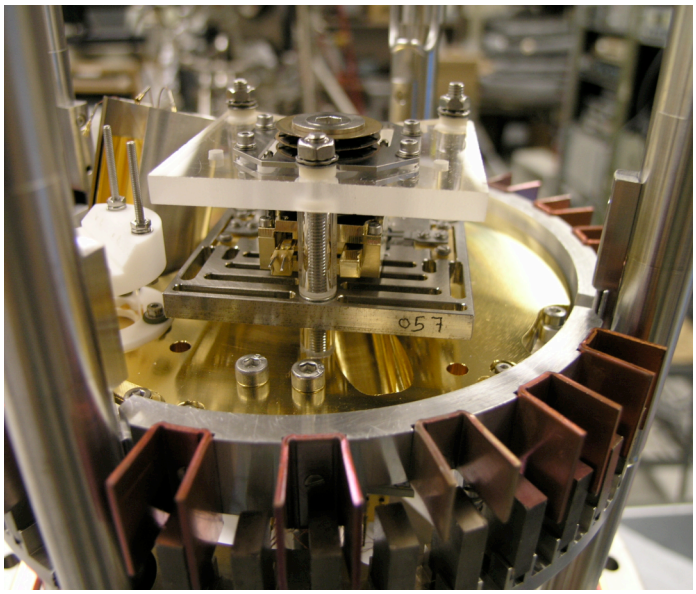

Fig. 2.6 VT STM system

Omicron VT STM also uses the same vibration isolation design like the home-built STM: a spring suspension with magnetic damping. The tip mounted on the tube scanner faces up while the sample surface facing down. The main difference from the home-built STM in the mechanical structure is the device for tip positioning. Here a stick-slip inertial stage is employed to approach the tip close to the sample. The mechanism of the stick-slip stage is that the scanner rests on a piezoelectric plate, then a sawtooth signal is applied to the piezoelectric plate so that the plate slowly moves the scanner up and then the piezoelectric plate quickly retracts so that the scanner slips across the plate. The scanner (with the tip) will approach to the sample surface by repeating this process.

Since it is a variable temperature instrument, the main advantage is that we can do our measurements at different temperature (25 K to 1400 K according to manufacturer specifications). We can heat samples to elevated temperature by direct or indirect heating.

2.2.3 JEOL SPM

Most electromigration experiments have been carried out on the JEOL 4500 SPM, as shown in Fig. 2.7. This system is more complicated than the home-built STM and the VTSTM, because it includes not only STM, but also AFM. So its design is also quite different from the other two STM systems. Its vibration isolation consists of a large air table on which the vacuum chamber is mounted. In the UHV chamber, the tip and the sample are supported by viton stacks. Because the viton stacks are stiffer than springs, they can not isolate vibration so efficiently as springs. This is the reason that the whole UHV system is mounted on a large air stable, which provides a low resonant frequency (<1 Hz) and the amplification near the resonant frequency is small. In addition, the sample itself is mounted on the end of the tube scanner while the tip remains stationary to allow for optical detection of the deflection of an AFM cantilever in the AFM model. The tips are cantilevers with tips coated by Ti-Pt (MikroMasch, NSC15/Ti-Pt), which can be used in both STM and AFM models.

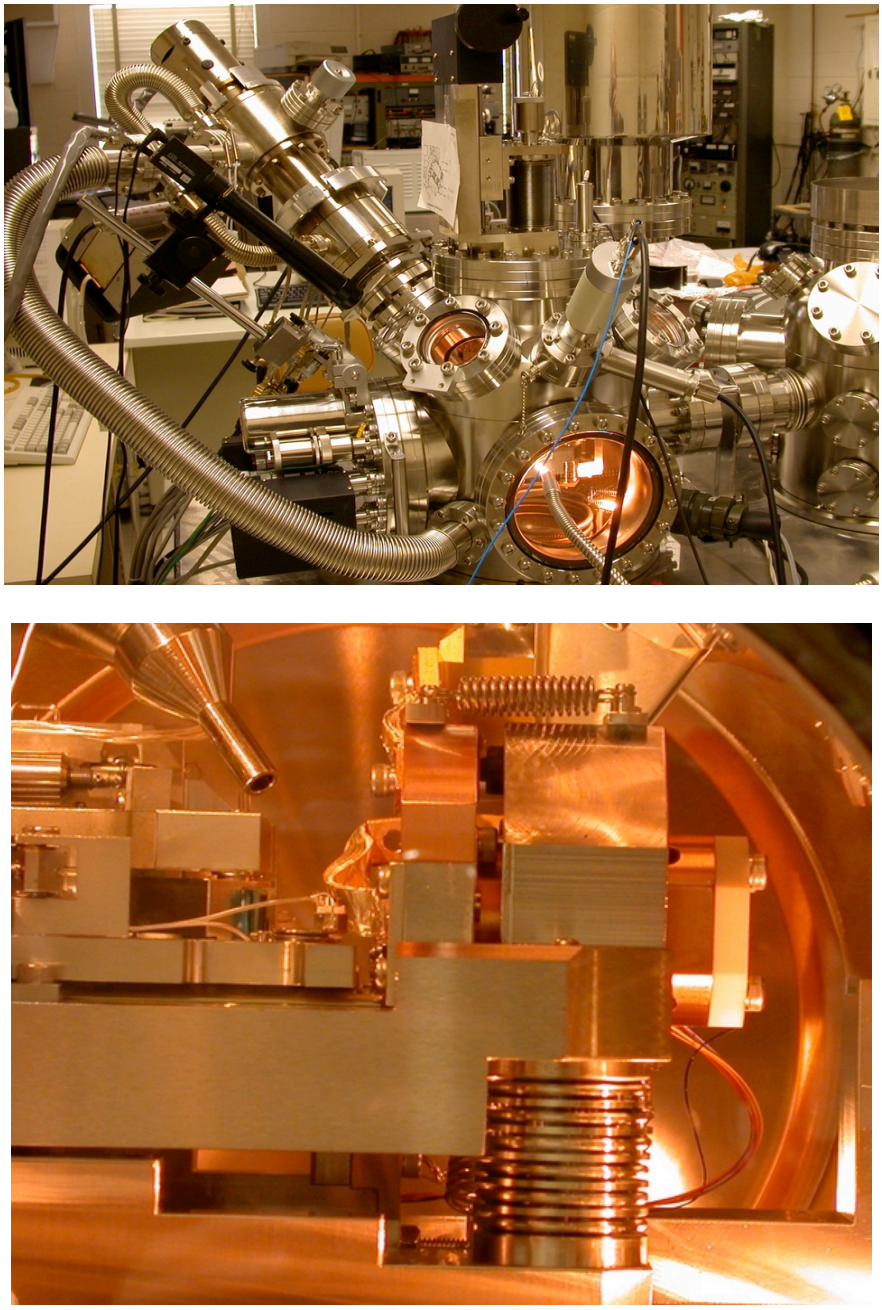

Fig. 2.7 JEOL SPM

2.3 Other experimental setups

Other main instruments used in experiments are SEM, LEED and Auger. SEM is

mounted onto the STM chamber of the JEOL SPM system, which is used to characterized the surfaces and localize the STM tip, which be introduced in details in Chapter 6. LEED and Auger are with the Omicron system to character the quality of the substrates. For preparing the Ag thin films, we developed a small evaporation chamber as shown. Another deposition setup is a thermal effusion system for C_{60} and other molecules deposition. For our Ag nanowire experiments (Chapter 3), we also developed a liquid deposition system. All these experiments will be introduced or mentioned in the following chapters.

Chapter 3 Fluctuations on bare metal surfaces

In this chapter, we will discuss the step fluctuations on bare metal surfaces. In the first section we develop the concept of the generalized survival probability using steps on Ag(111) as a model. The second section will focus on the pinned steps on Ag(111), through which the correlation length are directly measured, and an alternative way to measure the step stiffness is proposed. The third section is our STM study on Ag nanowires. According to our knowledge, this is the first time to use STM to directly image the topography of metal nanowires and characterize related dynamic properties. Part of these works have been publish in Physics review E (*Chenggang Tao, W.G. Cullen, E.D. Williams, C. Dasgupta, Generalized survival in step fluctuations, Phys. Rev. E 76, 021601 (2007)*) and Surface Science (*Chenggang Tao, W. G. Cullen and E. D. Williams, Surface morphological evolution and step fluctuations on Ag nanowires, Surf. Sci. 601, 4939 (2007)*).

3.1 Step fluctuations on Ag(111) surfaces (generalized survival)

I. Introduction

The stability of nanometer scale materials and devices is a fundamental and challenging issue [61-65]. A key problem associated with nanoscale stability is random

stochastic interface dynamics, which can be directly observed in fluctuations of crystal-layer boundaries (steps) [25, 66-70]. Such fluctuations can be evaluated using correlation function approaches, however additional information is available by considering first-passage questions [71], such as the temporal persistence probability *P(t)* and survival probability *S(t)*. Recently, first passage concepts have been applied to a variety of different problems, including ion channels in biology, single molecule electron transfer, etc [72-75]. In addition, the fluctuations of line boundaries where a surface changes height by one crystalline layer (steps) have previously been used as tests of theoretical predictions for persistence probability and survival probability [76-82]. Here we will address generalizations of the survival concept to include issues of first passage to arbitrary locations. The motivation for addressing this concept is the potential for applications in which nanoscale structures may fluctuate to the point where a change in properties or other switching behavior may occur.

The definition of survival probability *S(t)* is the probability of the step edge ***not*** returning to the fixed average step position within a given time interval *t*. Both theoretical and experimental studies have shown that the survival probability *S(t)* decays exponentially at large times, $S(t) \sim exp(-t/\tau_s)$, where τ_s is the survival time constant, which is directly proportional to the correlation time τ_c [83, 84]. To generalize this analysis, the return position can be shifted from the average position to an arbitrary reference position *R*. In this case, the generalized survival probability *S(t, R)* can be defined as the probability that the step position is initially beyond the pre-assigned reference position *R* (−*R*) and remains there (does not relax) over a given time interval *t* [85], as schematically drawn in Fig. 1. Similar to the survival probability, the generalized

survival probability also is predicted to have a long time exponential behavior, $S(t, R) \sim exp(-t/\tau_s(R))$, where $\tau_s(R)$ is the generalized survival time constant [85]. Herein, our experimental results of step fluctuations on Ag(111) observed by time dependent scanning tunneling microscopy (STM) confirm this prediction, and provide a generalization of the scaling form of the generalized survival that can be used to predict the survival properties of step fluctuations at different temperatures. Furthermore, we introduce a contrasting concept, noted as the generalized inside survival $S_{in}(t, R)$, the probability of the step position remaining between the pre-assigned reference positions R and $-R$. Correlated experimental and numerical investigation of this concept show distinctly different behavior than for the generalized survival.

II. Experimental and numerical procedures

The experimental process to make Ag films on freshly cleaved mica substrates has been reported previously [32, 86, 87]. The thickness of the Ag films used in this work is some 500 nm. After several sputtering and annealing cycles in a UHV chamber (base pressure $< 5 \times 10^{-10}$ torr), atomically clean Ag(111) surfaces are obtained, as determined by Auger, LEED and STM. Under proper annealing conditions, the width of flat (111)-oriented terraces can be larger than 1 μm, and step density is quite low, as shown in Fig. 2.

Following cleaning, the samples are transferred to a commercial variable temperature STM (Omicron) in the same UHV chamber, where temperature is controlled with a PBN heater. Step fluctuations are observed in real time by scanning the tip over a fixed position on the step edge in the direction perpendicular to the step orientation. The

typical tunneling current is 0.07 to 0.10 nA, and sample bias −1.60 to −1.70 V, chosen to insure that tip-sample interactions do not modify the step fluctuations [23, 25, 32]. For each temporal pseudoimage, the scan time interval δt between scan lines is 51.2 ms, and the total measurement time t_m is 102.4 s with 2000 lines. The pseudoimages are presented in Fig. 3. Ten to twenty pseudoimages are measured to obtain the data set at each different temperature. The temporal motion of the step edge, the step-edge position $x(t)$, is extracted from each line scan after flattening the upper or lower terrace in the image. The step edge is identified as the point at which the surface height is midway between the heights of the upper and lower terraces. The individual $x(t)$ data sets are used to calculate the distribution of displacements, the temporal correlation, autocorrelation and survival functions, and here the reported functions are averaged over ten to fifteen individual data sets. Measurements were performed in the temperature range from 300 K to 460 K by indirectly heating samples using the PBN heater.

We have also studied the behavior of the generalized survival probability $S(t, R)$ and the generalized inside survival probability $S_{in}(t, R)$ by carrying out numerical integrations of the one dimensional Edwards-Wilkinson (EW) equation (dynamical exponent $n = 2$) and the conserved-noise fourth order Langevin equation ($n = 4$). Since the experimental observations indicate that the model with $n = 4$ is appropriate for the systems studied here (see below), we present herein the results obtained for this model. Simulation results for the generalized inside survival probability for the non-conserved EW equation with $n = 2$ will be reported elsewhere [88].

The spatially discretized, dimensionless form of the Langevin equation used in the numerical work is

$$\frac{dx_i}{dt} = -\left(x_{i-2} - 4x_{i-1} + 6x_i - 4x_{i+1} + x_{i+2}\right) + \eta_i(t), \qquad (1)$$

where $x_i(t)$ represents the step position at lattice site i at time t, and $\eta_i(t)$ are random variables with zero mean and correlations given by $\langle \eta_i(t)\eta_j(t')\rangle = \delta_{t,t'}[2\delta_{i,j} - \delta_{i,j+1} - \delta_{i,j-1}]$. For a system of L sites with periodic boundary conditions, the equilibrium width is then given by $w^2(L) = L/24$, and the correlation time in the long-time equilibrium state is $\tau_c(L) = (L/2\pi)^4$. The simulations were done for $L = 200$; some results were also obtained for $L = 100$ and $L = 400$. Starting from a straight step profile ($x_i = 0$ for all i), the system was equilibrated by carrying out the time integration for a sufficiently long period, and the resulting equilibrated configuration were used as the starting point of further time integration for calculating the generalized survival probabilities. Since the noise is conserved, the average step position $\bar{x} \equiv \left(\sum_{i=1}^{L} x_i\right)/L$ remains equal to zero at all times and there is no need to subtract it from $x_i(t)$ to define the instantaneous step displacement from the average value. The results for the survival probabilities were obtained from averages over 10^4 independent runs.

III. Results and analysis

As described in the experimental section, the step-edge position $x(t)$ can be extracted from the measured pseudoimages such as those shown in Fig. 3. Given $x(t)$ we can directly calculate the temporal correlation functions $G(t)$ [66],

$$G(t) = \left\langle \left(x(t) - x(0)\right)^2 \right\rangle = \left(\frac{2\Gamma\left(1 - 1/n\right)}{\pi}\right)\left(\frac{kT}{\tilde{\beta}}\right)^{\frac{n-1}{n}} \left(\Gamma_n t\right)^{\frac{1}{n}}, \qquad (2)$$

where Γ_n is the step mobility and $\tilde{\beta}$ the step stiffness. The simulations (Eq. 1) are carried out at a fixed value of $\Gamma_n \tilde{\beta} / kT$. Since the step stiffness $\tilde{\beta}$ depends on both temperature and step orientation [49], we measure only steps oriented along the close-packed direction. The measured correlation functions consistently grow as $t^{1/n}$ with $1/n$ close to 1/4, indicating that the step edge fluctuations are dominated by periphery diffusion in this temperature range, as expected from previous reports [23, 25, 32]. The pseudoimages in Fig. 3 also clearly reveal a strong increase in fluctuation amplitude with temperature. The average step width $w = \sqrt{\left\langle \left[x(t) - \bar{x} \right]^2 \right\rangle}$ is 0.136 ± 0.007 nm at 300 K, and about seven times larger, 0.908 ± 0.043 nm at 460 K. (The stiffness $\tilde{\beta}$ is a decreasing function of temperature.) If the step configuration is equilibrated, the distribution of step displacements, $x(t)$ is expected to be Gaussian with a width equal to the equilibrium step width [11, 89]. This is confirmed experimentally, as shown by the distribution of step displacements at 460 K in Fig. 4, which has an equilibrium width 0.930 ± 0.010 nm, the same as the directly calculated step width above.

The survival probability is related to the autocorrelation function [90],

$$\begin{aligned} C(t) &= \langle [x(t_0 + t) - \bar{x}][x(t_0) - \bar{x}] \rangle_{t_0} \\ &= C(0)\left(\left(e^{-t/\tau_c} \right) - \Gamma\left(\frac{3}{4}, \frac{t}{\tau_c} \right) \left(\frac{t}{\tau_c} \right)^{1/4} \right), \end{aligned} \tag{3}$$

where τ_c is the correlation time, which is related to the effective system size as $\tau_c = kT\left(L_{eff} / 2\pi \right)^n / \Gamma_n \tilde{\beta}$. The first term in Eq. 3 becomes dominant when t is large, so the long time behavior of correlation functions is an exponential decay. The measured autocorrelation function data are well fitted by the form in Eq. 3 [32], and for the data

presented here yield correlation times τ_c, equal to 11.8 ± 4.9 s at 300 K and 15.1 ± 5.9 s at 460 K. This is consistent with the previous observation of measurement-time limited correlation time of $\tau_c = t_m / A = t_m / (9 \pm 4)$ [32]. The measurement time dependence arises from the increase in the time constant for fluctuations of increasing wavelength. Only those wavelengths with time constant substantially less than the measurement time are properly sampled. The longest properly sampled wavelength sets the effective system size and thus the correlation time [32]. Using the relationships between measurement time and correlation time, and correlation time and effective system size, the measured values of the step width therefore depend also on the measurement time,

$$w = \sqrt{kTL_{eff} / 12\tilde{\beta}} = \left(kT/12\tilde{\beta}\right)^{1/2} \left(2\pi\Gamma_n \tilde{\beta} t_m / AkT\right)^{1/2n} \qquad (4)$$

as well as on the physical parameters of temperature, step stiffness. and step mobility.

III.A Generalized survival

The *x(t)* data are also used to determine the generalized survival probability *S(t, R),* the probability for the step position to remain above (below) a certain pre-assigned reference position *R* (−*R*) over a time interval *t* [85]:

$$S(t,R) \equiv \mathrm{Prob}\left\{\left(x(t') > R\right) \vee \left(x(t') < -R\right), \forall t_o \le t' \le t_o + t\right\}. \qquad (5)$$

In analyzing the experimental data we chose *R* values equal to *w/5, 2w/5, 3w/5, 4w/5* and *w*. The results are presented in Fig. 5 for the measurement at 460 K. The uppermost curve corresponds to the usual survival probability, *S(t),* with respect to *R* = 0, which clearly shows exponential decay in the intermediate time regime. The deviation from exponential behavior at long times is caused by the limit of the total measurement time, which has been discussed in detail in earlier work [32, 84]. The red straight lines are fits of the

experimental data to a generalized exponential form, $S(t, R) \sim exp(-t/\tau_s(R))$. The behavior is consistent with the theoretical prediction that, given an exponential autocorrelation function, the corresponding survival probability should have related exponential behavior [90]. Fitting $S(t, R=0)$ to an exponential form $S(t, R=0) \sim exp(-t/\tau_s)$ yields the survival time constants τ_s, which are 1.38 ± 0.20 s at 300 K and 1.35 ± 0.10 s at 460 K, approximately 1/10 the magnitude of the correlation time. From upper to lower, the other curves are the generalized survival probability with R increasing from $w/5$ to w. The measured generalized survival probabilities $S(t, R)$ for different R all decay exponentially at intermediate time. As R increases, the generalized survival probability decays faster. This is in consistent with numerical simulations of the generalized survival probability that were carried out for a one-dimensional model that provides a discrete realization of the non-conserved EW equation [85].

We confirmed numerically that the generalized survival probability $S(t, R)$ for the fourth-order conserved equation exhibits the same general behavior as that found in simulations [85] of the EW model. In particular, we find that $S(t, R)$ decays exponentially with time at long times, and that the time constant $\tau_s(R)$ of the exponential decay is a decreasing function of the distance R. The dependence of τ_s on R is consistent with the exponential form, $\tau_s(R) \propto exp(C_1 R/w)$ where w is the equilibrium width of the step and C_1 is a constant. It should be noted here that this functional form is purely empirical, and although our results for τ_s are consistent with this form, other forms for the dependence of τ_s on R cannot be ruled out. The observed dependence of $S(t, R)$ on the system size L and the sampling time δt (i.e. the time interval between two successive measurements of

the step position in the calculation of the generalized survival probability) is also similar to that found for the EW model [26].

The experimental values of the survival probability at $t = 0$, $S(0)$ and the time constants $\tau_s(R)$ extracted from the fits are listed in Table 1 and the time constants are plotted in Fig. 6a. The time constants $\tau_s(R)$ decrease exponentially with R, with different length-constants at different temperatures, as shown in Fig. 6a. When R is normalized by the step width w, the $\tau_s(R/w)$ curves at 300 K and 460 K almost collapse on each other as shown in Fig. 6b. Exponential fits to the data show that the time constant is equal to $\tau_s(R) = \tau_{s0}exp(-R/w)$ to well within one standard deviation. Even though the exponential dependence of the time constant on R is a phenomenological result of the simulation above and in reference [85], the above results confirm the observation and show that the offset value R should be scaled in terms of the step width in evaluating the generalized survival probability.

III.B Generalized inside survival

The concept of generalized survival is related to a relaxation from a position outside the reference level to the reference level (e.g. it is related to one-sided statistics). Physically, and for possible applications, we also may be interested in another form of generalized survival, which is the probability for the step edge to remain between the pre-assigned reference positions R and $-R$ over a time interval t. In this case we are asking about the probability of the step, initially at a small displacement, ***not*** fluctuating to larger displacements. In order to distinguish this case from the generalized survival, we refer to it as the generalized inside survival $S_{in}(t, R)$. The definition is as follows:

$$S_{in}(t,R) \equiv \mathrm{Prob}\{-R < x(t') < R, \forall t_o \le t' \le t_o + t\}. \quad (6)$$

The generalized inside survival probabilities also have a clear exponential behavior on time, as shown in Fig. 7a. When R is less than w, the generalized survival decays quickly, with time constants less than 0.5 s. Given the sampling interval of 51.2 ms in our measurement, we obtain the most significant results with R values greater than w, although exponential decay is also clear at the smaller offsets. In contrast to the generalized survival, as R increases the generalized inside survival time constant also increases. This is reasonable intuitively, since it takes longer to cross larger R or $-R$ because the average required step excursion is larger. Fitting these generalized inside survival experimental data yields characteristic time scales, the generalized inside survival constants, $\tau_{sin}(R)$, as shown in Fig. 7b. The collapse of the curves with scaling as R/w is not as complete as for the generalized survival (Fig. 6), in particular with some deviation at 300 K for small R/w. The curves can be fit to an exponential form $\tau_{sin0}\ exp(A(R/w)^{\lambda})$, but the fits suggest a temperature dependence to the value of λ, as discussed below.

To determine the appropriate functional form for the dependence of the time constant on offset, R, the inside survival probabilities were also determined from the numerical simulations, with results shown in Fig. 8 for three different values of R (R/w = 0.5, 0.75 and 1.0). Fits of the long-time data to an exponential form are also shown to illustrate that the decay is exponential in time for large t. The data shown were obtained using δt = 1.0. We have examined how the measured $S_{in}(t, R)$ depends on the values of the sampling time δt and the sample size L. These results are consistent with the scaling behavior found in Ref. [78] for the generalized survival probability:

$$S_{in}(t, R, \delta t, L) = f_1(t/\delta t, R/w(L), \delta t/\tau_c(L)) \qquad (7)$$

where $w(L) \propto L^{0.5}$ is the equilibrium width and $\tau_c(L) \propto L^4$ is the correlation time of a step of length L, and f_1 is a scaling function.

The time scales $\tau_{sin}(R)$ associated with the exponential decay of $S_{in}(t, R)$ may be obtained from fits such as those shown in Fig. 8a. The results of the numerical simulation for the dependence of τ_{sin} on R/w, obtained for $L = 200$ and $\delta t = 1$, are shown in the top plot in Fig. 8b. It is clear from the plot that an exponential dependence, $\tau_{sin}(R) \propto exp(C_2 R/w)$, does not provide a good description of the data: the plot of $\log\tau_{sin}$ vs. R/w clearly shows considerable curvature. Similar behavior was also found for the R-dependence of τ_{sin} for the one-dimensional EW equation [88]. We have found that the empirical form, $\tau_{sin}(R) \propto exp[C_2 (R/w)^{\lambda}]$, with C_2 a constant and $\lambda \approx 0.6$, provides a good description of the simulation data. A fit to this form with $\lambda = 0.59$ is shown by the upper line in Fig. 8b. For comparison, the experimental data in Fig. 7b are shown with curves for best fits to the pure exponential ($\lambda = 1$) and exponential square root ($\lambda = 1/2$) forms.

The results obtained from the equilibrium simulations described are not directly comparable with those obtained from the experiments because in the experiments, the step position is measured as an average over a finite measurement time t_m. This has been shown to be important [84], because measurements of the survival probabilities require knowledge of the true average step position: the quantity R is, by definition, the distance of the reference level from the true average step position. In simulations, the true average step position is known, as discussed above. In experiments, on the other hand, the average step position differs from the true position if t_m is $< \tau_c$ because fluctuations with relaxation times larger than t_m can not be thoroughly sampled during the measurement

time. In experiments [32, 84], the effect of using a finite t_m is approximately equivalent to that of having a finite system of size $L_{eff} \propto t_m^{1/n}$ with $n = 4$ in the present case. This implies the following scaling dependence of the measured survival probability on the measurement time t_m:

$$S_{in}(t, R, \delta t, t_m) = f_2(t/\delta t, R/w(t_m), \delta t/t_m), \qquad (8)$$

where $w(t_m)$ is the measured step width (i.e. the root-mean-square deviation of the step position from its apparent average value). In principle, the scaling function should also have as its argument another scaling variable, t_m/τ_c, but the dependence on this variable may be neglected if $t_m < \tau_c$. Note that this scaling form implies that if the measured $S_{in}(t, R)$ decays exponentially in time, then the time scale of this decay, measured in units of δt, should be a universal function of $R/w(t_m)$ if $\delta t/t_m$ is held fixed.

We have studied by simulation the effect of a finite measurement time on the behavior of the generalized inside survival probability. In these simulations, the Langevin equation was numerically integrated for time t_m, starting from an equilibrated step profile. The average $\overline{x}_i$ of $x_i(t)$ over the time period t_m was then taken to be the "experimentally measured" average step position at lattice site i, and the quantities $x_i'(t) \equiv x_i(t) - \overline{x}_i$ were used to define the interface width $w(t_m)$ and to calculate the generalized inside survival probability $S_{in}(t, R)$ for different values of R (taken to be the distance from the "experimentally measured" average step position defined above). Our results for the dependence of the "experimentally measured" step width $w(t_m)$ on the measurement time t_m are in good agreement with those reported in [32]. In particular, we find that $w(t_m) \propto t_m^{1/2n}$ with $n = 4$. Also, the numerically obtained distribution of the $x_i'(t)$ is very well

described by a Gaussian with zero mean and width equal to $w(t_m)$, in further good agreement with the experimentally observed behavior of the distribution of the step displacements.

The results for the generalized inside survival probability with finite measurement time, obtained from the procedure described above, are shown in Fig. 9. The plots in this figure show results obtained from simulations with $t_m = 5000$ and $\delta t = 2.5$. It is clear from these plots that the "finite-time" $S_{in}(t, R)$ decays exponentially in time for large t, and that the time scale τ_{sin} of this decay increases with R. A plot for the time dependence of $S_{in}(t, R)$ for $R/w = 2.0$, obtained from simulations with $t_m = 1000$ and $\delta t = 0.5$, is also shown in the figure. Since $\delta t/t_m$ has the same value (= 1/2000) in both the simulations, the scaling relation of Eq.(8) predicts that plots of $S_{in}(t, R)$ vs. $t/\delta t$ obtained from the two simulations with the same value of R/w should coincide. As shown in Fig. 9, the two plots are close to each other, but not exactly coincident. Thus, the scaling relation of Eq.(8) is approximately, but not exactly satisfied, probably reflecting a dependence on the additional scaling variable t_m/τ_c mentioned above. It is clear from the data that the time scale τ_{sin} obtained from the simulation with $t_m = 1000$ is slightly larger (by ~ 5%) than the value obtained from the simulation with $t_m = 5000$. A similar increase in τ_{sin} with decreasing t_m is also found for other values of R/w and in simulations with smaller t_m.

The dependence of the time scale τ_{sin} on R/w, obtained from the "finite-time" simulation with $t_m = 5000$, $\delta t = 2.5$, is shown in the bottom plot of Fig. 8b. The empirical form, $\tau_{sin}(R) \propto exp[C_2 (R/w)^{\lambda}]$, provides a good description of the data, but with a value of λ (≈ 0.8) that is larger than that found for the results of the equilibrium simulation. A fit of the numerical results for τ_{sin} to this form with $\lambda = 0.8$ is also shown in Fig. 8b.

These results suggest that the value of λ is not "universal". It is also possible that this functional form does not represent the actual dependence of τ_{sin} on R/w.

The values of t_m and δt in the "finite-time" simulations were chosen so as to make the value of the scaling variable $\delta t/t_m$ the same as that (1/2000) used in the experiments. If the scaling relation of Eq.(8) is valid (as discussed above, our simulation results indicate that it is valid to a good approximation), then the results for $\tau_{sin}/\delta t$ obtained from simulations should match those obtained in the experiment for the same value of R/w. To test this prediction, we have multiplied the simulation results for $\tau_{sin}/\delta t$ by the δt (0.0512 s) used in the experiment to obtain values of $\tau_{sin}(R/w)$ in physical time units (seconds) for different R/w. Fig. 10 shows a comparison of the values of τ_{sin} obtained this way with the experimental results obtained at temperature T = 460 K. It is clear from the plots in this figure that the simulation results are in good agreement with the experimental ones. The small differences between the two sets of results for R/w near 2.0 may be due to insufficient sampling of the tails of the Gaussian distribution of the step displacement in the experiment.

Since the experimental measurements at temperatures 460 K and 300 K were carried out with the same values of t_m and δt, the scaling behavior discussed above suggests that the values of τ_{sin} for these two temperatures should be the same for a fixed R/w. As shown earlier (Fig. 7b), the experimental results for τ_{sin} at T = 300 K do not collapse to the same shape as those at 460 K when scaled as R/w. The experimental data were carefully evaluated, and there is no apparent systematic problem that could explain this difference. However, an underlying physical cause may arise from a dependence of the scaling function in Eq.(8) on the additional scaling variable t_m/τ_c. The expected

temperature dependence of the physical parameters that govern the step fluctuations indicates that the true correlation time $\tau_{c,true}$ increases by three orders of magnitude as T is decreased from 460 K to 300 K. Since t_m is the same at the two temperatures, the corresponding values of $t_m/\tau_{c,true}$ would also differ by three orders of magnitude. The experimental offset in the values of ts measured at the two temperatures is consistent with the direction of offset shown in Fig. 9. The question of whether the more dramatic change of the experimental $\tau_{c,true}$ might also account for the apparent change in the fit parameter, λ, unfortunately, cannot be immediately tested numerically because t_m can not be changed by several orders of magnitude in the simulation.

IV. Discussion

The first discussions of survival probability focused on the question of one-sided crossing of the average position (x = 0) of the step. This probability is related to the experimental problem of the time for relaxation of a step initially displaced by a distance x_0 from equilibrium, which is expected to go as [11, 91, 92]:

$$\langle x \rangle = x_0 \exp(-t/\tau_{eq}), \qquad (9)$$

where τ_{eq} has been shown to equal the correlation time τ_c, for the cases of attachment/detachment and periphery diffusion limited step fluctuations. The relationship of the survival time constant to the correlation time is thus intuitively reasonable. Here we have tested the numerical prediction for a broader definition of survival (generalized survival) involving one-sided crossing of a boundary displaced by an offset R from the average step position. The maximum survival probability ($S(0)$) in this case reduces to the probability of initially finding the step at a displacement greater than R:

$$S(0,R) = \int_{|x|>R} \frac{1}{w\sqrt{2\pi}} \exp(-x^2/2w^2)dx \,. \qquad (10)$$

As shown in Table I and Fig. 4, the experimental values of *S(0, R)* agree with the known values of Eq. (10).

As predicted theoretically, our generalized survival data are well fitted to a functional form

$$S(t,R) = S_0 \exp(-t/\tau_s(R)) \,. \qquad (11)$$

In addition, we show empirically that the offset-dependent time constant $\tau_s(R)$ also follow a simple relationship:

$$\tau_s(R) = \tau_{s0} \exp(-R/w) \,. \qquad (12)$$

This is consistent with numerical results that showed the exponential dependence of the time constant on the offset distance, *R*. It is also consistent with the theoretical scaling form of the generalized survival probability [85]:

$$S(t,L,R,\delta t) = f(\frac{t}{L^4}, \frac{R}{L^a}, \frac{\delta t}{L^4}), \qquad (13)$$

where *L* is the system size and α is the roughness exponent, which for steps on Ag(111) surfaces in this temperature range, is 1/2 [93]. The relationship between *w* and *L* (see Eq. (3)) is $w \propto L^{1/2}$. Thus our observed scaling form with R/w as the scaling variable is consistent with the theoretical prediction of R/L^{α} scaling at any fixed temperature. For physical systems, the identification of the step width as the relevant variable that sets the scale of the offset distance *R* further allows quantitative prediction of the variation of the survival time constant with changing physical parameters such as temperature, step stiffness and step mobility.

The generalized inside survival probability physically provides complementary information to the generalized survival. As expected, the values at $t = 0$, shown in Tables 1 and 2, reflect the Gaussian distribution of Fig. 4 and Eq. 10, yielding $S_{in}(0,R) = 1 - S(0,R)$. The exponentially increasing time constants for the inside survival, as the offset distance R increases, reflect physically the effect of the restoring force (due to the step stiffness) opposing the outward displacement of the step that would allow it to cross the offset position.

For both generalized probabilities considered, the dependence of the relaxation time constant on offset has not been determined analytically. The problem is especially difficult for inside survival, which does not have the clear relationship to the problem of one-sided statistics that has been used to evaluate generalized survival. Our results, both numerical and experimental, however provide clear evidence for a functional form, $\tau_{sin0} \exp(A(R/w)^{\lambda})$, that must be numerically equivalent to any analytical solution in the parameter space accessible to the experiments and simulations.

For applications, both the generalized survival and the generalized inside survival provide an approach for evaluating the impact of stochastic behavior on future nanometer scale electronic devices. The results here show that this can be accomplished semi-quantitatively given only knowledge of the measurement time and the interface width. For instance, we can consider the combination of the two generalized survival probabilities, $1 - S(R, t) - S_{in}(R, t) = P_c(R, t)$, where $P_c(R, t)$ is the probability that the step edge ***does*** cross the pre-assigned reference positions R ($-R$) for any given starting point. Such a problem may be related to a specific behavior that would be triggered by first arrival at the reference point. At present, the effects of atomic-scale structural

variation on interconnections in nanoelectronics and molecular electronics are in the early stages of understanding [94, 95]. As our ability to control interfaces grows, it may be possible to exploit such quantitative statistical knowledge of the effects of thermal fluctuations.

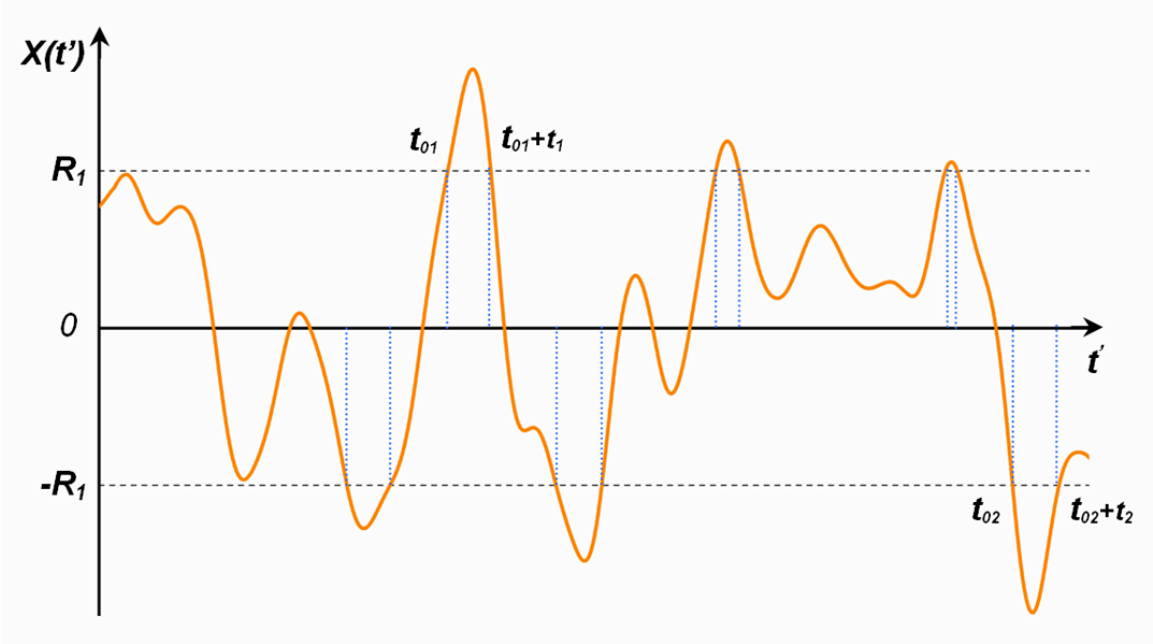

Fig. 1 (Color online). Schematic representation of temporal step wavelengths and the definition of the offset reference position R. Any interval of time over which the step remains $> R_1$ ($< -R_1$) represents a survival event. For instance in any interval between t_{01} and $t_{01} + t_1$ or between t_{02} and $t_{02} + t_2$ the step trajectory has survived by not crossing R_1 ($-R_1$). The solid orange line indicates the step position. The vertical dashed blue lines indicate time intervals for $S(t, R)$ with respect to the reference position R_1 ($-R_1$).

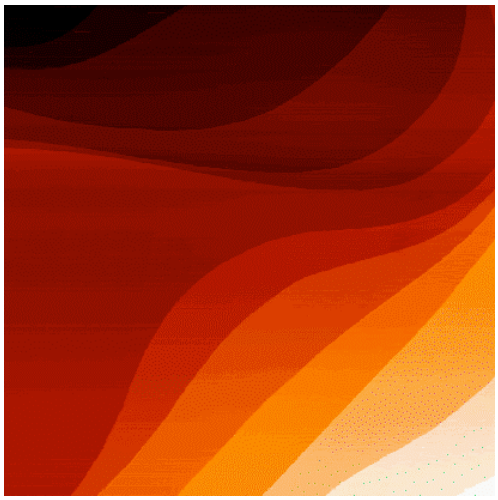

Fig. 2 (Color online). STM topography image of an 800 × 800 nm^2 Ag(111) surface. Tunneling conditions are $U_{sample} = -1.70$ V and $I_t = 95$ pA.

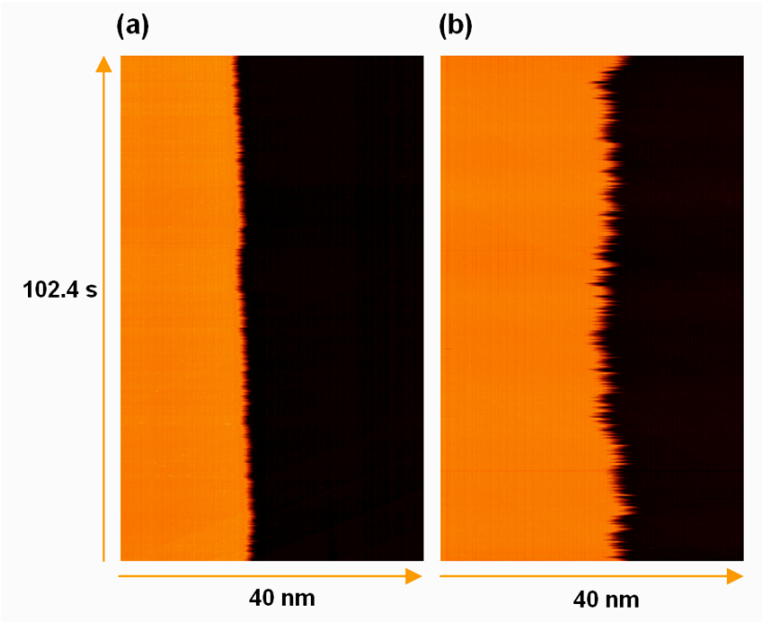

Fig. 3 (Color online). STM temporal pseudoimages obtained by scanning the STM tip over a fixed position on the step edge in the direction perpendicular to the step orientation. For both images, the line-scan length

is 40 nm, a line-scan time 51.2 ms, and total time 102.4 s with 2000 lines. The step orientations are along a close-packed direction. The images are obtained at 300 K (a) and at 460 K (b).

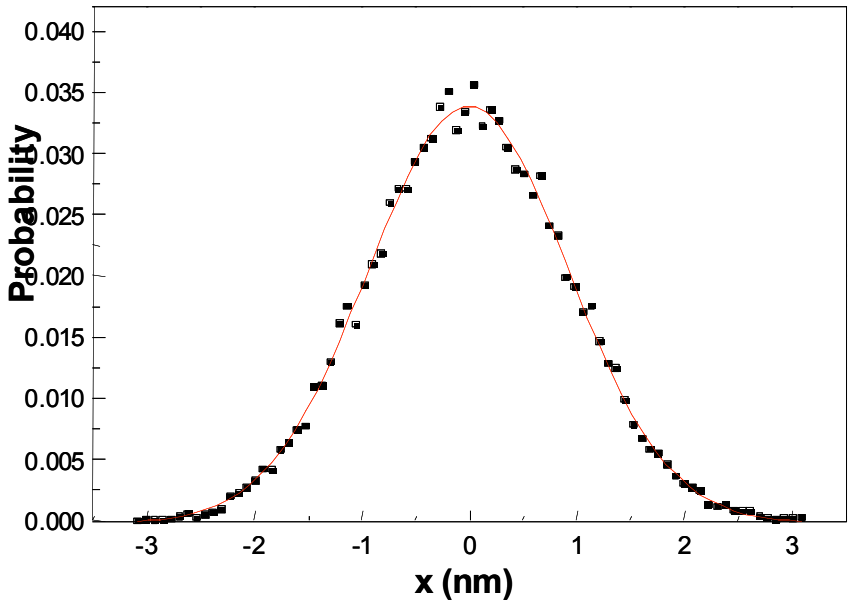

Fig. 4 (Color online). The distribution of step displacements at 460 K. The red fitting curve is Gaussian fit of the data with a width 0.930 ± 0.010 nm.

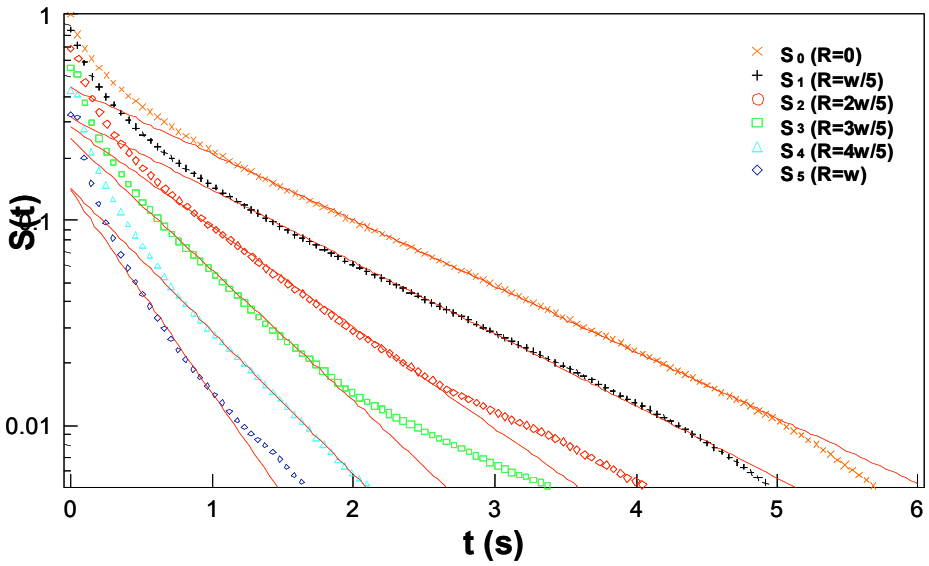

Fig. 5 (Color online). The generalized survival probability curves *S(t, R)* and corresponding fitting curves at 460 K. From upper to lower, the curves are respectively the generalized survival probability with respect to $R = 0$, $w/5$, $2w/5$, $3w/5$, $4w/5$, and w. The solid red lines are corresponding exponential fits for each curve. The time constants extracted from the fits are listed in Table I.

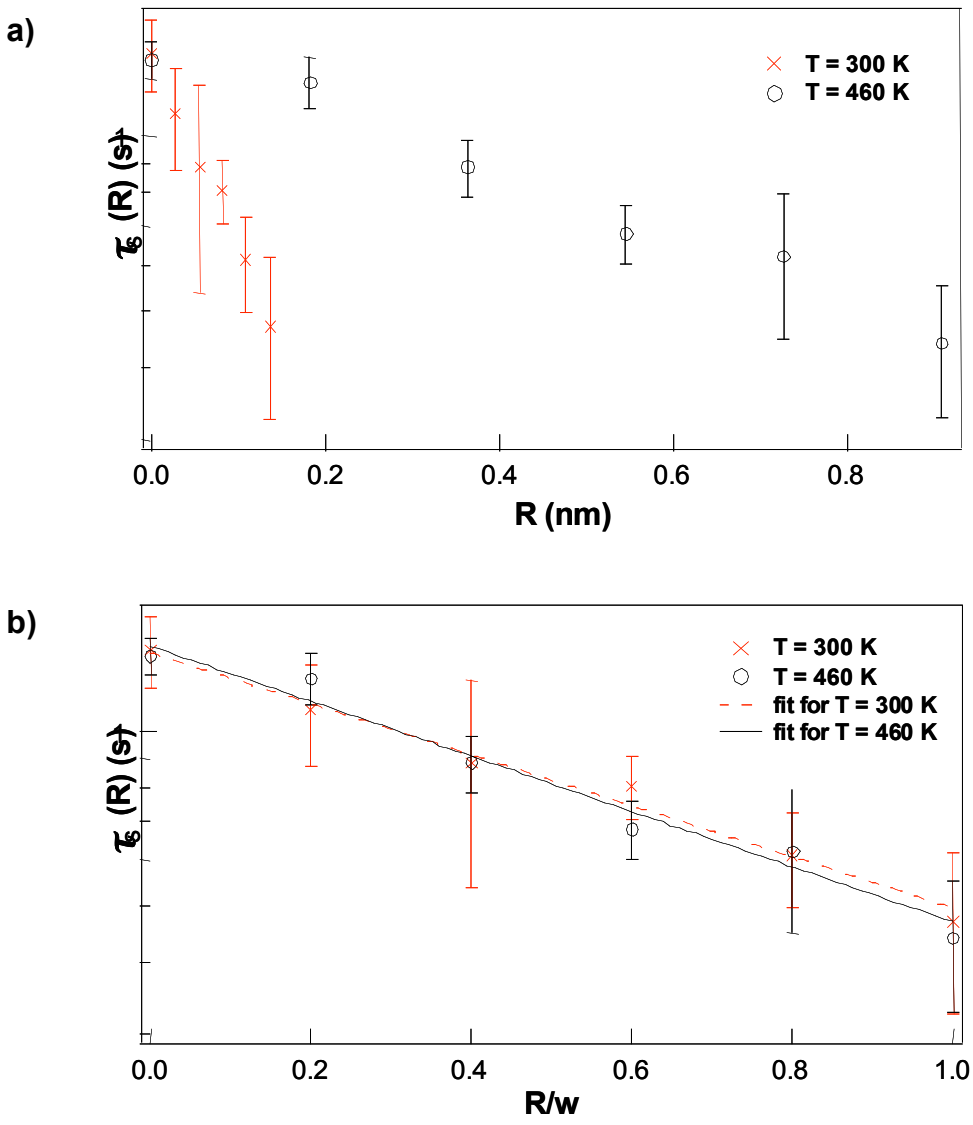

Fig. 6 (Color online). a) The generalized survival time constants, $\tau_s(R)$ vs. R. The red crosses are $\tau_s(R)$ at 300 K and the black circles at 460 K. b) The same data with R normalized by w. The red crosses are $\tau_s(R)$ at 300 K and the black circles at 460 K. The red dashed line and black solid line are corresponding un-weighted exponential fits for these two data sets respectively, $\tau_s(R) = \tau_{s0}exp(-A(R/w))$. The best fitting parameters are τ_{s0} = 1.37 ± 0.03 s, A = 1.01 ± 0.06 for $\tau_s(R)$ at 300 K, and τ_{s0} = 1.40 ± 0.06s, A = 1.09 ± 0.11 for $\tau_s(R)$ at 460 K.

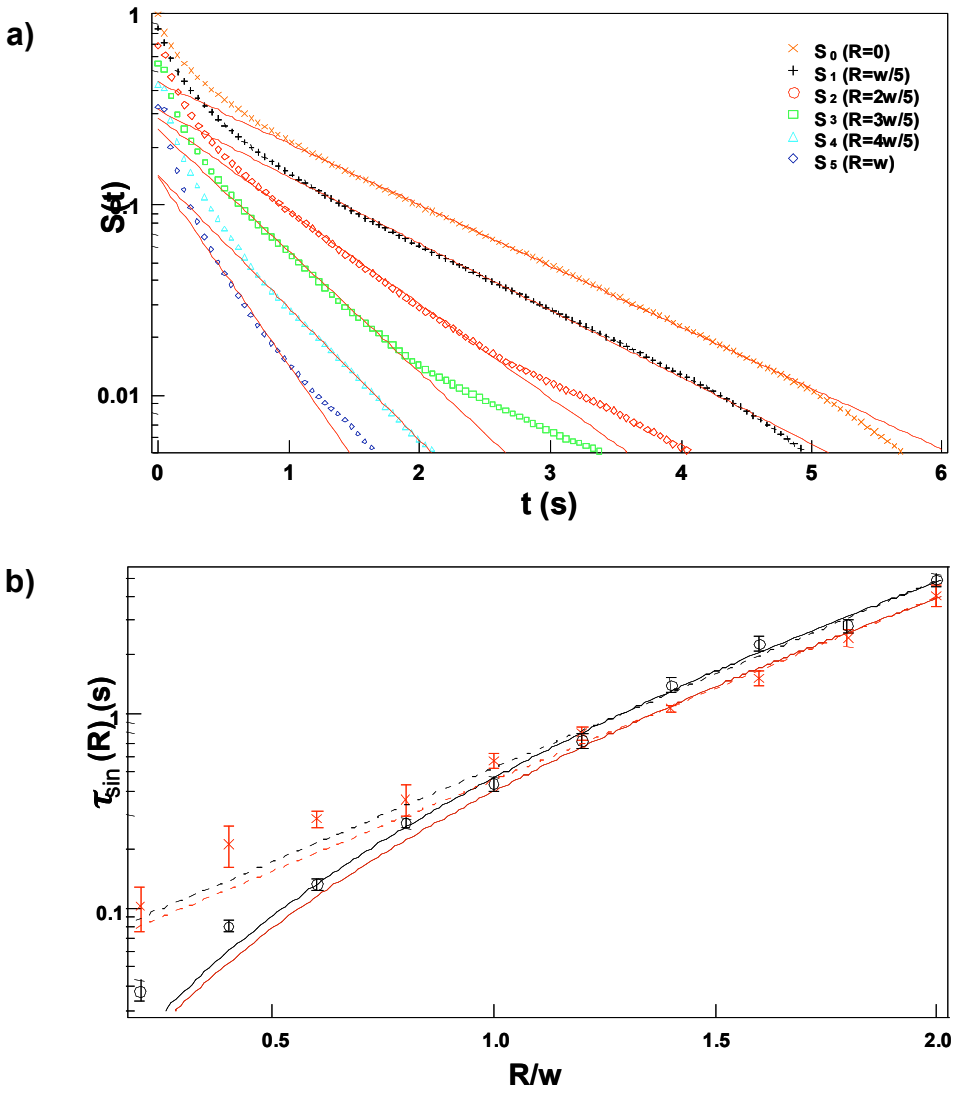

Fig. 7 (Color online). a) The generalized inside survival probability curves $S_{in}(t, R)$ and corresponding fitting curves at 460 K. From lower to upper, the curves are respectively the generalized survival probability with respect to R = 6w/5, 7w/5, 8w/5, 9w/5, and 2w. The solid red lines are corresponding exponential fits for each curve. The time constants extracted from the fits are listed in Table I. b) Time constants for the generalized inside survival probability, $\tau_{sin}(R)$ vs. R/w. The red crosses are $\tau_{sin}(R)$ at 300 K and the black circles at 460 K. The dashed lines are corresponding un-weighted exponential fits for these two data sets respectively using the fitting formula, $\tau_{sin}(R) = \tau_{sin0}exp(A(R/w)^{\lambda})$ *with* $\lambda = 1$. The best fitting values are $\tau_{sin0} = 0.05 \pm 0.01$ s, $A = 2.16 \pm 0.09$ for $\tau_{sin}(R)$ at 300 K (red), and $\tau_{sin0} = 0.06 \pm 0.01$ s, $A = 2.21 \pm 0.12$ for $\tau_{sin}(R)$ at 460 K (black). The solid lines are fits using the same fitting formula with $\lambda = 1/2$. The

best fitting values are $\tau_{sin0} = 0.002 \pm 0.001$ s, $A = 5.50 \pm 0.39$ for $\tau_{sin}(R)$ at 300 K (red), and $\tau_{sin0} = 0.002 \pm 0.001$ s, $A = 5.58 \pm 0.30$ for $\tau_{sin}(R)$ at 460 K (black).

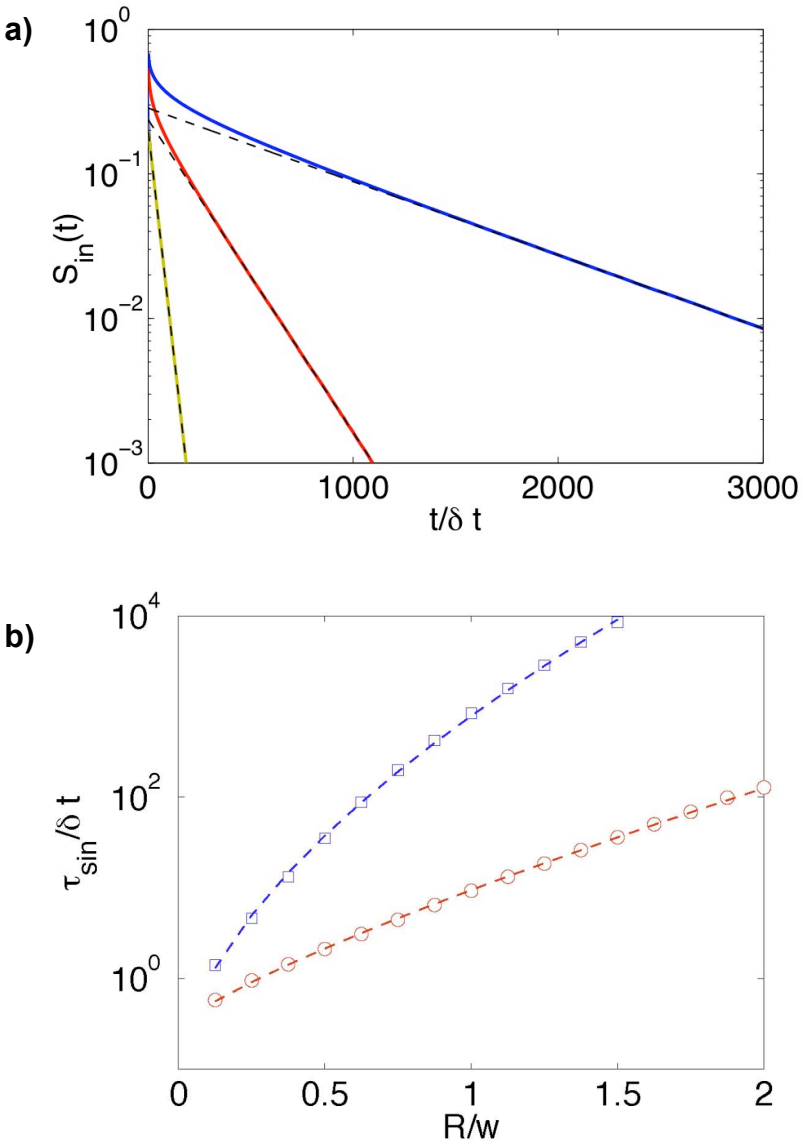

Fig. 8 (Color online). a) The generalized inside survival probability $S_{in}(t, R)$ as a function of time t (scaled by the sampling interval $\delta t = 1$) for three different values of the distance R. The thick lines (from top to bottom, $R/w = 1.0$ (blue), 0.75 (red) and 0.5 (green)) represent the simulation data and the (black) dashed lines represent exponential fits to the long-time data. b) Dependence of the time scale $\tau_{sin}(R)$, measured in units of the sampling interval δt, on the distance R, measured in units of the interface width w. In the upper

curve of b), the results obtained from equilibrium simulations for sample size L = 200 and sampling interval δt = 1 are shown by the (blue) squares. The (blue) dashed line passing through the data points represents a fit to the form $\tau_{sin}(R) \propto exp[C_2(R/w)^{\lambda}]$ with λ = 0.59. The lower curve in b) shows the results ((red) circles) obtained from a "finite-time" simulation (see text) with measuring time t_m = 5000 and δt =2.5. A fit of these data to the above form with λ = 0.8 is shown by the (red) dashed line. The error bars for the simulation data are smaller than the size of the symbols used in the plots.

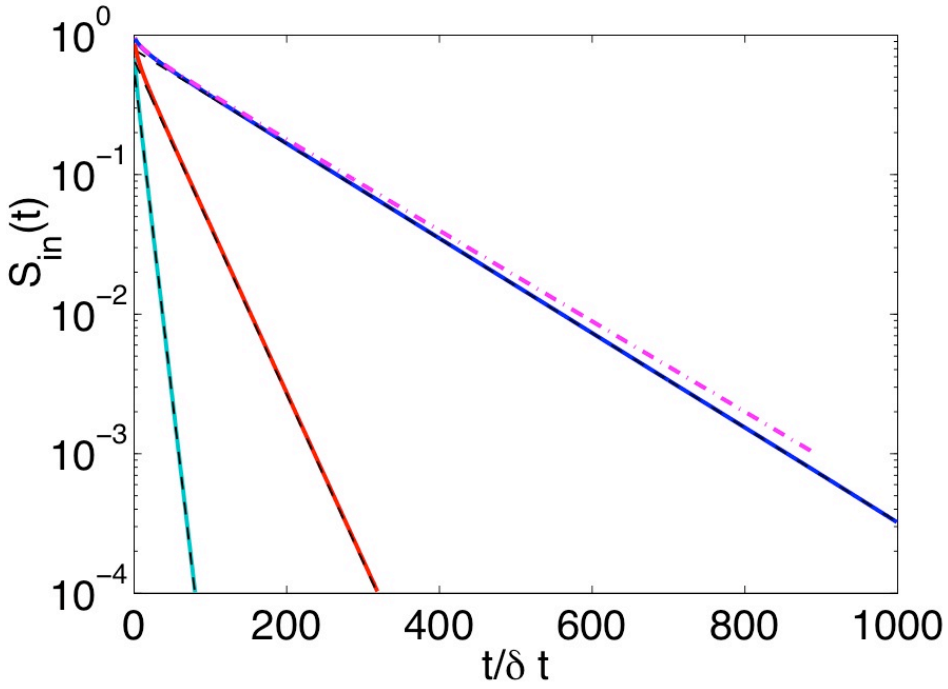

Fig. 9 (Color online). The generalized inside survival probability $S_{in}(t, R)$, calculated from "finite-time" simulations with t_m = 5000 and δt = 2.5 (see text), as a function of time t scaled by the sampling interval δt, for three different values of the distance R. The thick lines (from top to bottom, R/w = 2.0 (blue), 1.5 (red) and 1.0 (green)) represent the simulation data and the (black) dashed lines represent exponential fits to the long-time data. The (magenta) dash-dotted line shows the results for R/w = 2.0 obtained from a simulation with t_m = 1000 and δt = 0.5.

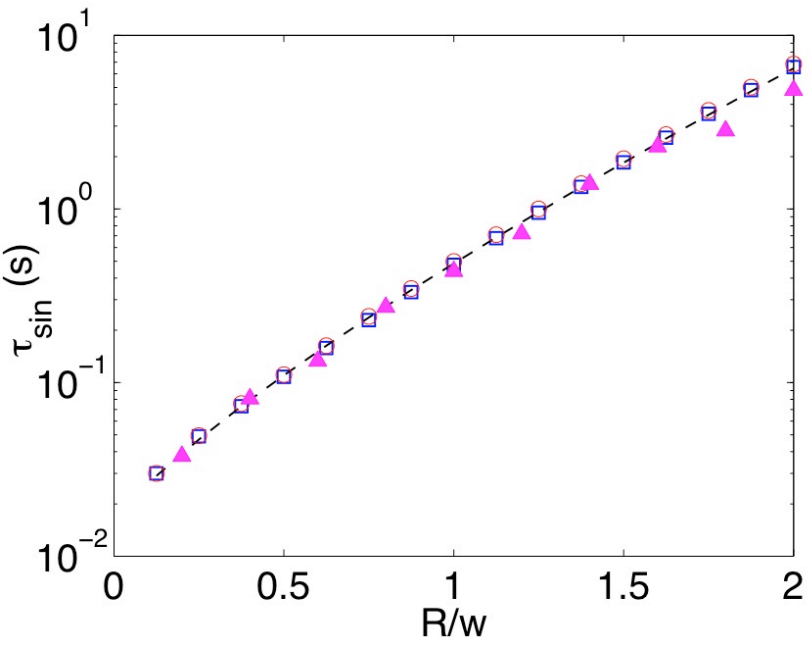

Fig. 10 (Color online). Comparison of numerical and experimental results for the time scale $\tau_{sin}(R)$ of the decay of the generalized inside survival probability. The (blue) squares and (red) circles respectively represent the simulation results obtained for t_m = 5000, δt = 2.5 and for t_m = 1000, δt = 0.5. The experimental results for temperature T = 460 K are shown by the (magenta) triangles. The (black) dashed line shows a fit of the simulation data to the empirical form, $\tau_{sin}(R/w) \propto exp[C_2(R/w)^{\lambda}]$, with $\lambda = 0.8$.

Table I Experimental parameters determined from fits to experimental *x(t)* data. The root mean-squared width *w* is determined from the distribution of *x(t)* as in Fig. 4, the correlation time is determined from fits to Eq. (4). The generalized survival intercepts, e.g. the experimentally measured values at $t = 0$, (*S(0)* and $S_{in}(0)$) are shown and the time constants (τ_s and τ_{sin}) extracted from the *x(t)* data using Eqs. (11) and (12). The offset values range from $R = 0$ to $R = w$. The known values of the Gaussian integral (Eq. (10)) yield expected values of *S(0)* are 1 (R/w=0), 0.841 (R/w=0.2), 0.689 (R/w=0.4), 0.549 (R/w =0.6), 0.424 (R/w =0.8), and 0.317 (R/w =1.0).

T (K)	w (nm) τ_c (s)	*R/w*	*S(0)*	τ_s *(R)*	$S_{in}(0)$	τ_{sin} *(R)*
300	w = 0.136±0.007 τ_c =11.8 ± 4.9	0	1.00	1.38 ± 0.20		
		0.2	0.84 ± 0.04	1.09 ± 0.22	0.16 ± 0.04	0.10 ± 0.03
		0.4	0.69 ± 0.06	0.88 ± 0.35	0.31 ± 0.06	0.21 ± 0.05
		0.6	0.54 ± 0.05	0.81 ± 0.10	0.46 ± 0.06	0.29 ± 0.03
		0.8	0.42 ± 0.03	0.61 ± 0.12	0.58 ± 0.03	0.36 ± 0.07
		1.0	0.31 ± 0.03	0.47 ± 0.15	0.69 ± 0.03	0.57 ± 0.05
460	w = 0.908±0.043 τ_c =15.1 ± 5.9	0	1.00	1.35 ±0.10		
		0.2	0.85 ± 0.01	1.24 ±0.13	0.15 ± 0.01	0.04 ± 0.01
		0.4	0.69 ± 0.02	0.89 ±0.10	0.31 ± 0.02	0.08 ± 0.01
		0.6	0.56 ± 0.02	0.68 ±0.08	0.4 ± 0.022	0.13 ± 0.01
		0.8	0.43 ± 0.02	0.62 ±0.17	0.57 ± 0.02	0.27 ± 0.02
		1.0	0.32 ± 0.02	0.44 ±0.11	0.68 ± 0.02	0.44 ± 0.04

Table II Experimental parameters for the inside survival for offset values ranging from $R = 1.2w$ to $R = 2w$. The expected values for $S_{in}(0)$ based on the Gaussian distribution are: 0.770 (R/w = 1.2), 0.838 (R/w = 1.4), 0.890 (R/w = 1.6), 0.928 (R/w = 1.8). 0.954 (R/w = 2.0).

T (K)	*R/w*	$S_{in}(0)$	τ_{sin} *(R)*
300	1.2	0.77 ± 0.02	0.79 ± 0.06
	1.4	0.84 ± 0.01	1.06 ± 0.05
	1.6	0.89 ± 0.01	1.51 ± 0.13
	1.8	0.93 ± 0.01	2.44 ± 0.24
	2.0	0.96 ± 0.01	4.04 ± 0.50
460	1.2	0.76 ± 0.01	0.72 ± 0.06
	1.4	0.84 ± 0.01	1.39 ± 0.12
	1.6	0.89 ± 0.01	2.28 ± 0.21
	1.8	0.930 ± 0.004	2.83 ± 0.21
	2.0	0.956 ± 0.005	4.83 ± 0.34

3.2 Pinned steps on Ag(111)

Introduction

At the nanometer scale, the properties of materials and devices are dramatically changed due to size effects. In order to exploit nanodevices, a fundamental and challenging issue is to study the stability of metal surfaces, which is dominated by mass transport on the surfaces. Specially on Ag(111) surfaces, the step-edge fluctuations are dominated by thermal Ag atoms diffusion along step edges. The motion includes all the wavelengths accessible to the line within the correlation length. Normally, the nominal length of steps (topographic length) is much longer than the corresponding correlation length, so the steps can be considered as free steps. The correlation length is determined by temperature and kink density on the step edge. In principle, if the nominal length is smaller than the corresponding correlation length of the free step, the correlation length should be equivalent to the nominal length. Herein, we use impurity on Ag(111) surfaces to pin steps and investigate this problem.

Experimental

The procedure to make Ag film is similar to the method that has been reported in previous papers. The only difference is that during depositing Ag onto the freshly cleaved mica substrate, the pressure is some 10^{-5} torr, which is about 1 order higher than the pressure in our previous process. This causes more impurity in the Ag films. Then samples are transferred into a UHV chamber (base pressure $< 5 \times 10^{-11}$ torr). After

several sputtering and annealing cycles, clean Ag(111) films are obtained, and checked by LEED and STM. On the STM stage, sample temperature is controlled with a PBN heater. At ~ 410 K, the typical STM topography image is shown in Fig. 1. On the surface, steps are pinned by the impurity points, which are shown as white dots in this STM image. Different from free steps, step fluctuations of "pinned" steps are much less obvious, which directly reveal the fluctuation magnitude is smaller. In a zoomed-in image as shown in Fig. 2, we can clearly see this difference.

Fig. 1 (Color online) Pinned steps on Ag(111)

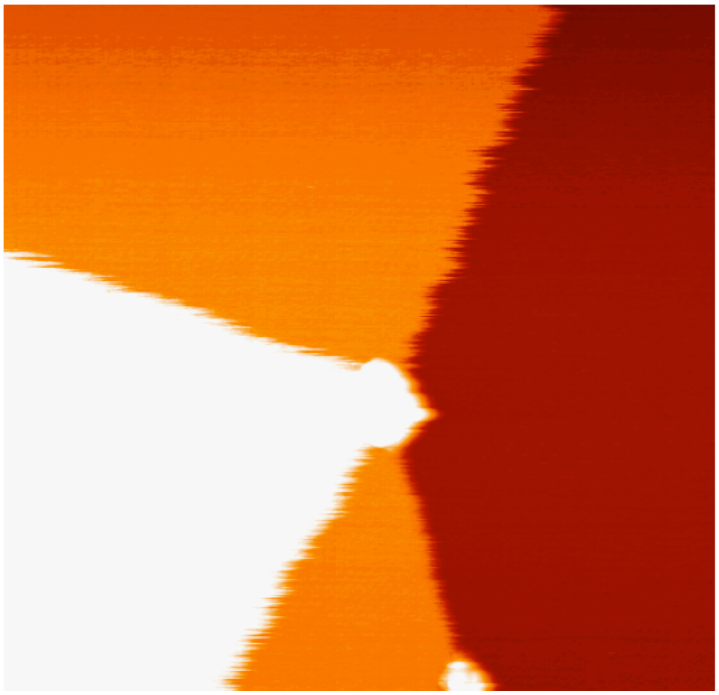

Fig. 2 (Color online) Pinned steps (52 × 52 nm^2)

In order to measure fluctuations, we use repeated STM scans across a fixed position at the step boundary, at the mid-point between the two ends for "pinned" steps. For free steps, this fixed position can be arbitrarily chosen at any point on the step edge. The outcome of this repeated scanning are temporal pseudo-images. The typical mild tunneling conditions are 90 to 110 pA for tunneling current and 1.50 to 1.70 V for sample bias. Under these conditions, the tip-sample interaction can be negligible. For all data presented in this paper, the time interval between scan lines is 51.2 ms, and the total measurement time for each pseudo-image is 102.4 s with 2000 line scans. Ten to fifteen sets of x(t) data are measured for each step segment.

From pseudo-images, the step-edge position x(t) can be extracted by image processing. First we flatten the image for the upper or lower terrace, and then identify the step point at which surface height is midway between the heights of the upper and lower

terrace heights. The individual x(t) data sets are used to calculate individual correlation and autocorrelation functions. The reported correlation and autocorrelation functions are averages of ten to fifteen individual measurements.

Results and discussions

As we discussed in Chapter 1 and the previous section in this chapter, starting from the Langevin formalism, we have correlation functions with the following form:

$$G(t) = \left\langle \left(x(t) - x(0) \right)^2 \right\rangle = \left(\frac{2\Gamma\left(1 - 1/n\right)}{\pi} \right) \left(\frac{kT}{\tilde{\beta}} \right)^{\frac{n-1}{n}} \left(\Gamma_n t \right)^{\frac{1}{n}} = G_0 t^{\frac{1}{n}}, \qquad (1)$$

where Γ_n represents the step mobility, and $\tilde{\beta}$ the step stiffness. Determined by the mass transport mechanism around step edges, the characteristic exponent *n* is equal to 2 and 4 respectively, for the AD and PD cases. By fitting the correlation functions, *n* can be extracted, as shown in Fig. 3a. Here we measure the pinned steps with length from 20 nm to 100. For comparison, we also measure an unpinned step (called free step). In the log-log plot, all the correlation functions are roughly parallel to each other, indicating the slope, 1/n, is similar. The resulting values of 1/n from fitting are represented in Fig. 3b. The data point after the break in the horizontal axis is the date for free step. For all these steps, 1/n is close to the theoretical value ¼ for the PD case. So for the pinned steps, the fluctuations are also governed by the periphery diffusion. On the other hand, G_0 does depend on the step length as shown in Fig. 3c. For PD limit fluctuations, we know G_0 is related the amplitude of the fluctuations. Roughly speaking, larger G_0 indicates larger fluctuation amplitude. So the results of G_0 vs. step length in Fig. 3c are consistent with the direct observation from the frizzy morphology of pinned steps as shown in Fig. 2. To

precisely study the relationship between the amplitude and the step length, we introduce the mean squared width of fluctuating steps:

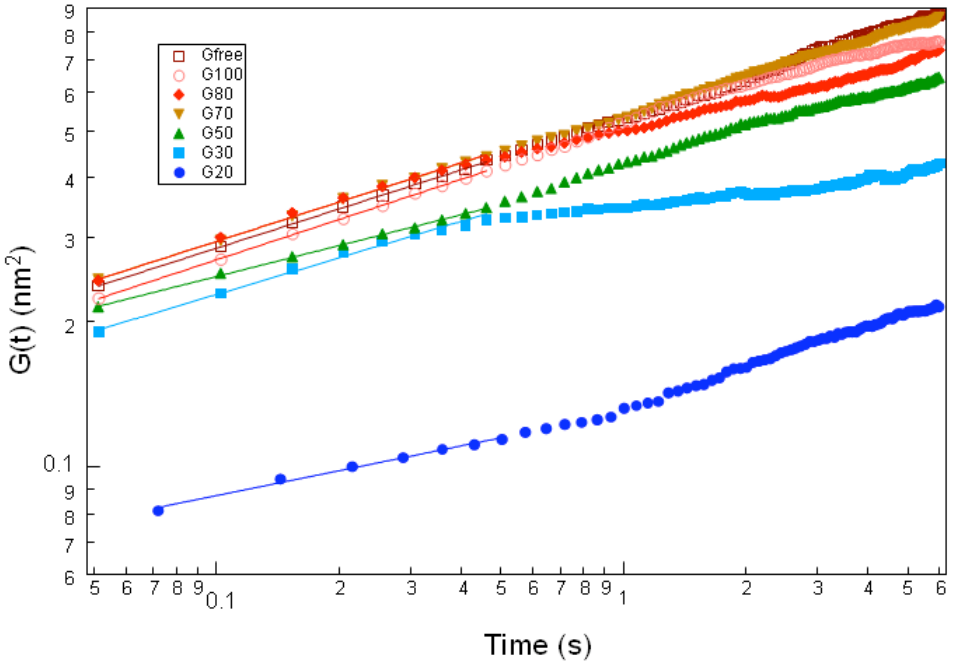

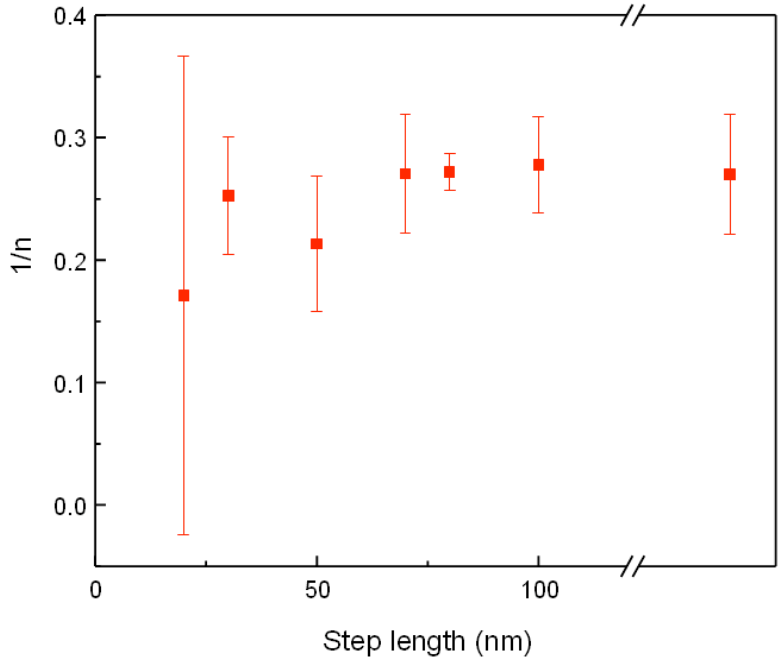

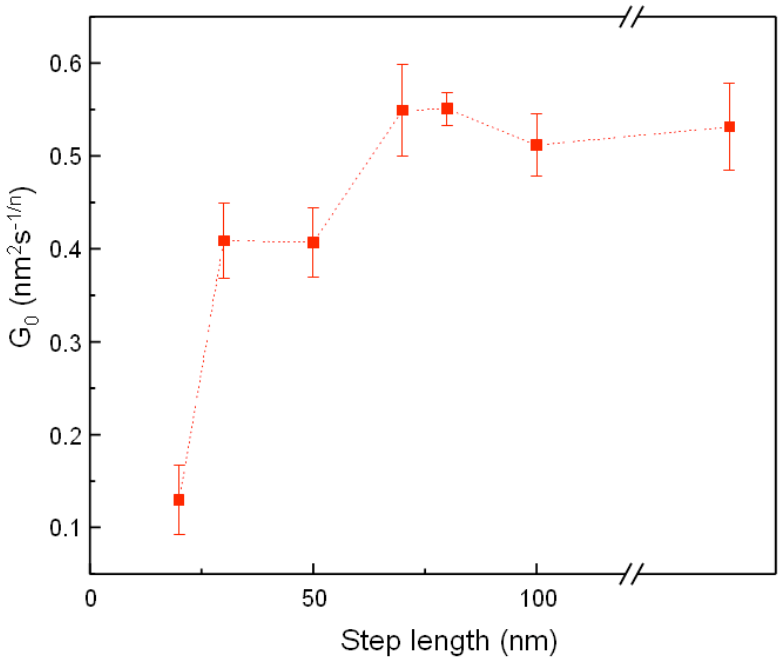

Fig. 3 (Color online) Correlation functions of steps with different length. (a) Correlation functions and corresponding fits. (b) 1/n vs. step length. (c) G_0 vs. step length.

$$w^2 = \left\langle \left(x(t) - \bar{x} \right)^2 \right\rangle = \frac{k_B T L}{12\bar{\beta}}, \qquad (2)$$

where L is the correlation length. The first part of this equation is the definition of w^2, and the second part is the relationship between the system length and w^2 for the PD limit fluctuations. Similar to calculating the correlation functions, here we also directly calculate w^2 from $x(t)$ and the results are the overage of more than 10 temporal pseudo-images for each step length. The results are shown in Fig. 4.

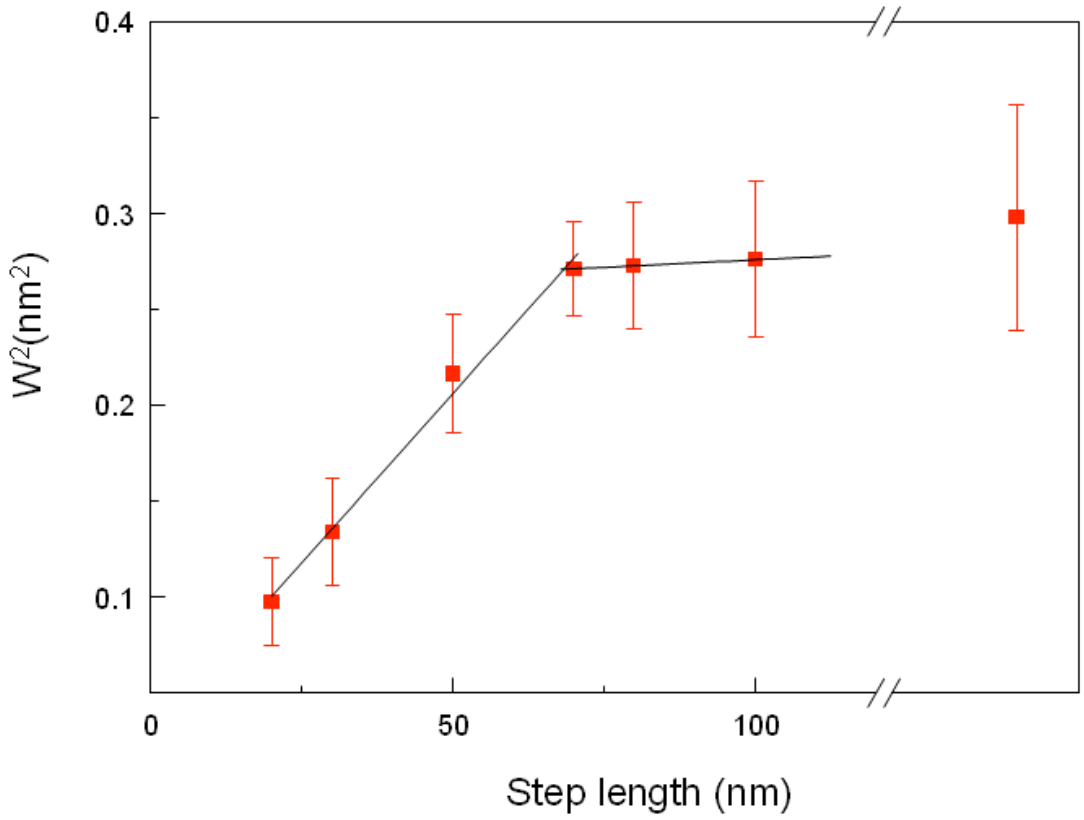

Fig. 4 (Color online) w^2 vs. step length. The black solid lines are linear fits of the data in two ranges. For step length from 20 to 70 nm, the best fit is $w^2=(0.0035\pm0.0002)\times l+(0.03\pm0.01)$; for step length from 70 to 100, the best fit is $w^2=(0.0002\pm0.000003)\times l+(0.25\pm0.0002)$. Here l denotes the step length.

From Fig. 4, we can see for steps shorter than 70 nm, w^2 linearly increases with the step length. When steps are longer than 70 nm, w^2 does not show obvious change, and the value is close to the corresponding value of free steps, which is the data after the break in the horizontal axis. According to the definition of the correlation length, for a pinned step, when its length is shorter than the correlation length, the correlation length should be the step length since the pinning points isolate any effect beyond the points. Of course, if the step length is longer than the correlation length, the pinning points do not affect the

correlation length. So the results in Fig. 4 clearly indicate at this temperature, the maximum correlation length should be ~70 nm. To determine the maximum correlation length, we fit the data in two ranges as shown in Fig. 4, and obtain the correlation length, the connecting point of the two linear fits, L_{max}=68 nm.

Furthermore, according to Eq. 2, another immediate result is the step stiffness $\tilde{\beta}$. Using the slope from the fit in the range that the step length is shorter than the correlation length, we can obtain the value of $\tilde{\beta}$, 841±48 meV/nm. This value is in excellent agreement with previous results measured through the temperature dependence of the equilibrium shape or the size dependence of island shape fluctuations by Ibach *et al.* [31, 96].

Conclusion

By analyzing the pinned steps on Ag(111) surfaces, we find the fluctuations of the pinned steps are still dominated by the periphery diffusion, and the maximum correlation length is 68 nm. This experiment also provides a method to measure the step stiffness without changing the sample temperature.

3.3 Fluctuations on Ag nanowires

Introduction

In recent years, semiconducting and metallic nanowires have been the subject of intensive research efforts. The small quasi-1D geometric structure and high surface-to-volume ratio make nanowires promising components in nanoscale electrical circuits and

chemical sensors [97-104]. For all these applications, especially the sensor applications, the morphological and chemical nature of the nanowire surfaces, including the presence of defects like steps and twin boundaries, play a crucial role in molecular-scale interfaces. In thin films, surface defects dramatically alter the stability of the films. For nanowires, it is likely that stability is an even more challenging issue when electrical current is flowing through the devices, causing electromigration and temperature change [105]. Therefore, defects on the surfaces of nanowires should be studied thoroughly; yet, there are few studies that directly probe the surfaces of nanowires at the atomic scale [106], and even fewer that focus on the dynamical and kinetic properties of the surfaces at this scale. The main difficulty comes from the measurement technology and how to clean the surfaces of these nanostructures. Most often, scanning electron microscopy (SEM) is used to characterize nanoparticles or nanowires in devices, but SEM does not have atomic resolution. Transmission electron microscopy (TEM) can provide near-atomic resolution and some information on shape fluctuations of nanoparticles [17, 18], but provides primarily projected cross-sectional information. In addition, an intrinsic disadvantage of TEM measurements for dynamics is that the electron beam can interfere with the thermodynamical and kinetic properties being measured. Due to its intrinsic surface sensitivity, mild tunneling conditions, high resolution and fast scan ability, scanning tunneling microscopy (STM) can overcome the above difficulties. Here we report the morphological and dynamical properties of surface defects of Ag nanowires measured using STM.

Experimental

The substrates for the experiment are Ag thin films made by thermal deposition, prepared as described in detail previously [32]. The Ag thin films are then transferred into the main chamber of the STM system (Omicron). After several sputtering and annealing cycles, the atomically clean Ag(111) surfaces are obtained. The Ag nanowire samples are prepared in water via a seedless, surfactantless wet chemical synthesis process as previously described [107]. As-prepared nanowires might have adsorbed water or salts on their surfaces. To improve cleanliness, the Ag nanowires are redispersed into spectroscopic grade methanol by centrifugation, with ~ 200 μM final Ag concentration. Using a pulse valve (series 9 pulse valve and IOTA ONE controller, Parker Inc.) [108], Ag nanowires are deposited from suspension onto atomically clean Ag thin films in a loadlock chamber, which is connected to the main chamber of the STM system. Then samples are transferred into the STM chamber, and slightly annealed at a temperature of about 120 °C for 10 minutes to remove methanol on the substrate and the surfaces of Ag nanowires. Characterization using STM is carried out at room temperature.

Results and discussions

Following deposition and cleaning, the distribution of nanowires is basically uniform. In our STM measurements, we observed isolated single nanowires, and also clumps, with density of about 0.2 to 5 nanowires per square micron. This approximate density is also confirmed by AFM and SEM measurements when samples were taken out from the UHV chamber after STM measuring. Large area survey STM scans are used to identify well-defined nanowires for quantitative study. Fig. 1a shows an STM image of Ag nanowires on the Ag substrate. The diameters of nanowires are around 20 nm. The lengths are

characteristically short, from 50 nm to hundreds nm. Survey images over large areas reveal nanowires with lengths in the range of 50 nm to a few micrometers. Long nanowires, especially with lengths on the micrometer scale are non-uniform in diameter along the longitudinal axis, and are likely to be polycrystalline. For simplicity, we chose short nanowires to study their surface features, as shown in Fig. 1a. The local topography of each nanowire shown in Fig.1a is characteristic. The ends of the nanowires are not rounded, but instead have facets joined at straight edges that meet at one top point. Furthermore, the line profiles of the cross section of nanowires are not curved, but have straight edges connected by jagged corners, as shown in Fig. 1b and 1c. On the left side of each nanowire shown in Fig. 1a and 1b, a "ghost image" appears. This is due to a "side tip" effect, which is often observed when measuring structures with large aspect ratio. To avoid this "side tip" effect and clearly characterize the surface features of side surfaces of nanowires, we reduce scan sizes and zoom onto the top of each nanowire.

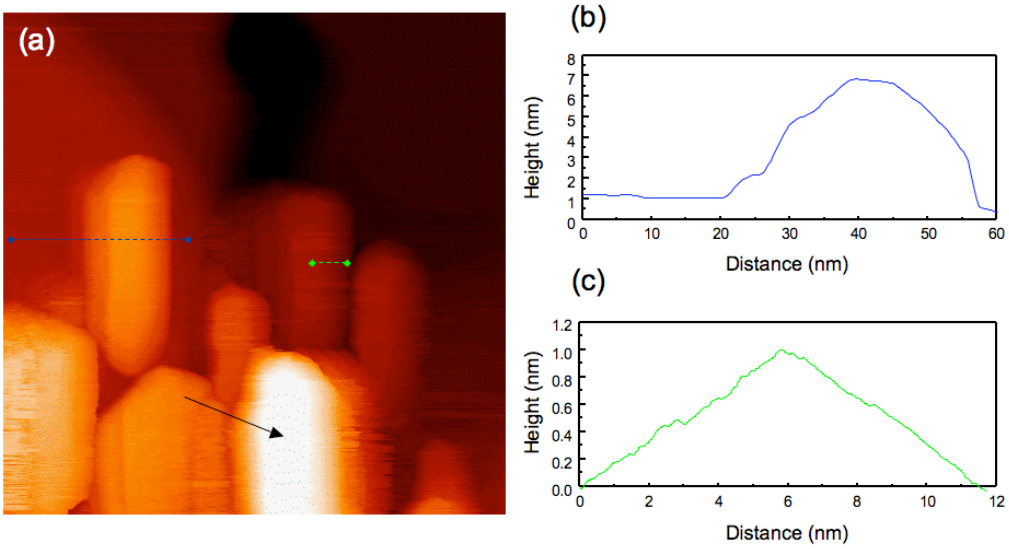

Fig. 1 (color online) (a) STM topography image, size 170 × 170 nm^2, of Ag nanowires on Ag substrate. The vertical range is 20 nm. The tunneling current is 31 pA with a sample bias of –

0.91 V. (b) and (c) line profiles of cross sections as marked by dashed lines with the same color in (a).

Figs. 2a-c show the topography images on the top of the nanowire, indicated by the black arrow in Fig. 1. The sawtooth structure shown in Fig. 2a is the highest point, and is the boundary between two adjacent facets. Fig. 2b and 2c, respectively, show the two neighboring facets by tilting the topography image of Fig. 2a. On both facets, monolayer steps (uncorrected height 0.15 nm) can be easily seen. In Fig. 2b, there is a monolayer adatom island. The rectangular shape suggests that this facet may be of (100) or (110) orientation, dramatically different from the hexagonal shape of the monolayer islands on the Ag(111) substrates at room temperature [109, 110]. The two tilted images also clarify the sawtooth structure in Fig. 2a as the result of neighboring monolayer or multilayer steps at the edges of the adjacent boundary, as shown in the 3D version in Fig. 2d. The sawtooth structure is most typically observed at the boundary between two neighboring facets. However, there are also sharper boundaries in Fig. 2e, which is a different section of the same nanowire as shown in Fig. 2a. The interfacial angle between the two facets is measured by calibrating the large height differences with the assumption that the nanowire's height is roughly equal to its width. The interfacial angle determined for the wire in fig. 2 is ~ 110°. This is consistent over measurements of different nanowires.

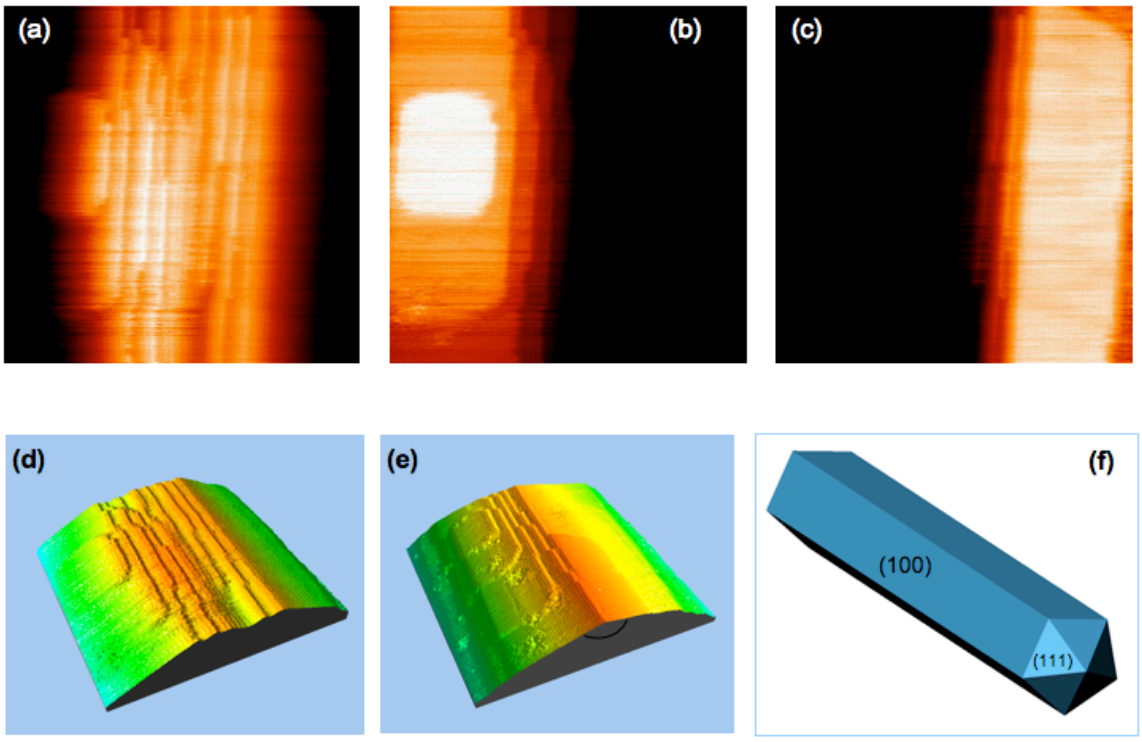

Fig. 2 (color online) (a) STM topography image, scale 20 × 20 nm^2, of the top of the Ag nanowire. (b) and (c) left and right facets on either sides of the region in (a) obtained by tilting the STM image in (a). (d) 3D rendering of (a). (e) image of another top section of the same wire. (f) Schematic drawing of a Ag nanowire.

Previous TEM studies on Ag nanowires have revealed that Ag nanowires are penta-twinned crystals with five (100) side faces and capped at both ends by five (111) faces [99, 107, 111]. The idealized 3D morphology of Ag nanowires is a pentagonally twinned prism with a pentagonal cross-section when viewed along the common [110] axis and five (111) twin boundaries arranged radially, as schematically shown in Fig. 2f. For a perfect pentagonal cross-section, the interfacial angle is 108°. Our STM topography images of most short nanowires show one facet boundary on top with an angle of 110°. This is in good agreement with a prism with a pentagonal cross-section, and one of its side faces contacting the substrate.

Surface defects, such as steps and facet boundaries, are usually the most active parts in chemical reactions [112, 113], and also dramatically affect the stability of the entire wire, especially at the nanoscale [114-116]. For these reasons, here we focus on the dynamics of steps and facet boundaries. In Figs. 2a-e, all the step edges appear frizzy, indicating temporal step fluctuations on the time scale of each line scan. To quantify step fluctuations, we use repeated STM scans over a fixed point on the step along the direction perpendicular to the step orientation, and obtain pseudo-images as shown in Fig. 3. The typical tunneling current is ~ 100 pA at the sample bias ~ – 1.0 V. Under these mild tunneling conditions the effects of tip-sample interactions have been shown to be negligible [23, 25, 32]. The line-scan length is 23.7 nm, and the line-scan time 0.2 s. For each pseudo-image, the total measurement time is 102.4 s with 512 lines. In Fig. 3, there are 4 steps. To avoid step-step interactions [117, 118], we choose the right-most step for analysis. Using image processing methods as described previously [32, 119], we extract the step position and then calculate the time correlation function $G(t) = \langle (x(t+t_o) - x(t_o))^2 \rangle_{to}$ for each image. The resulting correlation function, shown in Fig. 4, is averaged over more than 10 pseudo-images. By fitting the correlation function to $G(t) = G_0 \times t^n$, we obtain the exponent $n = 0.24 \pm 0.06$. This indicates the step fluctuations are determined by periphery diffusion, with the corresponding theoretical value of $n = 1/4$ [37]. This scaling exponent allows us to rule out the possibility that the facets are (110) oriented because Pai *et al.* [36] and Morgenstern *et al.* (31) have shown that at and below room temperature, step fluctuations on Ag(110) are dominated by adatoms leaving and attaching to the step edge rather than by periphery diffusion. In contrast, previous density functional theory (DFT) calculations for steps on Ag(100) surfaces have shown that the

diffusion barrier for adatoms along step edges is lower than the surface diffusion barrier (step edge barrier = 0.30 eV by the local density approximation (LDA) or 0.27 eV by the generalized gradient approximations (GGA), surface diffusion barrier ~ 0.52 eV by LDA or 0.45 eV by GGA) [120]. This calculation indicates step fluctuations on Ag(100) occur more readily by periphery diffusion than by processes that involve exchange of adatoms with the terrace. Consistently, previous experimental studies on submonolayer homoepitaxial islands on Ag(100) surfaces have shown that the island diffusion is dominated by periphery diffusion [121]. Thus, our fluctuation measurements are consistent with the TEM observations of (100) oriented facets on the nanowires.

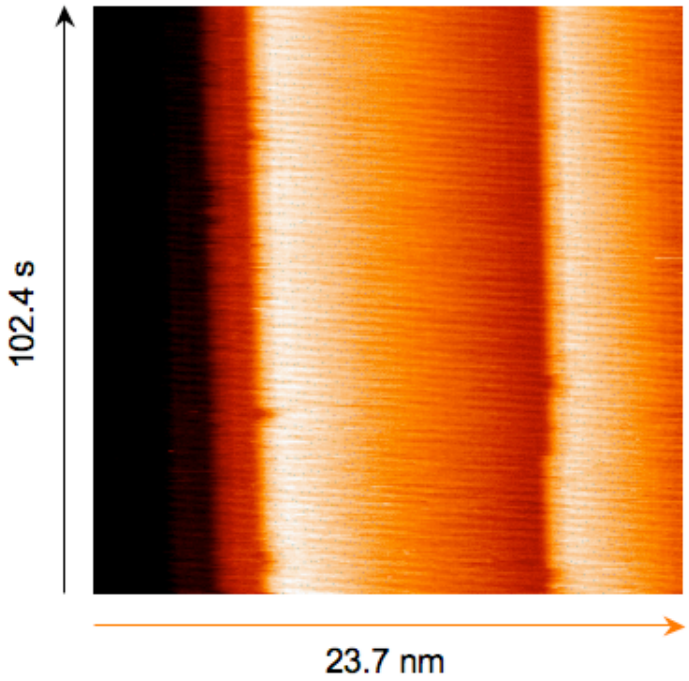

Fig. 3 (color online) STM pseudoimage obtained by scanning the tip repeatedly across a fixed position on the step-edges on a facet of a Ag nanowire. The line-scan length is 23.7 nm, and a line-scan time 0.2 s. Total time is 102.4 s with 512 lines. The tunneling current is I = 93 pA at a sample bias U_s = – 0.95 V. The mean squared width of the step edge is 0.009 ± 0.004nm^2.

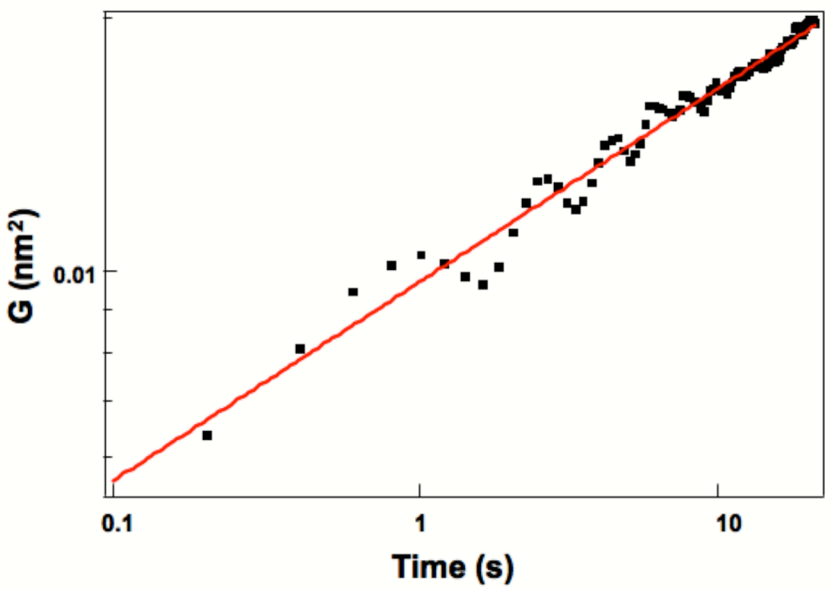

Fig. 4 (color online) Time correlation function of step fluctuations. The solid red line is the power law fit for the experimental data, $G(t) = G_0 \times t^n$. The best fit yields G_0 = 0.01 ± 0.001 nm^2s^{-n}, and n = 0.24 ± 0.06.

Since the step fluctuation is dominated by the periphery diffusion, according to the fitting value of the prefactor of the correlation function, G_0, we can further estimate the step mobility and the hopping time constant of the adatoms along the step edges. For periphery diffusion limited fluctuations, $G(t) = \left(\frac{2\Gamma(3/4)}{\pi}\right)(k_B T)^{3/4}\left(\frac{\Gamma_h}{\tilde{\beta}^3}\right)^{1/4} t^{1/4}$, where Γ_h is the step mobility and $\tilde{\beta}$ the step stiffness (29). Using the fitting value of G_0, we can immediately obtain $\left(\frac{\Gamma_h}{\tilde{\beta}^3}\right)^{1/4}$ = 0.20 $nm^2s^{-1/4}ev^{-3/4}$. According to the terrace-step-kink (TSK) model, the step stiffness $\tilde{\beta} = \frac{2k_B T}{a}\sinh^2(\varepsilon_k / 2k_b T)$ (where a is the lattice constant and ε_k the kink energy) and the calculated kink energy ε_k = 102 meV for a Ag(100) surface (33, 34), $\tilde{\beta}$ is 2.05 eV/nm. Then step mobility can be estimated as 0.0135 nm^5/s.

For periphery diffusion limited fluctuation, we also know the hopping time, $\tau_h = \frac{a^5}{\Gamma_h}$ (29).

So we can further calculate the hopping time, τ_h = 0.15 s. Both the step mobility and the hopping time are pretty consistent with the rates of island diffusion (10^{-1} to 10^{-2} Å^2/s) on Ag(100) at room temperature (35).

Conclusion

We have demonstrated that atomically clean Ag nanowires can be prepared and imaged using STM. The results confirm the overall shape and crystallography of the nanowires, previously determined via TEM, and also provide direct information about the nanoscale morphology and variability of the nanowires. The nanowires have well defined steps and facets, and thus are amenable to prediction of shape evolution using the continuum step model. The dynamical properties of the steps are consistent with the behavior of steps on macroscopic surfaces, confirming that properties measured on clean surfaces may be used directly in predicting the behavior of nanowires. In particular, the step fluctuation measurements on these Ag nanowires show that the dominant mass transport mechanism at room temperature is periphery diffusion, e.g. diffusion of Ag atoms along the step edges. The time constant measured for periphery diffusion at room temperature can be combined with the activation energy from previous DFT calculations to predict mass transport rates at different temperatures.

Chapter 4 Fluctuations of molecule/metal interfaces

In this chapter we first will discuss how local organic molecules, C_{60}, affect fluctuations of bare steps on Ag(111). Then we will analyze how molecules change the equilibrium shape of the decorated islands, and finally concentrate on the dynamic properties of the molecule/metal interfaces. These works have been published in Physical Review B (*Chenggang Tao, T. J. Stasevich, T. L. Einstein, and E. D. Williams, Step fluctuations on Ag(111) surfaces with C_{60}, Phys. Rev. B 73, 125436 (2006)*) and Nano Letters (*Bo Xu*, Chenggang Tao*, William G Cullen, Janice E Reutt-Robey, Ellen D Williams, Chiral symmetry breaking in two-dimensional C_{60}-ACA intermixed systems, Nano Letters 5(11), 2207 (2005) *Contribute equally to this work*).

4.1 Fluctuations of steps "pinned" by C_{60}

Introduction

The challenge of nanoscience is to identify and exploit unique materials properties that arise due to nanoscale size. Here we consider a novel possibility: the application of an immobile adsorbate to confine structural waves at nanometer length scales. Specifically, the system consists of monolayer-high steps (a boundary on a surface where the height changes by one atomic layer) on Ag(111). At room temperature, the step-edge fluctuates due to thermal motion of the Ag atoms along the edge of the step. The motion includes all

the wavelengths accessible to the line within the correlation length [32, 122]. The time constant τ_q for the evolution of each wavelength $\lambda = 2\pi / q$ is $\tau_q = kT / 2\Gamma_n \tilde{\beta} q^4$, where $\tilde{\beta}$ is the step stiffness, related to the line tension, and Γ_n is the atomic mobility that underlies the step motion [122]. If step motion is 'pinned', the maximum wavelength possible should be fixed at twice the distance between the pinning sites. In this work, we have investigated the physical nature of the size-limiting boundaries by using the preferential adsorption of C_{60} at step edges on Ag(111) to attempt physical confinement of step motion.

C_{60} on metal surfaces has been studied extensively [123-126]. At room temperature, on Ag(111) surfaces C_{60} films grow in a layer-by-layer manner with nucleation occurring at steps, followed by growth from steps onto both lower and upper terraces. C_{60} adlayers form a close-packed hexagonal structure of $2\sqrt{3} \times 2\sqrt{3}R30^\circ$ periodicity with respect to the substrate. We use C_{60} molecules at very low coverage (<1%) to create regions of bare step edges of variable lengths. By directly measuring the temporal variation of the "pinned" step edges, we evaluate the effects of nanoscale structural confinement.

Experimental

The Ag(111) thin film preparation method has been described previously [32]. In an UHV chamber (base pressure < 10^{-10} torr), Ag(111) thin films are sputtered and annealed. After several cycles, surfaces become atomically clean, as confirmed by both LEED and STM. Under proper annealing conditions, step edges on the surface are well isolated from each other and have lengths up to 1 or 2 μm. C_{60} is evaporated from powder in a PBN

crucible at deposition rate 0.01 ML/min, with the clean Ag(111) film held at room temperature. At low coverage, C_{60} molecules bind at the step edges and then nucleate small, close-packed islands, as shown in Fig. 1. At lower coverage, steps on the Ag(111) surfaces are only partly covered by C_{60}. Fig. 2 and Fig. 3 are STM topography images, in which the bright dots along step edges indicate C_{60} molecules. In Fig. 3, the frizzy bare part of the step between C_{60}-covered regions clearly indicates fluctuation [34, 127]. By controlling the annealing conditions and C_{60} coverage, the length distribution of the bare step region between C_{60}-covered regions can be readily changed.

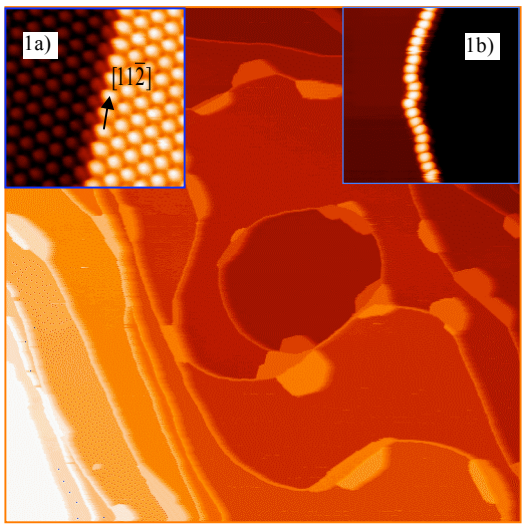

Fig. 1 (Color online) C_{60} chains and small islands along step edges on Ag(111) surface (400 nm × 400 nm, I = 30 pA, V = -2.05 V. Inset 1a, 10 nm × 10nm. Inset 1b, 15 nm × 15 nm)

Fig. 2 (Color online) STM topography image of the Ag(111) surface with C_{60} molecules partly covering step edges (1000 nm × 1000 nm, I = 110 pA, V = -1.54 V. Inset, 400 nm × 295 nm).

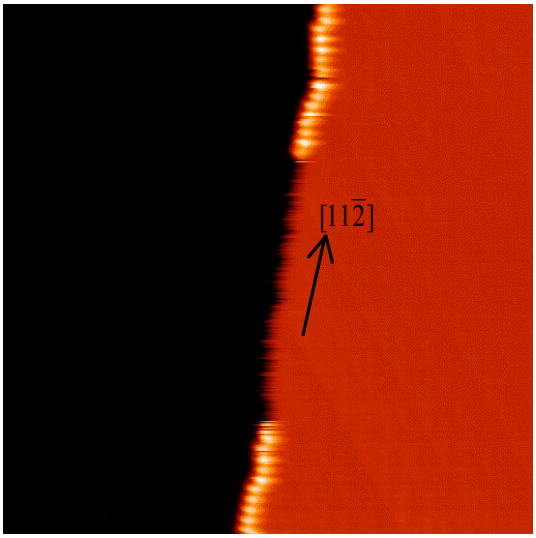

Fig. 3 (Color online) STM topography image of the monatomic steps on the Ag(111) surfaces partly covered by C_{60} molecules (40 nm × 40 nm, I = 97 pA, V = -1.61 V).

For observation of step fluctuations, we use repeated STM scans across a fixed position at the step boundary, at the mid-point between the two ends of a bare segment of step-edge. The tunneling current is 0.10 to 0.12 nA, and sample bias 1.50 V. Under these tunneling conditions the tip-sample interactions can be negligible for Ag surfaces [25, 32]. An example of a resulting pseudoimage is shown in Fig. 4. For all data in this paper, the time interval between scan lines is 0.0512 s, and the total measurement time is 102.4 s with 2000 line scans. This pseudoimage directly shows the magnitude of the edge fluctuations is up to ~ 0.6 nm. Fifteen to twenty sets of *x(t)* data are measured for each step segment.

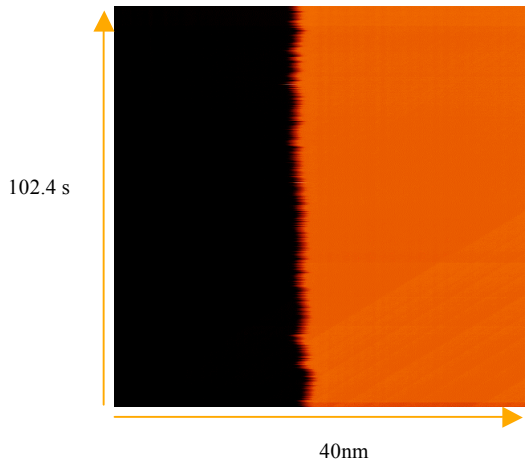

Fig. 4 (Color online) STM pseudoimage obtained by scanning the tip repeatedly over the middle point of the bare step-edge. The line scan length is 40 nm, and a line-scan time is 0.0512 s. Total time is 102.4 s with 2000 lines. The tunneling conditions are I = 97 pA, U = -1.61 V. The step orientation is along close-packed direction.

In order to extract the step-edge position *x(t)*, we flatten the image for the upper or lower terrace, and then identify the step point at which surface height is midway between the heights of the upper and lower terrace heights. The individual *x(t)* data sets are used

to calculate individual correlation and autocorrelation functions. The reported correlation and autocorrelation functions are averages of more than fifteen individual measurements.

Results and analysis

When the C_{60} coverage is 4~5%, C_{60} molecules fully cover step edges and form small islands along step edges, as shown in Fig. 1. Insets 1a and 1b show, respectively, C_{60} islands that cross over step edges and C_{60} chains along step edges. As shown in inset 1a, the C_{60} arrangement reveals the orientation of the underlying step edge, which in this case is known to be along the low-symmetry $[11\bar{2}]$ direction of the substrate, as indicated by the arrow. At lower coverage (< 1%), step edges on the Ag(111) surfaces are partly covered by C_{60}. On meandering step edges, C_{60} molecules are observed to avoid step edges along the close-packed direction of the substrate (e.g., step parallel to $[1\bar{1}0]$ direction) and cover those parts deviating from the close-packed direction. When checking STM topography images with Ag vacancy islands partly covered by C_{60} molecules, as shown in the inset of Fig. 2, we also clearly see this property on both long meandering steps and step edges of the near-hexagonal islands. To perform our measurement, we chose step segments with different lengths between adjoining C_{60} regions. Most of the larger step segments are along the close-packed directions of the substrate. However, shorter segments were found primarily at lower-symmetry orientations, as could be expected based on the C_{60} growth mode at low coverage.

In Fig. 3, the uncovered part of the step clearly reveals the presence of temporal fluctuations by the frizzy appearance. However, the C_{60} molecules appear motionless

according to STM topography images (viz. the position is invariant from scan to scan), and look like pinning points on the step edges. In order to find out how the C_{60} molecules affect the step fluctuations, we measured steps with different bare lengths, from 10 nm to more than 100 nm.

The basic theory to describe the fluctuations of the step is Langevin analysis using the continuum step model. Each degree of freedom of the step is assumed to diffuse towards lower energy with a speed proportional to the gradient of the energy, while random thermal noise tends to roughen the step edge. In general, the Langevin equation can be written as:

$$\frac{\partial x(y,t)}{\partial t} = -\frac{\Gamma_n}{kT}\frac{\delta H}{\delta x} + \eta(y,t), \qquad (1)$$

where Γ_n represents the step mobility, H the Hamiltonian for the step, and $\eta(y,t)$ the thermal noise. The thermal noise can be uncorrelated or correlated depending on the limiting types of step fluctuations. One is attachment-detachment limited fluctuations that are caused by mass exchange between the steps and terraces. In this case, the thermal noise is uncorrelated. Another type of step fluctuations is caused by step-edge diffusion. Since atoms can only hop from one site to another on the step edge, the thermal noise is correlated. Previous studies have shown that step fluctuations on bare Ag(111) surfaces are governed by step-edge diffusion [25, 32, 96]. For this case, the Langevin equation becomes:

$$\frac{\partial x(y,t)}{\partial t} = -\frac{\Gamma_n \tilde{\beta}}{kT}\frac{\partial x^4(y,t)}{\partial y^4} + \eta(y,t), \qquad (2)$$

with $\langle \eta(y,t)\eta(y',t') \rangle = -2\Gamma_h \delta(t-t')\delta''(y-y')$ and $\Gamma_h = a_\perp^2 a_\parallel^3 / \tau_h$, where $a_\parallel$ ($a_\perp$) is the lattice constant parallel (perpendicular) to the step edge, and τ_h the hopping time.

As described in the experimental section, from pseudoimages we can extract the temporal vibration of the step edge, which is the step-edge position *x(t)*. From *x(t)* we can calculate the time correlation functions *G(t)* and autocorrelation functions *C(t)* defined by, respectively:

$$G(t) = \langle (x(t) - x(0))^2 \rangle , \qquad (3)$$

$$C(t) = \langle [x(t) - \bar{x}][x(0) - \bar{x}] \rangle . \qquad (4)$$

The results for a step with a bare length of 51.0 nm between C_{60} molecules are shown in Figs. 5a and 5b. According to the above Langevin description of the dynamics [12, 32, 128, 129], *G(t)* and *C(t)* can be expressed as follows:

$$G(t) = \left(\frac{2\Gamma(1-\frac{1}{n})}{\pi} \right) \left(\frac{k_B T}{\tilde{\beta}} \right)^{\frac{n-1}{n}} (\Gamma_n t)^{\frac{1}{n}} = G_0 t^{\frac{1}{n}}, \qquad (5)$$

$$C(t) = C(0) \left((e^{-t/\tau_c}) - \Gamma(\frac{n-1}{n}, \frac{t}{\tau_c})(\frac{t}{\tau_c})^{1/n} \right), \qquad (6)$$

$$C(0) = \frac{kTL}{2\pi^2 \tilde{\beta}}, \qquad (7)$$

$$\tau_c = (\frac{L}{2\pi})^n \frac{k_B T}{\Gamma_n \tilde{\beta}}, \qquad (8)$$

where Γ is the gamma function, τ_c the correlation time, Γ_n the step mobility, and L is the system size which is also often identified as l_{corr}, the correlation length, over which correlated motion can be observed. Step fluctuations on Ag(111) surfaces are governed by step-edge diffusion, and n = 4 [25, 32, 84]. By using Eqs. (5) and (6) to fit the experimentally determined *G(t)* and *C(t)*, we can calculate values of *C(0)*, τ_c and the pre-exponential factor of *G(t)*, which is denoted as G_0 in Eq. (5). In order to determine diffusion type for these steps partly covered by C_{60} molecules, we fit all the correlation functions using Eq. (5). The average value of the measured exponents 1/n is 0.23 ± 0.02. This clearly shows that the fluctuations of steps with C_{60} molecules are dominated by step-edge diffusion, the same as for the fluctuations of steps on bare Ag(111) surfaces. For more precise comparison of G_0, then we fix the exponent at 1/4 to fit the correlation functions. In Fig. 5a, the fit (solid blue line) shows the time correlation function scales very well as $t^{1/4}$ up to a length scale of $\sqrt{G(t)} \sim 0.3$ nm for the 51 nm step. Fig. 5b shows the corresponding autocorrelation function and fitting curve, from which we can extract C(0) and τ_c. The results are shown in Fig. 6, in which we can see that τ_c does not show any obvious dependence on step lengths or step orientations. A linear fit to τ_c yields a slope of 0.034 ± 0.056 s/nm, indicating no significant functional dependence on step lengths. The simple average of the measured correlation times yields $\tau_c = 10.6$ s. This is equal to 1/9.7 times the measurement time as also observed for steps without C_{60} [32] However, G_0 depends strongly on step orientations, with values for steps along the close-packed directions consistently smaller than those of misorientated steps. Since G_0 represents the magnitude of step fluctuations, this indicates that fluctuations of steps

along close-packed directions (we define that the step angle $\theta = 0$) are smaller than fluctuations of steps along low-symmetry directions. A possible explanation is the orientational variation of the step stiffness [130]. Close-packed steps are expected to be stiffer than misorientated steps. Another possible contribution to this orientation dependence of G_0 is the step mobility.

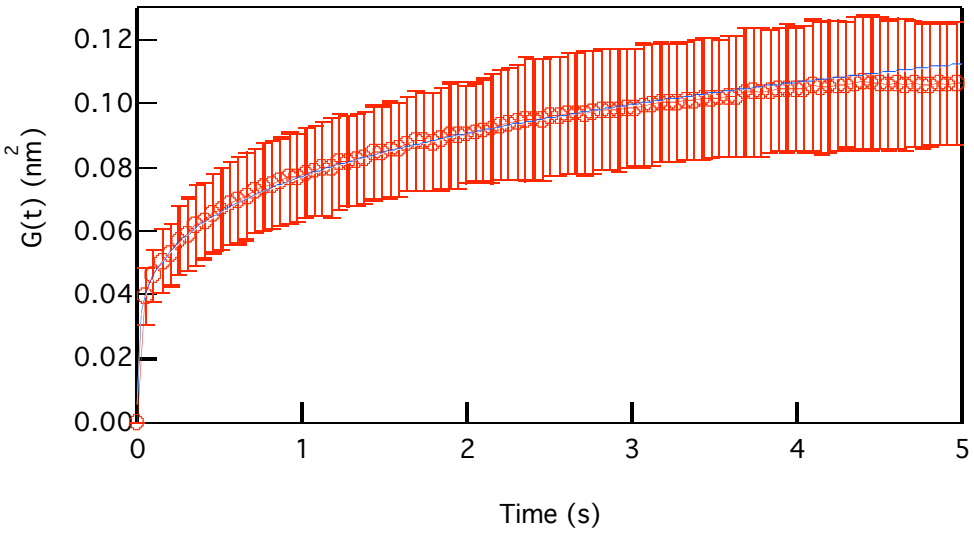

5a

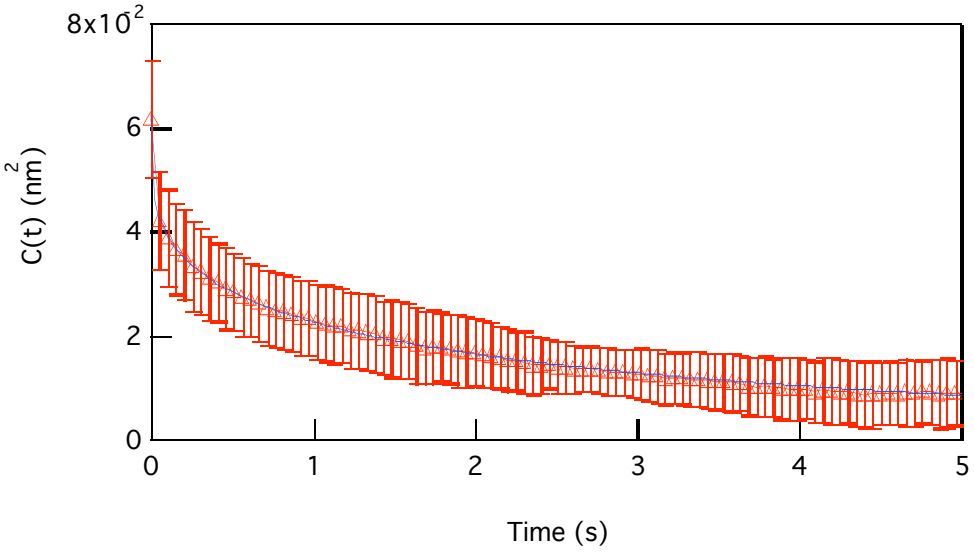

5b

Fig. 5. (Color online) Typical C and G curves and fit curves. In both figures, Solid lines (blue), fitting curves using Eq. (5) and (6). The best fit values are $C(0) = 0.0627 \pm 0.0002$ nm^2, $\tau_c = 11.26 \pm 0.10$ s, $G_0 = 0.0713 \pm 0.0005$ nm^2. The error bars shown are the standard deviation of the average over 12 sets of x(t) data, all measured on the same step segment.

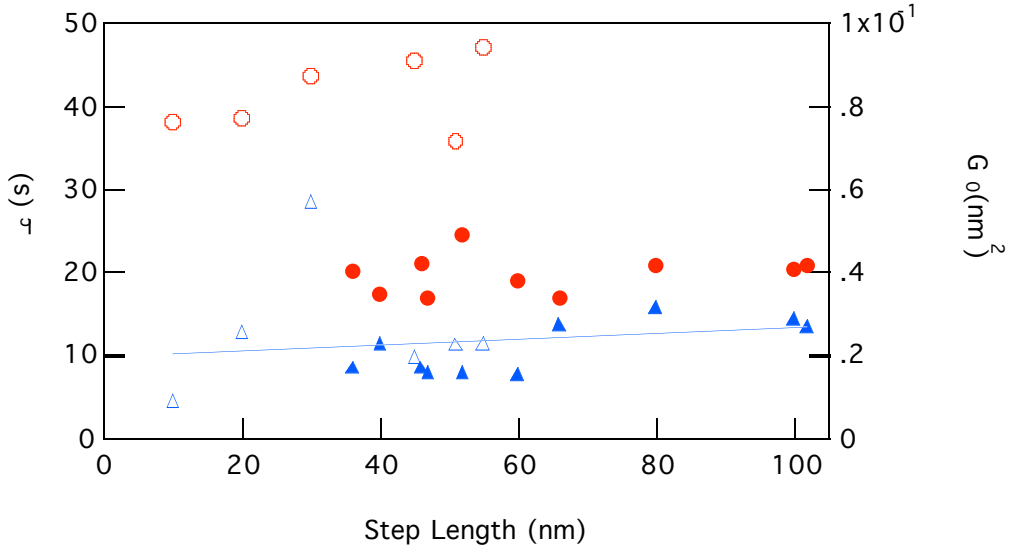

Fig. 6. (Color online) G_0 (right axis) and τ_c (left axis) vs. Step lengths. Circles (red), G_0 with solid circles for close-packed steps and open circles for misorientated steps. Triangles (blue), τ_c with solid triangles for close-packed steps and open triangles for misorientated steps. The deviation angles for steps deviating from close-packed direction were: $l = 10$ nm, $\theta = 8^\circ$; $l = 20$ nm, $\theta = 26^\circ$; $l = 45$ nm, $\theta = 14^\circ$; $l = 55$ nm, $\theta = 17^\circ$. Solid line (blue), linear fit for τ_c.

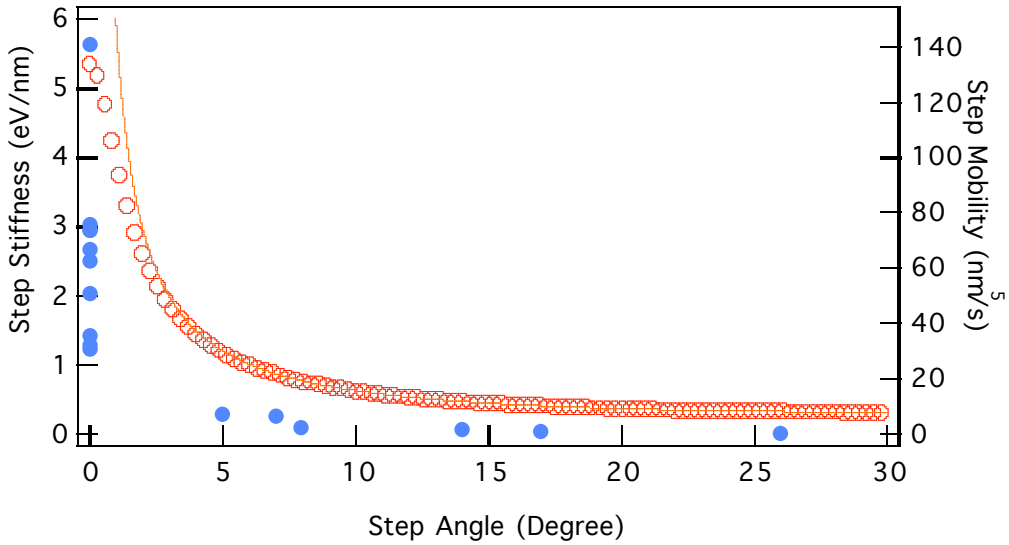

Fig. 7 (Color online) Step stiffness (left axis) and step mobility (right axis) vs. Step orientation. Solid line (red), low temperature step stiffness as a function of the step angle (Eq. 9); open circle (red), exact step stiffness. Solid circles (blue), experimentally determined step mobility.

Recently experimental and theoretical studies have shown that the Ag(111) step stiffness $\tilde{\beta}$ is a strongly varying function of the step orientation for small step angles at room temperature [19, 130, 131]. At this temperature, corresponding to roughly $T_c/8.5$, the exact form is well approximated by a remarkably simple equation [130, 132]:

$$\frac{k_B T}{\tilde{\beta}(\theta) a} = \frac{\sin(3\theta)}{2\sqrt{3}} \qquad (9)$$

The corresponding angular dependence of the stiffness is shown as the solid red line in Fig. 7. The validity of this equation only breaks down for steps oriented very close to the high-symmetry direction (where θ ranges from 0 to 2 degrees). Because these steps are experimentally very difficult to distinguish from high symmetry steps, their stiffness is most easily fit to the exact high-symmetry result [130, 132]:

$$\frac{k_B T}{\beta(0) a_{\parallel}} = \frac{3}{2} \frac{\sqrt{3+2f}-1}{\sqrt{2(3+2f)(f-\sqrt{3+2f})}} \qquad (10)$$

where $f = (1+3z^2)/[2(z-z^2)]$ and $z = 3^{-Tc/T}$. This result is shown as the red open circle at $\theta = 0$ in Fig. 7. Eq. (10) represents the stiffness maximum, so it will generally over-estimate the experimental step stiffness. The exact solution for the full orientation dependence of $\tilde{\beta}(\theta)$ can be numerically evaluated and is shown as red open circles in Fig. 7. Given the stiffness, it is immediately possible to calculate the step mobility from the measured values of G_0. The result is shown as blue solid circles in Fig. 7. The step mobility shows step orientation dependence similar to that of the step stiffness. For misorientated steps, covering an angular range from 5 to 26 degrees, the values of the step mobility are essentially constant, and much less than those of steps orientated along the close-packed direction. The range of measured values of the step mobility for the nominally close-packed steps is likely because the step mobility is very sensitive to small changes in the angle. To quantify this observation, the hopping time for the fluctuations caused by the step diffusion can be expressed in terms of Γ_h, $\alpha_{\parallel}$ and $a_{\perp}$: $\tau_h = a_{\perp}^2 a_{\parallel}^3 / \Gamma_h$. Using the average measured values of Γ_h for close-packed steps and misorientated steps,

we can roughly determine the corresponding hopping time. For close-packed steps, the hopping time constant is ~ 31 μs. For misorientated steps, the hopping time constant is ~ 704 μs, about twenty times larger than that of the close-packed steps.

Given $\tilde{\beta}$, it is straightforward to calculate the values of the system size (or correlation length) for steps with different lengths. According to Eqs. (5) and (8) with n = 4, the system size L can be expressed in terms of G_0, τ_c, $\tilde{\beta}$ and T:

$$L = \left(\frac{\pi^2 \tilde{\beta}}{k_B T \Gamma(\frac{3}{4})} \right) \tau_c^{\frac{1}{4}} G_0 . \qquad (11)$$

The results are shown as circles in Fig. 8. Using Eq. (7) to determine the system size yields similar results. The ratios of the system size from Eqs. (7) and (11), L_7/L, are consistently near one, with average value 1.17 ± 0.10. The dashed line in Fig. 8 shows the simplest expectation that L equal the step length. It is clear that the measured system sizes do not have a simple proportional dependence on the step length. In fact, there are two distinct regions, the first corresponding to close-packed steps (solid circles), and the second to misorientated steps (open circles). For both regions, the system sizes show at most weak dependence on the step lengths, with a slope of 0.42 ± 0.57 for close-paced steps, and slope 0.23 ± 0.13 for low-symmetry steps (solid lines in Fig. 8). However, the values of L of the close-packed steps longer than those of the misorientated steps. The observed values of L are consistent with correlations limited by the measurement time,

$\tau_c = t_m / A$, with A = 9.7. This is the same behavior observed for steps on clean Ag surfaces where there are no apparent pinning sites at the step edge.

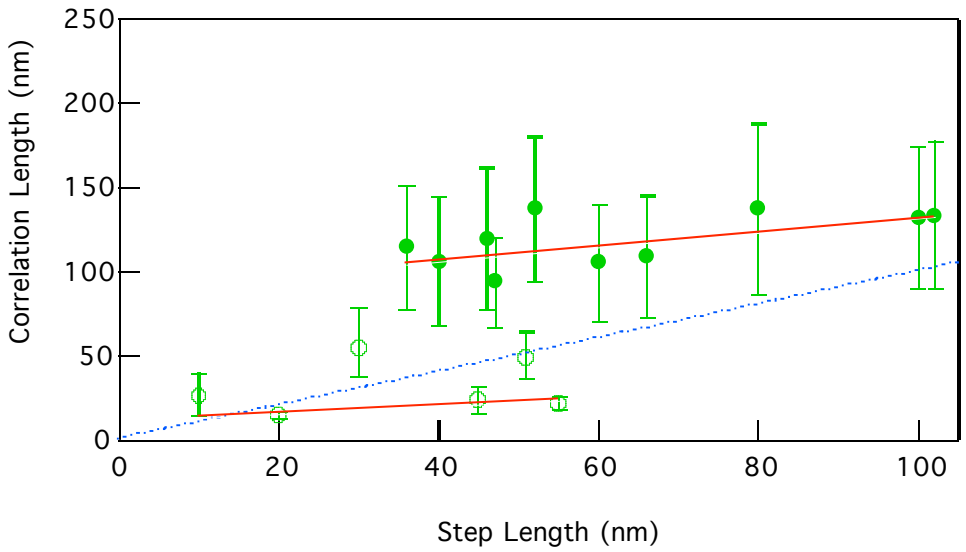

$L = a+b*l_{step}$

a = 88 ± 35, b = 0.42 ± 0.57

a = 11 ± 4, b = 0.23 ± 0.13

Fig. 8. (Color online) Correlation lengths vs step lengths. Circles (green), experimentally determined correlation lengths with solid circles for steps orientated along close-packed direction and open circles for steps deviating from the close-packed direction. Dash line (blue), step lengths. Upper solid line (red), linear fit for the correlation lengths of the steps orientated along the close-packed direction with coefficients a = 88 and b = 0.42. Lower solid line (red), linear fit for the correlation lengths of the steps deviating from the close-packed direction with coefficients a = 11 and b = 0.23.

Discussion and conclusions

In summary, we have found that for C_{60} growth model along step edges, steps of orientation along the $[11\bar{2}]$ direction are the most adhesive for C_{60}, while step edges orientated along close-packed directions are less likely to bind C_{60}. The average value of the measured exponent for the correlation function *G(t)*, 0.23 ± 0.02 for steps of both orientation. This clearly shows the fluctuations of steps decorated with C_{60} molecules are dominated by step-edge diffusion as are clean steps. Our results further indicate for the step-edge diffusion case, the step mobility exhibits strong step orientation dependence. This is in contrast to the attachment-detachment dominated case on Ag(110), in which the step mobility does not depend appreciably on the step orientation [133]. In a simple lattice model [25], the hopping time is directly determined by the effective activation barrier energy E_a, which is related to the kink energy ε_k and the true diffusion barrier E_h: $E_a = (3/4)\varepsilon_k + (1/4)E_h$ [32, 96]. The difference of hopping times for close-packed steps and misorientated steps indicates that hopping along the misorientated steps has larger effective activation barrier energy. This is a reasonable result, according to an intuitive explanation that both the kink density and the effective diffusion barrier are larger for misorientated steps.

The results of the measured system sizes (or correlation lengths) consistently show little dependence on the step lengths, but do depend on the step orientations. As shown in Fig. 8, the measured correlation lengths are almost constants for the close-packed steps and the misorientated steps, respectively. Formally these characteristic lengths should be determined by the system length. Considering a step edge with two

pinning points at ends, the length of the step edge should determine the system size. In our measurements, the step lengths between C_{60} sites range from 10 nm to ~100 nm. If the C_{60} molecules were real pinning points, the characteristic lengths would show step length dependence. Instead the measured correlation length for high-symmetry steps is consistently larger than the C_{60}-C_{60} separation, and the values of the length are consistent with fluctuations limited by the measurement time [1] for both high and low-symmetry step edges. Thus, the results indicate that C_{60} molecules are NOT acting as pinning points on the step edges.

Previous studies of C_{60} on Au(111) and Ag(111) surfaces have revealed that the C_{60}-substrate interactions are considerable due to surface states [123, 134-136]. For C_{60} on Ag(111), the adsorption energy is 1.5 eV, consistent with a small amount of charge transfer from the Ag(111) film to the C_{60} molecules. The interaction between C_{60} molecules and step edges is apparently stronger (enough to constrain C_{60} to step edges), in agreement with the observation that no individual C_{60} molecules were on terraces at room temperature. Considering the geometry of step edges of (111) surfaces and C_{60}, the zigzag shape of steps along the $[11\bar{2}]$ direction provides perfectly match for the natural lattice constant of C_{60} molecules, which can thus align into close-packed chains along step edges. There is no detectable C_{60} motion once C_{60} molecules have connected into chains along the step edges, suggesting that the near-neighbor intermolecular attraction hinders C_{60} movement. More details about the distribution of C_{60} on the step edges will be discussed elsewhere.

In our measurement time range, C_{60} molecules remain at fixed positions and show no scan-to-scan variability. However the quantitative step fluctuation features indicate

that C_{60} molecules are not acting as pinning points that would limit the correlation length of the step fluctuations. In order to understand why C_{60} molecules do not change step fluctuations, we need to consider not only the geometric effect of C_{60} molecules along the step edge, but also the local electron redistribution caused by C_{60} molecules. As discussed above, both previous experimental and theoretical studies confirm that there is charge transfer from Ag(111) surfaces to C_{60} molecules. Recent theoretical calculations provide further insight into the charge redistribution between Ag(111) surfaces and C_{60} molecules [135]. The interaction between C_{60} and the surface is primarily covalent, with some ionic character (0.5 electron transfer per C_{60} molecule). The largest electron accumulation occurs in the middle of the interface region between the C_{60} and the top surface layer. The electron accumulation in the interface region corresponds to a strong local electric field, similar to that considered in Feibelman's analysis on surface-diffusion on Pt(001) [137]. Feibelman showed that when an external electric field is oriented to pull electrons out of the metal, Pt adatoms gain charge and become more like Au. As a result, their bonds to the surface weaken, and therefore the diffusion barrier diminishes. It is reasonable to expect that the charge redistribution caused by C_{60} should also change adatom diffusion along the step edges, possibly enhancing it enough to compensate for geometric effects. The geometric effects are illustrated in Fig. 9, using a simple lattice model with the value of the distance from the edge of C_{60} molecules to the underneath surface and the nearest step edge 0.09 nm [135]. The resulting spacing show that maximum radius of adatoms that could hop through the gap between C_{60} and step edges is less than 0.1 nm, which is less than the radius of Ag atoms in the bulk, ~0.145 nm. This implies that possible Ag adatom diffusion could be constrained to substitutional motion

or diffusion around the C_{60} molecules on the neighboring terraces. For both possibilities, the geometric effects would suggest hindered adatom movement along the step edges. Overall the geometric effect and the charge redistribution effect by C_{60} molecules may counteract each other. This, or perhaps more exotic explanations of correlated motion [138], are needed to explain the surprising result that the C_{60} atoms at the step edges provide little or no restriction to the fluctuations of intervening step-edge segments.

More generally, our results show that C_{60} molecules have no detectable effect on mass transfer along a defect structure (step edge) on the Ag(111) surface. This conclusion is surprising, and opens the possibility that metal diffusion may also be facile under other electronegative organic molecules on metal surfaces [139]. This is very useful for nanometer scale device fabrication, in which mass transport on metal electrodes plays a key role.

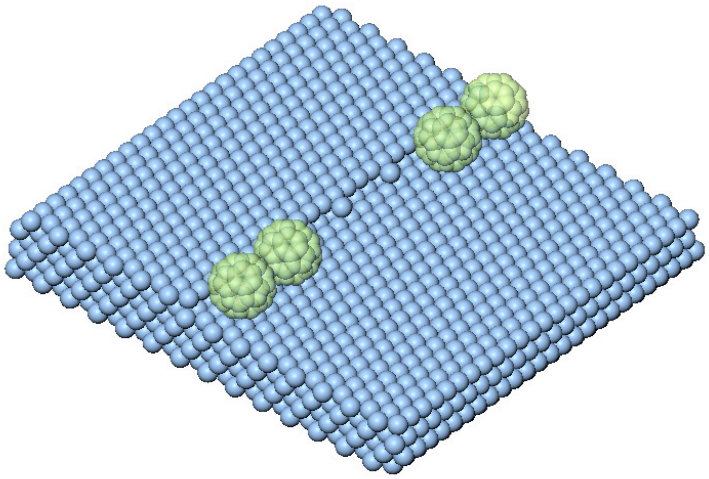

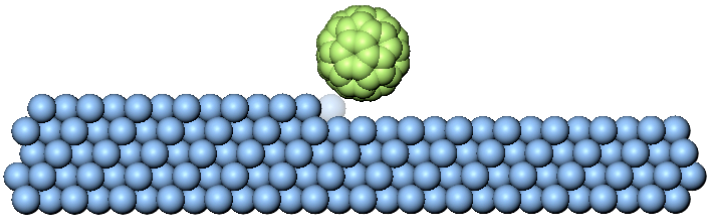

Fig. 9. (Color online) Schematic illustrations of the step with C_{60}. C_{60} molecules stay side by side to form chains along step edges, partly covering step edges.

4.2 Metal/molecule interface fluctuations

Introduction

Nanoscale electronics has attracted intense research interest, motivated in part by the potential use of single molecule conduction in electronic devices.[1, 2, 140] Substantial achievements in this area make it increasingly clear that a great challenge will be understanding and controlling the interaction between the active nanoscale elements and the conductive electrodes in the devices.[61, 141-144] Structural changes at the nanometer scale, involving the displacement of even a single metal atom, can greatly alter the electronic properties and reliability of the devices.[94, 145, 146] In order to shed light on this problem, we introduce a model system, a one-dimensional (1D) metal-molecule interface formed at Ag monolayer islands decorated by C_{60} molecules. Direct time-resolved imaging of this system using STM reveals the amplitude/frequency relationships for the motions of the Ag "electrode" and the C_{60} molecules at the interface.

Quantifying structural fluctuations is accomplished by using the continuum step model for interfaces to analyze time-dependent STM measurements.[66] Silver surfaces are known to display substantial structural mobility at room temperature,[29, 32, 147] resulting in correlated motion of extended structures such as pits and islands.[39, 148, 149] Carefully designed experiments allow the motion, shape and correlation functions of the interfaces of such structures to be determined.[67, 96, 150, 151] These reveal the time scale and amplitude of the fluctuations, which are in turn determined by the stiffness of the interface and the characteristic times for motion of the atoms at the interface.[66, 152-154] More complex systems, for instance the interfaces between molecules and metal surfaces, have not yet been investigated in this way. The adsorption of C_{60} on metal surfaces provides an ideal system for demonstrating the effects of fluctuations at a metal-molecule interface. Previous studies of C_{60} on metal surfaces have documented the characteristics of the adsorbed C_{60}, which include rapid diffusion at room temperature and preferential binding at structural edges such as steps and island boundaries.[119, 123, 126, 155] Experimental methods for preparing the surface and methods of image analysis have been presented previously,[119] and are synopsized in the supplemental materials.

Experimental

Ag(111) thin film preparation procedure has been described previously.[32, 86, 87] In a UHV chamber (base pressure $< 3 \times 10^{-11}$ torr), Ag(111) thin films are Ar-sputtered and annealed. After many cycles, surfaces become atomically clean, as confirmed by Auger, LEED and STM. Under proper annealing conditions, monolayer Ag islands are generated on the clean Ag(111) films. The size of islands ranges from several nm to more than 100

nm. The distributions of island size and density are sensitively related to the annealing conditions.

C_{60} is evaporated from powder in a PBN crucible with the clean Ag(111) film held at room temperature. Before deposition, we carefully degas the evaporator and the C_{60} containing crucible, so that during deposition, the pressure in the chamber never exceeds 1.0×10^{-10} torr. The deposition rate is ~ 0.01 ML/min. By controlling deposition time, the C_{60} coverage varies from only few C_{60} molecules on the whole surface to C_{60} molecules to fully covering steps and island edges. After deposition, the samples are transferred onto the STM stage in the same chamber.

The typical tunneling conditions are 0.07 to 0.11 nA at −1.55 to −1.75 V. To investigate the decorated island shape fluctuations, we employ relatively fast STM scans over individual islands to obtain ensembles of topography images at consecutive time. The fastest scan speed is 13.1 s per 256 × 256 pixel image and 26.2 s per 512 × 512 pixel image, respectively. Each ensemble contains 50 to several hundred sequential images. Via image processing methods, the position of each C_{60} molecule can be extracted, and the island shapes are digitized by the positions of all C_{60} molecules in the chains. The typical size of the decorated islands we investigated is from 20 nm to 50 nm in diameter. In our measurements, we find that the decorated islands in this size range do not have observable net motion across the surface of the film. For smaller decorated islands typically with size less than 10 nm, we do see island decay, in which the surrounding C_{60} rings shrink by coalescence, e.g. in which the total number of C_{60} molecules does not change.

Results and discussions

At room temperature, equilibrium monolayer islands on clean Ag(111) surfaces are hexagonal.[96] The island edges appear frizzy, indicating step-edge fluctuations. Previous experimental studies have shown that the edge fluctuations at and above room temperature are dominated by diffusion of Ag atoms along the periphery of the structure.[32, 96] When C_{60} molecules are deposited onto these surfaces, they bind preferentially at step edges, causing no observable change in the fluctuations of neighboring bare segments of the step edge.[119] By carefully controlling the deposition rate and time, we can generate islands with edges covered by precisely one closed single strand of C_{60}, as shown in **Fig. 1a**. These images reveal that both adatom islands and vacancy islands (supplemental **Figure S1** and **S2**) are covered by closed C_{60} chains one molecule wide, which we call C_{60} rings. In these images, we can also clearly see that the shape of the decorated islands larger than 20 nm is approximately circular. On closer inspection (supplemental **Figure S2c**), the C_{60} rings are not smooth circles with constant local curvature; some sections have higher curvature than others, and there are some tortuous structures indicating kinked configurations. Furthermore, as shown in **Fig. 1b** and **1c**, the images of some C_{60} molecules in the rings appear disjointed, indicating C_{60} molecules have moved between sequential scans. The temporal signature of such motion is illustrated in **Fig. 1d**. On the whole, the shape of the C_{60} ring fluctuates visibly on the time scale of sequential STM images, with a time scale substantially slower than the edges of undecorated Ag islands on clean Ag(111) surfaces.

Since the C_{60} rings are fluctuating at room temperature, we use STM to repeatedly scan relatively small decorated islands, as shown in **Fig. 2a**, to obtain a temporal

sequence of images (movie in supplemental **Movie S3**). The images are then processed to determine molecular positions, and one frame of such an STM image ensemble is shown in **Fig. 2b**, in which the blue dots represent the STM topography image of C_{60} molecules, and the orange dots are the digitized C_{60} positions. Both the island area and the number of C_{60} molecules in the surrounding C_{60} ring remain constant over the entire sequence of images, with total measurement time around 60 minutes. By averaging the images in a sequence, we obtain the mean shape of the decorated island (or the C_{60} ring), the equilibrium shape,[156] as shown in **Fig. 2c**. Distinctly different from the hexagonal shape of bare Ag islands, the equilibrium shape of the decorated island is almost perfectly circular, with an average C_{60}-C_{60} distance close to 1 nm. Such circular structures are expected to fluctuate in the normal modes of a circle as illustrated schematically in **Fig. 2d**. To obtain the kinetic properties of the decorated island, many sequential images are needed for longer total measurement time, and a shorter time interval for higher time resolution. To address these requirements, we analyzed a data set for a decorated island by a ring including N = 78 C_{60} molecules. The ensemble includes ~ 600 sequential images with a time interval of 13.1 s, for a total measurement time around 130 minutes. To determine the structural correlation functions, the edge of the ring is approximated by a series of measurements of the radius $R(\theta_n)$ at equally spaced angles, where $\theta_n = n\pi/N$ with N = 78, the number of C_{60} in the ring. To analyze the fluctuations, we subtract the equilibrium circular shape from each digitalized island shape, leaving a new series $r(\theta_n) = R(\theta_n) - \langle R \rangle$, where $\langle R \rangle$ is the radius of the equilibrium circle.

Given $r(\theta_n)$, we Fourier transform to determine the magnitudes r_k of the component Fourier modes:

$$r_k = \frac{1}{N} \sum_{n=-N/2+1}^{N/2} r(\theta_n) e^{ik\theta_n} . \quad (1)$$

Once we know r_k, it is straightforward to calculate correlation functions in the Fourier representation:[152, 153]

$$G_k(t) = \langle [r_k(t+t_0) - r_k(t_0)]^2 \rangle = A_k(1 - e^{-t/\tau_k}) , \quad (2)$$

where A_k is the mean squared amplitude of the radial fluctuations in the k^{th} mode, and τ_k is the time constant for the k^{th} mode. The correlation functions for modes 2-12 are plotted in **Fig. 3a**. Fitting the correlation functions to Eq. 2 yields the parameters A_k and τ_k.

Both the amplitude and the time constant are expected to have a power-law dependence on the mode number k. Hence, we plot A_k vs. k and τ_k vs. k in **Fig. 3b**. We find the scaling relationship $A_k = (0.108 \pm 0.002) \times k^{-\alpha}$ nm^2 with $\alpha = 1.88 \pm 0.01$, consistent with the prediction of the Langevin analysis:

$$A_k = \frac{k_B T \langle R \rangle}{\pi \tilde{\beta} k^2}, \quad (3)$$

where $\tilde{\beta}$ is the decorated-edge stiffness. From Eq. 3 we determine $\tilde{\beta} = 0.65$ eV/nm. According to our previous study,[32] the edge stiffness of bare steps on Ag(111) at room temperature depends on step orientation. For steps deviating from the close-packed direction, the average experimental step stiffness is 0.67 eV/nm,[119, 130] which is similar to the above decorated-edge stiffness. On the other hand, **Fig. 3b** shows the scaling relationship $\tau_k \propto k^{-z}$ with $z = 1.85 \pm 0.05$, indicating that the decorated-island shape fluctuations follow the behavior expected for uncorrelated motion (z = 2, usually attributed to attachment-detachment (AD) kinetics). This is in stark contrast to the

correlated motion of Ag atoms on the bare Ag(111) step boundary, characterized by a z = 4 power law for the temporal fluctuations.

The scaling behavior of τ_k suggests that the fluctuations of the 1D Ag-C_{60} interface are governed by uncorrelated events, similar to the behavior observed for attachment-detachment kinetics at step edges. However, in this case the observed invariance of number of C_{60} molecules is inconsistent with exchange of C_{60} molecules between the ring and a diffuse phase beyond the decorated-island edges. Instead, the observed structural configurations suggest uncorrelated C_{60} displacements within the ring most likely involving molecular displacements as shown in **Fig. 1b** and **1c**. These quasi-kink local configurations are related to C_{60} molecules in the rings hopping approximately along the radial direction to a nearest stable position. This idea is confirmed by temporal line scans over individual C_{60} molecules (**Fig. 1d**). The displacements occur only between two discrete positions. The hopping displacement of 0.26 nm suggests registry to the underlying Ag lattice.

The distinct difference in the basic nature of the fluctuations of the underlying Ag-side of the interface, and the directly observed C_{60} ring indicate that motion of the C_{60} side of the interface is not strongly coupled to the underlying Ag motion. For the C_{60} ring fluctuations, using the theoretical values $\alpha = 2$ and $z = 2$, we obtain mode k and radius R dependence of A_k and τ_k: $A_k = (0.009\text{nm})(R/k^2)$ and $\tau_k = (11.5\text{nm}^{-2}\text{s})(R/k)^2$. In comparison, for bare Ag step edges, for which previously determined values for the step stiffness and hopping time constant are available,[32] the corresponding relationships are $A_q = 2k_BT/L\tilde{\beta}q^2$ and $\tau_q = k_BT/\Gamma_h\tilde{\beta}q^4$, respectively, where L is the system length and q is the wavenumber.[66] If step edges are considered as closed interfaces, we can equate the

system length with the perimeter of the circular boundary, unifying the formulas for both step edges and islands. Since $L = 2\pi R = k\lambda$, and $q = 2\pi/\lambda = k/R$, then the squared-amplitude A_q and the time constant τ_q can be represented in terms of the mode number k as $A_k = k_B TR/\pi\tilde{\beta}k^2$ and $\tau_k = k_B TR^4/\Gamma_h\tilde{\beta}k^4$. The resulting formula for A_k for step edges is identical to Eq. 3. From our previous study,[119] the step mobility is $\Gamma_h = 2.86\ nm^5s^{-1}$, so for bare step edges around a circular boundary of radius R, $A_k = (0.012nm)(R/k^2)$ and $\tau_k = (0.0135nm^{-4}s)(R/k)^4$. Physical examples of the resulting time constant values for mode 4 are, for bare step edges, $Sqrt(A_4) = 0.09$ nm and $\tau_4 = 0.8$ s, while for Ag-C_{60} interfaces, $Sqrt(A_4) = 0.08$ nm and $\tau_4 = 120$ s. Compared with the effects of Ag atoms hopping along bare Ag step edges, the mode motion resulting from C_{60} molecular displacements is a slow process. Previous measurements of partially covered Ag steps have shown that the C_{60} molecules attached to island edges do not alter the Ag step fluctuations. This strongly suggests that in this system the underlying Ag step edge is fluctuating with at most weak correlation with the motion of the C_{60} overlayer. In this case, the independent motions of the Ag and the C_{60} will contribute to the electronic properties of the interface by creating fluctuations of the Ag-C_{60} separation, introducing signal variability with an amplitude spectrum (T = 300K) combining the silver signature $A_k\left(f_k = 1/\tau_k\right) = \frac{0.10nm^3}{R} f_k^{-1/2}$ and the C_{60} signature $A_k\left(f_k = 1/\tau_k\right) = \frac{8\times10^{-4}nm^3}{R} f_k^{-1}$. The effect on electron transport signals will be strongest where the amplitudes are largest, e.g. in frequency range (modes 4 - 12) of 1.3 to 105 Hz due to Ag motion, and 0.01 to 0.08 Hz due to C_{60} motion.

The ability to structure C_{60} molecules into rings decorating Ag islands provides a model system in which the observable collective fluctuations of the metal-molecule

interface can be readily interpreted in terms of fundamental time constants and free energies. It is shown here that the C_{60} rings decorating Ag islands provide a model to study the organic molecule/metal interface fluctuations. By analyzing the interface fluctuations, we obtain time constants corresponding to frequencies of 0.01-100 Hz and an amplitude for changes in the interface width of ~ 0.1 nm. Such interface fluctuations will directly impact the transport properties of nanoelectronic and molecular electronic devices that involve small area contacts between electrodes and the electronic material.[94] The approach presented here provides a quantitative method for characterizing the stochastic properties of electronic interfaces on the nanometer scale, and predicting the correlated frequency spectrum of the signature in electrical transport across the interface.

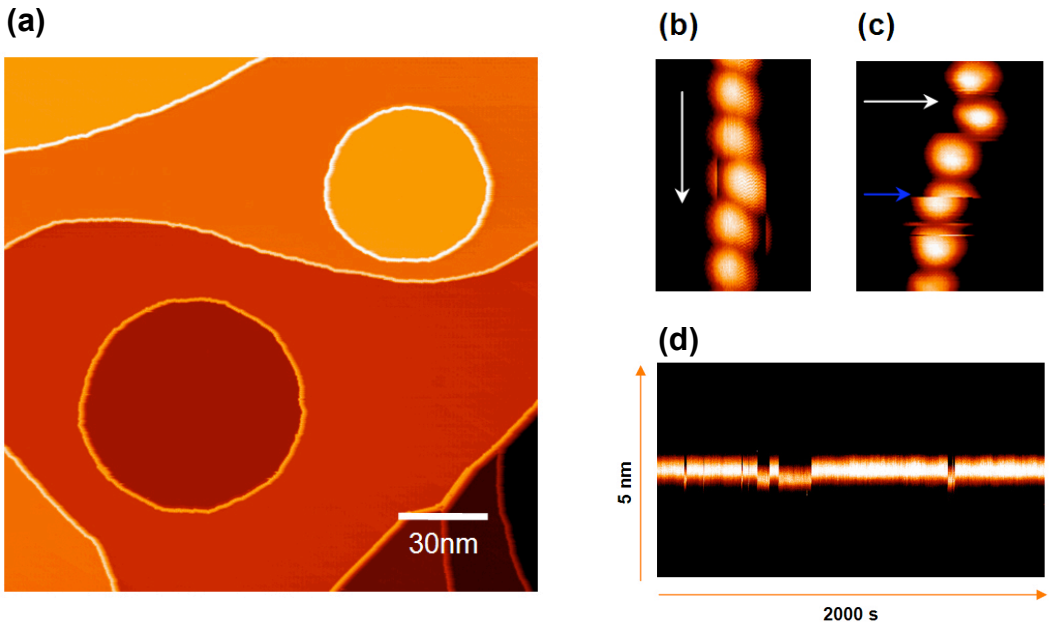

Figure 1 (a) STM topography images of Ag islands decorated by closed C_{60} chains. The tunneling conditions are U_{sample} = −1.71 V and I_t = 86 pA. **(b)** and **(c)** STM images showing C_{60} displacements between sequential scans. White arrows indicate scan direction. **(d)** temporal STM image of an individual C_{60} molecule in the C_{60} chains hopping. The STM tip repeatedly scans over the top of a single C_{60} molecule as noted by the blue arrow in **(c)**. The time intervals between observed hopping events are from 6.1 s to 170.8 s, and the displacement of the C_{60} molecule along the scan direction is 0.263 nm. The scan direction is 17 degrees from the close-packed direction of the substrate, and the lattice constant of Ag(111) is 0.2889 nm. Thus the C_{60} motion is consistent with a hop from a stable position to a nearest neighbouring stable position.

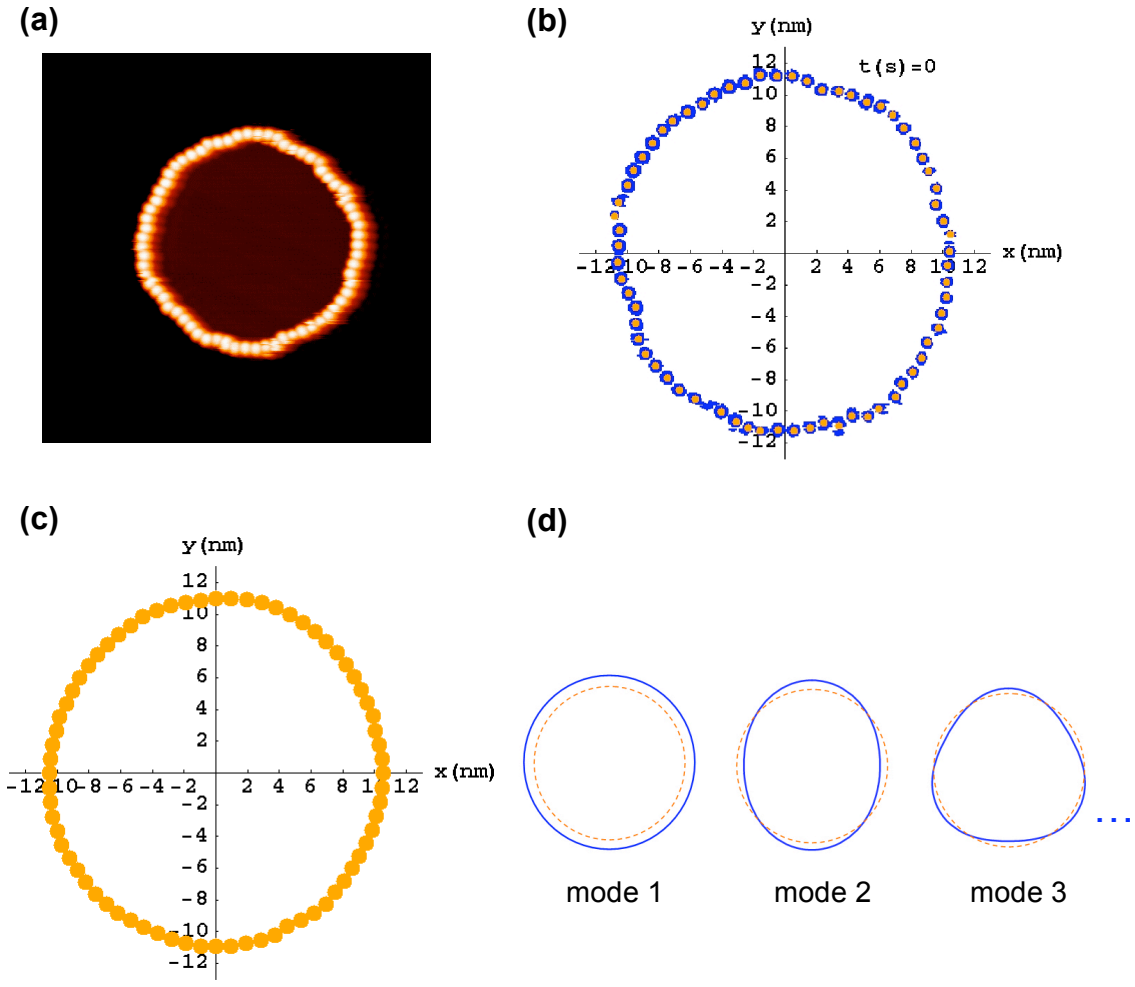

Figure 2 **(a)** STM topography of a C_{60} ring covering the Ag island edge, obtained from one frame of a set of 66 sequential images measured with time interval 52.4 s. **(b)** The large blue dots represent area of bright contrast due to C_{60} the STM topography image, and the orange dots are digitized positions of each C_{60}. See supplemental material for time-lapse movie (S3) showing fluctuations. **(c)** The mean shape of the C_{60} ring by averaging over 66 sequential topography STM images. **(d)** Schematic of circular fluctuation modes.

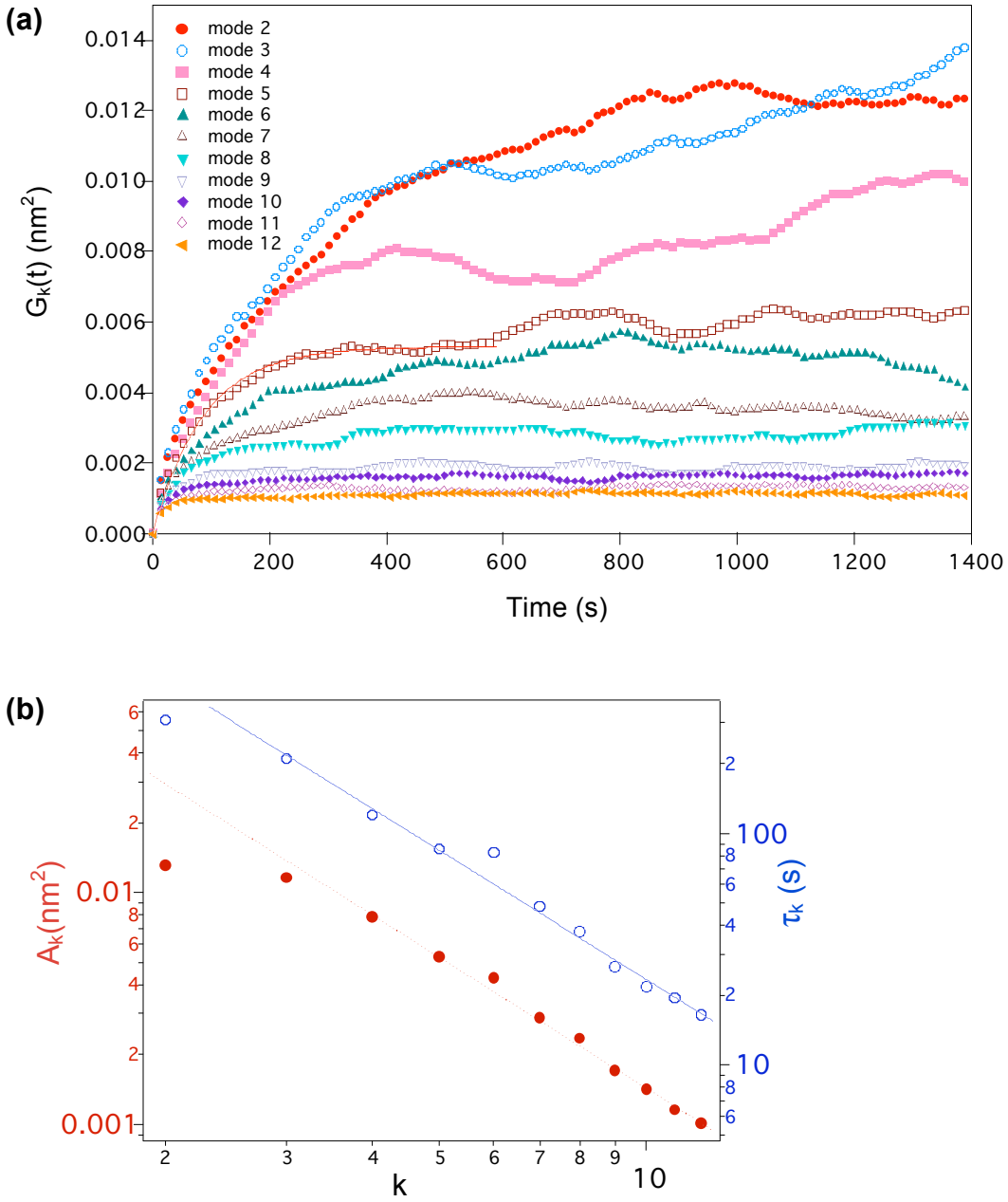

Figure 3 (a) Correlation function for different modes of the ring shape fluctuation. The solid red curve is the corresponding fit to Eq. 2 for mode 5. **(b)** A_k and τ_k vs. k. The dashed red line is the power law fitting for the experimental data, $A_k = A_0 \times k^{-\alpha}$. The best fit is $A_0 = 0.108 \pm 0.002$ nm^2, and $\alpha = 1.88 \pm 0.01$. The solid blue line is the power law

fitting for the experimental data, $\tau_k = \tau_0 \times k^{-z}$. The best fit is $\tau_0 = 1660.3 \pm 145$ s, and $z = 1.85 \pm 0.05$.

Supporting information

Detailed experimental procedures are described.

Large area scans (**Figure S1**) show the overall morphology of the surface following decoration by a C_{60} coverage controlled to create C_{60} chains one atom wide along step edges. From such large area images, specific features can be localized under the STM tip, and higher-resolution images can be made, as shown in enhanced color in **Figure S2**. **Figure S2** shows both decorated adatom islands and vacancies. Sequential scans of an entire closed ring, such as **Figure S2c**, are used to create movies (**S3**) of the structural fluctuations of the entire ring structure.

Supporting figures and movie

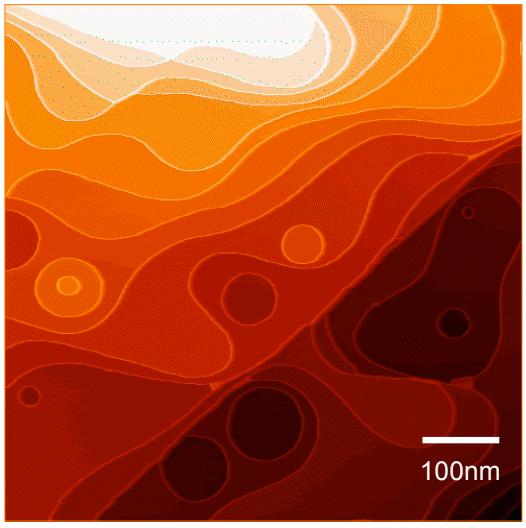

Figure S1 STM topography image of Ag thin film morphology decorated by single-molecule wide C_{60} chains. The tunneling conditions are $U_{sample} = -1.71$ V and $I_t = 86$ pA.

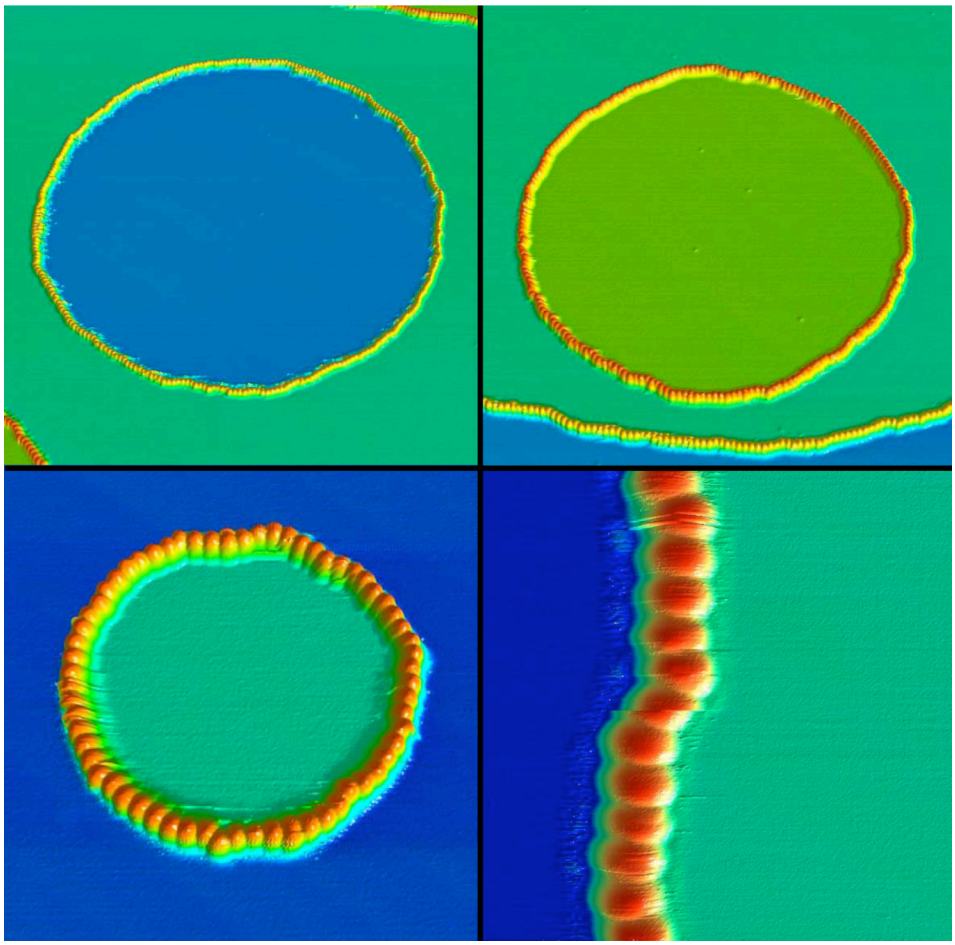

Figure S2 STM images (3D view) of different types and size scales of decorated islands. The color bar indicates height, which differs slightly in offset and scale for each image. **(a) (upper left)** large vacancy island decorated by a C_{60} ring (island diameter ~ 96 nm), **(b) (upper right)** large adatom island decorated by a C_{60} ring (island diameter ~ 72 nm), **(c) (lower left)** small adatom island decorated by a C_{60} ring (with 64 C_{60} molecules, diameter ~ 21 nm), **(d) (lower right)** close up view of an edge segment. The horizontal streaks and the "split" molecule near the center of the image indicate hopping of C_{60} molecules between sequential STM line scans.

Movie S3 A movie of a STM image ensemble including 66 sequential images with time interval 52.4 s. Images are as shown in **Fig. 2b**, in which the blue dots represent the STM topography image of C_{60} molecules, and the orange dots are the digitized C_{60} positions.

Chapter 5 Fluctuations in organic thin films

In this chapter we will discuss the self-assembled monolayers of C_{60} and acridine-9-carboxylic acid (ACA). We have found a chiral structure formed by these two components on Ag(111) due to C_{60} crystallizing the 2D gas phase of ACA molecules. The ordered/disordered (2D gas) phase boundaries also fluctuate at room temperature. We characterize thermodynamic properties of these boundaries.

5.1 Chiral structures formed by C_{60} and ACA

Introduction

The development of chiral surfaces offers new approaches to chiral synthesis and active devices. Chiral surfaces, produced by chiral molecular adsorption [157-162], electrodeposition [163], or slicing chiral single crystals [164-168], provide a platform for heterogeneous enantioselective reactions, with the advantage of easier product separation and reactivation. For device applications, chiral surfaces exhibit enantiospecific properties, such as electron-molecule interactions [169], polarization-dependent photoemission [170], and nonlinear optical response [157, 171]. The latter are especially interesting in the burgeoning field of organic optoelectronic and integrated photonic materials [172, 173]. Here we demonstrate how a mixture of C_{60} and ACA can be organized into chiral phases through a self-assembly process [174, 175], even

though the constituent molecules themselves are achiral. The hierarchical assembly mechanism suggests a broadly applicable route to chiral aromate surfaces, which are particularly desirable for potential optoelectronic applications.

Adsorption induced surface chirality has generally fallen into two classes: (1) The adsorption of chiral molecules on an achiral surface (direct-transfer chirality), and (2) The adsorption of molecules which are achiral in 3-D but become chiral when confined to the 2-D surface due to symmetry breaking imposed by the surface (surface-confined chirality). In the latter case, even though the individual adsorbed molecules become chiral, the surface phase often remains achiral due to the formation of a racemate (equal population of the two enantiomers). Only if molecule-molecule and molecule-substrate interactions favor an enantiopure phase will surface chirality result [176, 177]. By co-adsorption of C_{60} and ACA, we introduce a new method to generate surface chirality. In this method, the interactions among two achiral molecular species with very different symmetry and the substrate act to break the symmetry of the individual components. With its I_h symmetry classification, C_{60} appears a most unlikely candidate for chiral symmetry breaking. Nonetheless, when co-adsorbed with a C_{2v} symmetric ACA, interactions between C_{60} and ACA result in the assembly of a chiral phase. In this case, the C_{60} molecules form reactive complexes with ACA that nucleate into enantiopure domains with a specific chirality.

Experimental

Samples were prepared by sequential deposition of ACA (390 K) and C_{60} (650 K) on an epitaxially-ordered Ag(111) thin film grown on a mica substrate [178]. C_{60} was

deposited from an effusion cell in the UHV measurement system (base pressure $\sim 5\times10^{-11}$ torr) and ACA from a resistively heated Knudsen cell in a load-lock connected to the UHV chamber (base pressure $\sim 8\times10^{-9}$ torr). During the experiment, *ca*. 0.4 ML ACA and 0.4 ML C_{60} were deposited sequentially on the clean Ag(111) surface and imaged using an Omicron VT-STM in the same UHV chamber. All the STM images shown in this paper were taken at room temperature. Low temperature (40 K) STM studies (see supporting information) were used to provide additional information about specific molecular configurations as noted.

Results and discussions

The highly symmetrical C_{60} molecule is illustrated in Fig. 1a. Upon adsorption on metal surfaces, individual C_{60} molecules are mobile and have no preferential orientation unless cooled down to low temperature[155, 179]. An ordered phase of C_{60} forms even at low coverage, with a $2\sqrt{3}\times2\sqrt{3}R30°$ structure on Ag(111) [123]. Individual ACA molecules (Fig. 1b) also retain reflection symmetry and thus are achiral, when adsorbed on the surface as free molecules, given the expected symmetric occupancy of the hydrogen atom in the carboxyl group [180, 181]. At room temperature, ACA molecules form a 2-D gas phase on the surface when the coverage is low (< 0.3 ML). With increasing ACA coverage (> 0.3 ML), an ordered ACA structure appears, which can be indexed in matrix notation as (4 0, 2 4) with respect to the Ag(111) lattice (definition of Ag lattice vectors is shown in Figure. 4a). This ACA ordered phase is in dynamic equilibrium with the 2-D gas phase. In the ordered structure, hydrogen bonds between nitrogen atoms and hydroxyl hydrogen atoms link ACA molecules into parallel chains that extend over 100 nm to span

the widths of Ag(111) terraces [182]. In this structure, the molecular long axis is parallel to the low-symmetry $[11\bar{2}]$ direction of Ag(111). Because the symmetry of the carboxyl group is broken by the hydrogen bonding, individual molecules in this higher density phase are chiral. However, the ordered phase itself is achiral as the result of a racemic molecular arrangement.

The structures of the co-adsorbed ACA and C_{60} monolayers show a striking dependence on deposition sequence. If C_{60} molecules are deposited first, the C_{60} and ACA molecules form phase-separated domains identical to those of the single component monolayers described above [123, 182] (see supporting information). However, when the deposition sequence is reversed, four distinct structures are observed simultaneously, as shown in Fig. 1c. Three of the phases are identical to those of the pure C_{60} and ACA structures (labeled as I, II, and III in Fig. 1c, respectively). However, a new and striking structure is also observed, in which there appears to be one C_{60} per unit cell (labeled as IV in Fig. 1c). Two significant features of this new structure are noted. First, the distance between neighboring C_{60} molecules is 2.65 nm, in comparison with the 1 nm nearest neighbor spacing of C_{60} in the pure $2\sqrt{3}\times 2\sqrt{3}R30°$ -C_{60}/Ag(111) phase. Second, there are two domains of phase IV that demonstrate mirror symmetry with respect to the $[11\bar{2}]$ directions of Ag(111) as indicated in Fig. 1c. The structure is determined to be $2\sqrt{21}\times 2\sqrt{21}R\pm 10.9°$, or (10 2, -2 8) and (8 -2, 2 10) in matrix notation with respect to the Ag(111) surface.

STM images of this mixed phase reveal triangular domains, which are frequently arranged into a hexagonal “Chinese-Checkers” pattern (Fig. 2a). Higher resolution images (Fig. 2b) show that in addition to the dominant feature in each unit cell (identified

as the C_{60} molecule), there are additional rod-shaped features visible between the C_{60} molecules. These rod-shaped features are similar in size and shape to the appearance of individual ACA molecules, observed after cooling the 2-D ACA gas phase from room temperature to 40 K (see supporting information). With the help of C_{60} vacancies, the otherwise occluded ACA molecules are imaged directly. Their positions are highlighted with gray-shading in Fig. 2b, with the extrapolated ACA positions under the C_{60} molecules also demonstrated. The ACA molecules are arranged into two types of "molecular pinwheel" trimers, labeled as ***S*** and ***R*** in Fig. 2b, with different orientation with respect to the underlying Ag(111) lattice and with specific chiralities. In Fig. 2, each C_{60} molecule is located atop an ***R*** trimer and immediately bounded by three open ***S*** ACA pinwheels inside the domain. We define the domain where C_{60} sits atop an ***R*** trimer as ***S*** chirality (since the ***S*** trimer is exposed). Thus the domains presented in Fig. 2 have ***S*** chirality.

STM images of both enantiomeric phases, ***R*** and ***S***, are presented in Fig. 3 with a suggested molecular model. In Fig. 3b, C_{60} molecules always occupy the valley of ***S*** trimer and leave the ***R*** trimer empty, whereas in Fig. 3d reversed occupancy happens. As a result, the two phases in Fig. 3b and Fig. 3d are of ***R*** chirality and ***S*** chirality, respectively. These two phases demonstrate mirror symmetry with respect to the $[1\bar{1}0]$ direction of Ag(111).

Low temperature STM images indicate C_{60} molecules are positioned with opposing hexagonal rings parallel to the surface (see supporting information), consistent with the 3-fold symmetry of the underlying ACA structure. The ACA molecules in the underlying trimer are positioned without centro-symmetry with respect to the C_{60} to

accommodate the close spacing between molecules. This is the origin of the chiral symmetry breaking. Given this observed symmetry, the trimer ACA molecules are suggested to orient with the ring nitrogen atoms pointing inward and the carboxyl groups pointing outward, providing primary hydrogen bonds between carboxyl groups and secondary hydrogen bonds between ring nitrogen atoms and phenyl hydrogen atoms.

The resulting spatial array of the ACA molecules alone (e.g. without the C_{60} or the Ag substrate) is apparently described by the plane symmetry group P31M. However, due to the enantioselective C_{60} positioning, the symmetry group is lowered to P3, with symmetric operations of 120° rotation centered on the C_{60} molecules, the center points of the unoccupied trimers, as well as corners of the unit cells drawn in the figures. The enantiomerically pure phase can exist in two nonequivalent rotational domains: a rotation by 60° will give a non-superposable domain while a rotation by 120° will give a superposable domain. The walls between the homochiral domains are found to be straight and separated by distinct structures of the ACA molecules, as highlighted in Fig. 2. Following our molecular packing model, these domain boundaries are stabilized by H-bond formation between the ACA molecules at the edges of the adjacent domains (see supporting information). This provides further support for the proposed model and accounts for the commonly observed "Chinese Checkers" structures shown in Fig. 2a.

The model also allows a natural mechanism for the production of the two different enantiopure domains. As this intermixed phase only forms when C_{60} is deposited on ACA-preoccupied surface, it is plausible that C_{60} molecules first induce local ordering of an ACA trimer, with random selection of one of the trimer rotational orientations, which in turn is registered with respect to the underlying Ag(111) lattice. After the initial

chirality creation event, subsequent assembly of ACA molecules is constrained by the hydrogen bonding interactions to maintain the defined chirality. It is interesting to note that the subsequent C_{60} molecules never occupy the ACA trimer of opposite chirality inside one domain even though the spacing is large enough to avoid steric C_{60}-C_{60} repulsion. It is likely that the initial symmetry breaking event also induces configurational differences between the two ACA timers. The STM observations show that in the C_{60}-occupied trimers (both ***S*** and ***R*** chirality), the long axes of component ACA molecules are pointed along the $[11\bar{2}]$ directions of Ag(111), whereas for C_{60}-free trimers, the long axes of component ACA molecules are pointed along the $[1\,\bar{1}0]$ directions. The different interaction with the Ag(111) lattice may break the energy degeneracy of the trimers and make the latter energetically unfavorable for C_{60} occupation. Consequently, the ***S*** and ***R*** chiral phases show preferred domain orientations with respect to the substrate. The substrate thus plays a decisive role in setting the orientation of chiral domains.

Previous observations of surface chirality (class 1 and class 2 systems) have been restricted to the adsorption of single chiral or symmetry-breaking achiral molecules. In the present mixed-phase system, surface chirality is introduced by co-adsorption of the decidedly achiral C_{60}, which nucleates chirality by the enantioselective positioning over a racemic mixture of ACA molecules. For the intermixed ACA and C_{60} system, the resulting extended chirality is limited only by the finite domain size.

The chiral C_{60}-ACA phase provides a model for developing chiral aromate surfaces for technical applications. For these particular aromate components, the distance

between neighboring C_{60} molecules is 2.65 nm, dictated by the packing of ACA molecules. The possibility to shrink or expand this separation by the choice of aromate (e.g. isonicotinic acid or pentanoic acid) offers the intriguing possibility of tuning the lattice constant. Moreover, as C_{60} can be modified by the subsequent deposition of calixerene moieties [183], opportunity abounds to adjust the molecular landscape in the vicinity of the periodic chiral centers. Mixed phase systems thus offer a new strategy for generating chiral surfaces, that offers potential flexibility in tuning both the physical and electronic properties of the chiral structure, as will be needed for nanoarchitecture [184] and device applications [172, 185].

Supporting information available:

(1) STM image of separated phases when C_{60} was deposited before ACA, (2) low temperature high resolution STM image of C_{60} and ACA intermixed structure demonstrating 3-fold symmetry of C_{60}, (3) STM image showing the 2-d ACA gas phase following a temperature quench to 40 K, and (4) magnified STM image of juxtaposed ACA-C_{60} 60º rotational domains with the proposed molecular packing model, including molecular registration to the Ag lattice.

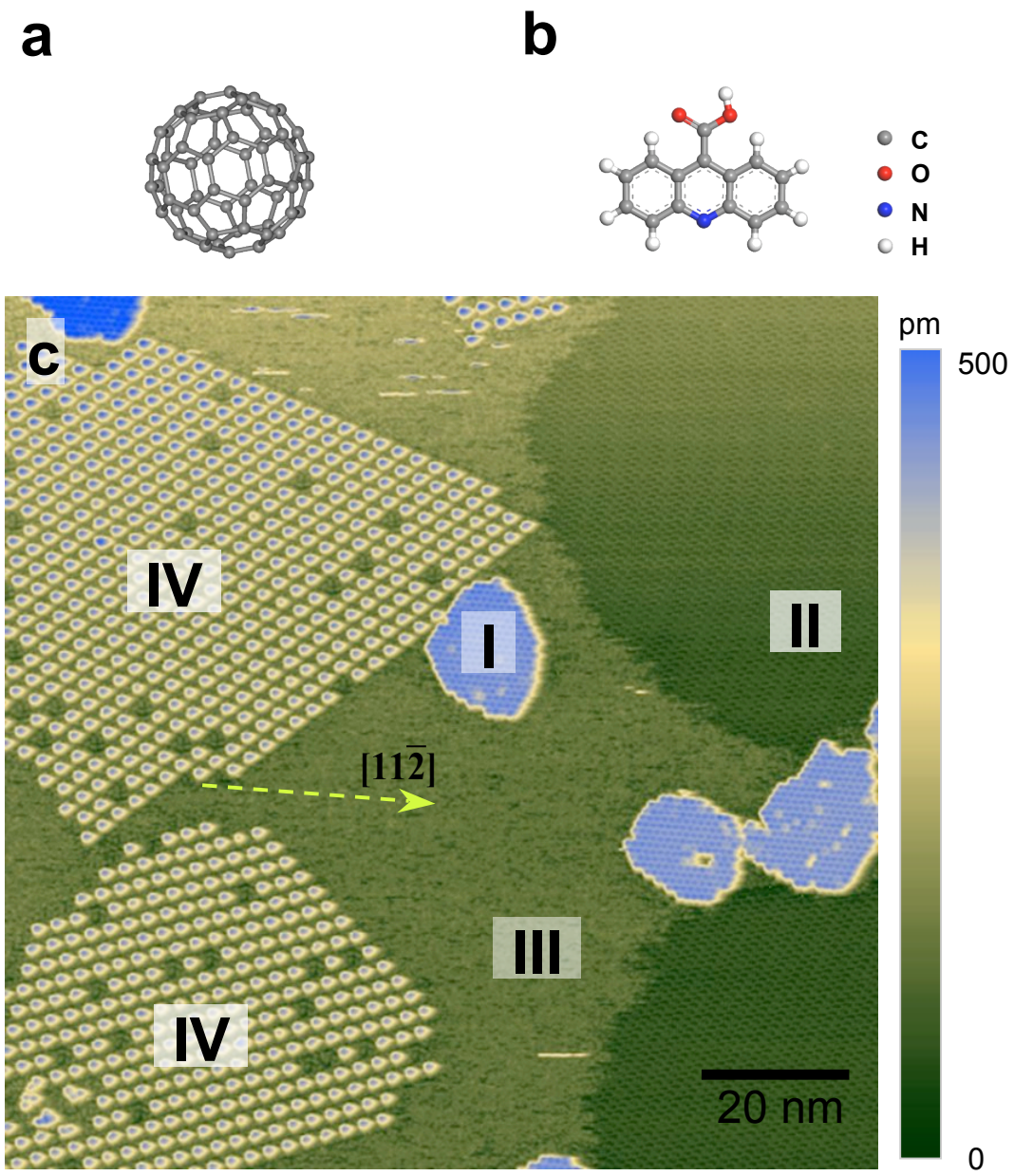

Figure 1. Self assembly of C_{60} and ACA supramolecular structures. a, b, Chemical structure of C_{60} (a) and ACA (b). c, STM image of distinct self organizing phases produced by sequential deposition of ACA (0.4 ML) and C_{60} (0.4 ML) on a room temperature Ag(111) substrate: Phase I, $2\sqrt{3}\times 2\sqrt{3}R30°$ -C_{60}/Ag(111); Phase II, (4 0, 2 4) -ACA/Ag(111); Phase III, 2-D ACA gas/Ag(111); and Phase IV, C_{60} and ACA

intermixed phase. Two domains of Phase IV are symmetric with respect to Ag $[11\bar{2}]$ direction. Constant current (40 pA) images were acquired with -0.8 V sample bias.

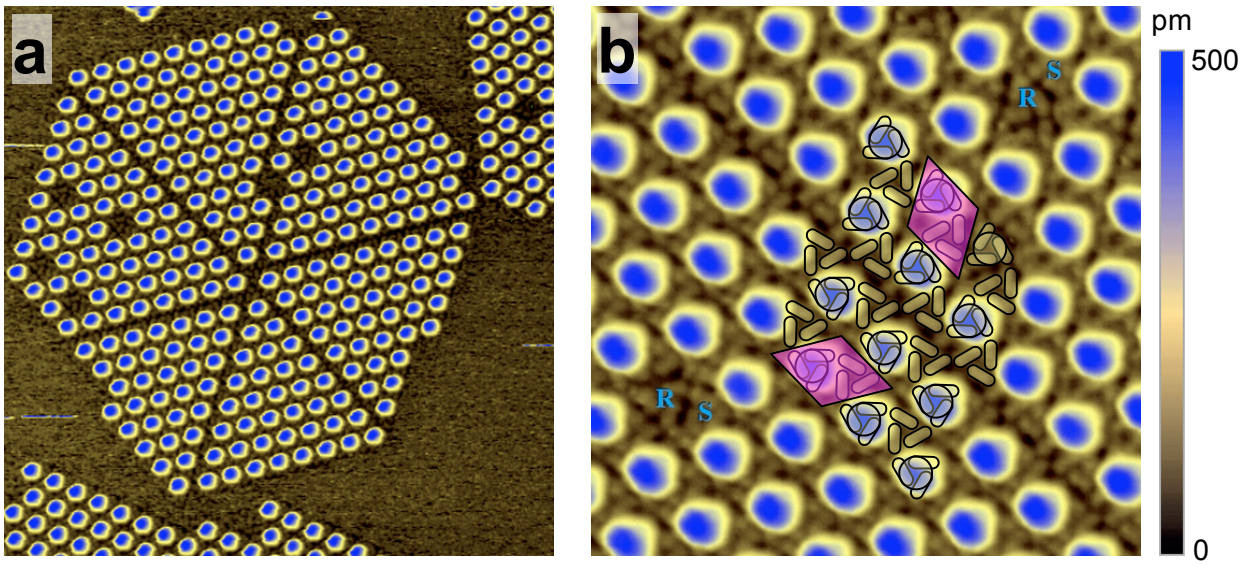

Figure 2. STM images of rotational domains with identical chirality of the intermixed C_{60} and ACA supramolecular phase. a, A hexagonal "Chinese-checkers" structure (size 60 nm x 60 nm, sample voltage -0.8 V, tunneling current 80 pA). b, A higher resolution image of the boundary between adjacent domains reveals additional features identified as ACA molecules (size 20 nm x 20 nm, sample voltage -0.8 V, tunneling current 40 pA).An outline drawing highlighting these molecular features is superposed on STM image and one unit cell is drawn for each of the domains showing the 60° rotation.

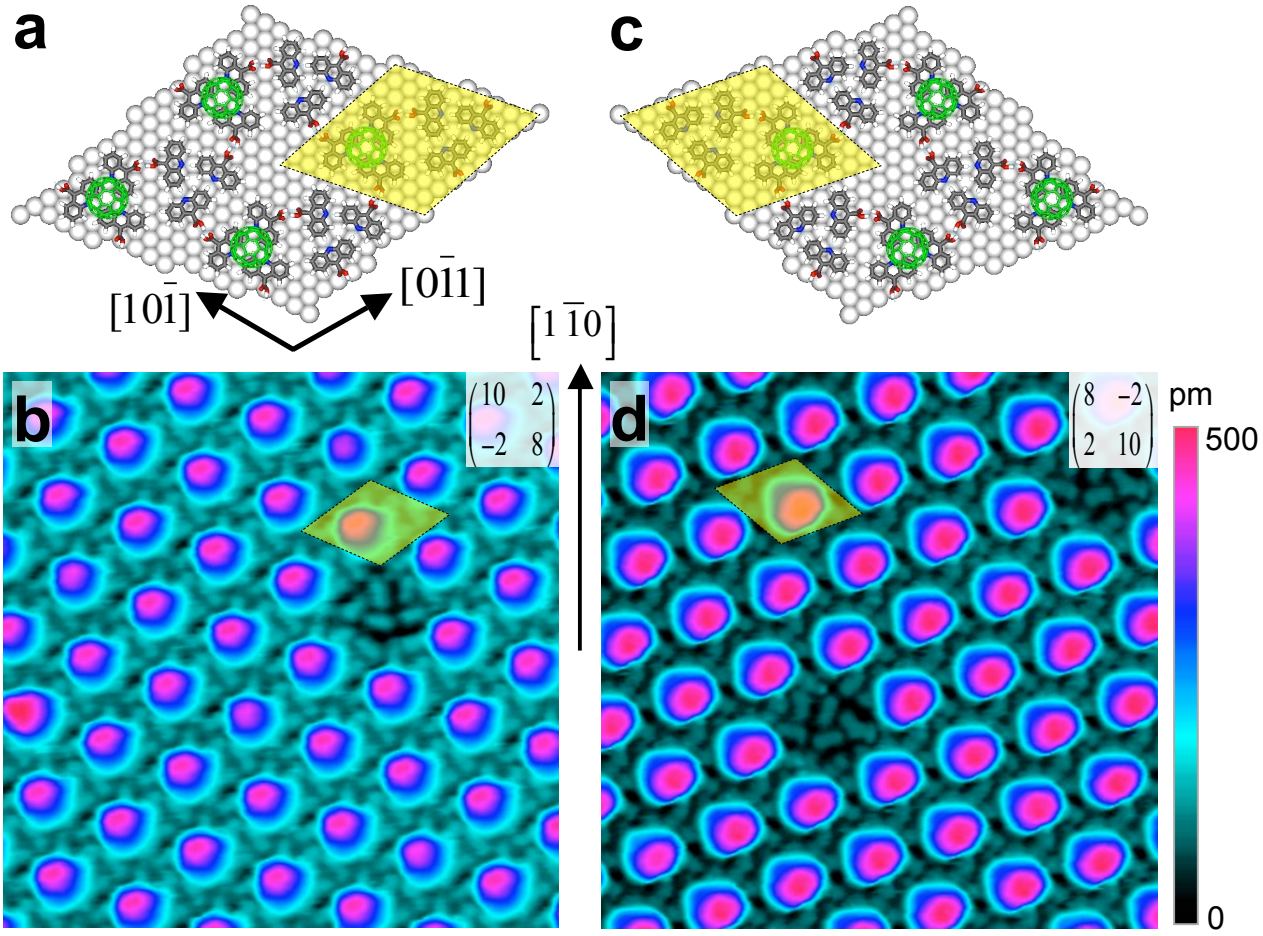

Figure 3. Proposed structural models and STM images of the C_{60} -ACA intermixed supramolecular structures for ***R*** chiral surface (*a*, *b*) and ***S*** chiral surface(*c*, *d*). For reference, a unit cell is indicated in each panel, along with the matrix notation of the domain. Ag(111) lattice vectors are shown in *a*. Constant current (40 pA) STM images (18 nm x 18 nm) were acquired with -0.8 V negative sample bias.

5.2 ACA boundary fluctuations

Introduction

Organic materials that allow electron and hole transport and recombination have extensive materials and device applications [186-190]. Understanding the relationships between the transport characteristics of organic thin films (OTF) and how molecules are structurally arranged within the film is a fundamental and challenging issue. For OTFs, the complex molecular symmetries and interactions [191-193] often cause the formation of multiple density-dependent phases, with pattern size on the nanometer or micron scale, coexisting at room temperature [177, 194, 195]. Previous research has mostly focused on the structural properties of each phase or the transport properties of the film as a whole [161, 196-198]. However, in fact, in many cases the boundaries of local ordered regions (often referred to as domain boundaries or island edges) dramatically affect the stability and transport properties of the OTFs. Herein we use time-dependent scanning tunneling microscopy (STM) to characterize fluctuations of such low-dimensional boundaries, using as a model system the boundary between the ordered and disordered phases of acridine-9-carboxylic acid (ACA) on Ag(111) at room temperature.

The ACA molecule, shown in Fig. 1a, has a roughly rectangular structure, with the potential for strong H-bonding intermolecular interactions along the C-axis, and weaker quadrupolar interactions along the Q axis. Our previous STM studies of ACA adsorption have shown that at low to moderate ACA coverage (< 0.3 ML), no ordered ACA structures form on the terraces of the substrate [199-201]. As ACA coverage is

increased, ordered structures begin to form, covering the substrate partially. Usually these islands of order extend from both sides of Ag monatomic steps of the substrate. The area around the islands shows no order at room temperature, but noise in the tunneling current suggests the presence of mobile species. This is confirmed by measurements at low temperature where the motion is quenched [199]. Thus above 0.3 ML, the ACA exists in two-phase equilibrium between an ordered and disordered phase. Careful STM imaging has revealed the molecular arrangement in the ordered phases [200, 201]. At moderate ACA surface densities, ACA molecules arrange head-to-tail into chains connected by OH…N hydrogen bonds (H bonds), along the $[1\bar{1}0]$ direction of the substrate, as shown in Fig. 1. According to this packing model, the molecular dimensions are ~ $2a$ in $[1\bar{1}0]$ direction and ~ $2\sqrt{3}\,a$ in $[11\bar{2}]$ direction as shown in Fig. 1b (a is the lattice constant of Ag(111)). The asymmetry of this structure provides two distinct types of edge boundaries (parallel and perpendicular to the hydrogen-bonded rows), for the measurements presented in this report.

Experimental methods

The substrates, Ag thin films on mica, are made by thermal deposition, as described previously [32, 86, 87], and transferred into a UHV chamber (base pressure ~ 3×10^{-11} torr). After several sputtering and annealing cycles, atomically clean Ag(111) surfaces are obtained, as confirmed by both LEED and STM. By carefully controlling annealing conditions, large defect-free terraces (> 1 μm) form on the Ag films.

Methods for the preparation of well-controlled ACA films have been determined previously [199-201]. In a preparation chamber (base pressure ~ 5×10^{-9} torr) contiguous

to the main UHV chamber, ACA in powder form is placed in a quartz Knudsen cell. After fully degassing the chamber at ~ 380 K, ACA molecules are thermally deposited at 393 K onto the Ag substrates, which are held at room temperature. The deposition rate is ~ 0.3 ML/min, calibrated by a quartz microbalance and subsequent STM measurement. When the ACA coverage is larger than 0.3 ML, ACA molecules coexist in ordered and disordered phases.

STM imaging was performed using professional standards as demonstrated in earlier work [43, 199, 202-205]. The tunneling current is ~ 40 pA at sample bias ~ 0.90 V. These mild tunneling conditions were carefully determined to assure that the tip-sample interactions do not affect the measurements, as will be demonstrated in the following section. To observe boundary fluctuations, we use repeated STM scans across a fixed position at the boundary, along the direction approximately perpendicular to the boundary direction. The time interval between sequential scans is 51.2 ms and the total measurement time is 102.4 s with 2000 lines for each temporal pseudoimage. Images are recorded in both the forward and backward scanning directions, and analyzed separately. Typically 15 such forward/backward data sets are measured for each boundary investigated. To extract the position of the boundary as a function of time $x(t)$, we flatten the temporal pseudo-images by tilting the images to level one of the phase regions, and then identify the boundary at which the height is midway between the two phases. One $x(t)$ data set is obtained from each pseudo-image.

Results

Images of ordered regions formed at an average ACA coverage of ~ 0.6 ML are shown in Fig. 2. The isolated ordered ACA islands were formed on wide terraces (e.g. far from step edges that nucleate the ordered phase). Such isolated islands are typically close to square, with an aspect ratio of the island width along the $[1\bar{1}0]$ direction of the substrate to the width along the $[11\bar{2}]$ direction near to one.

The edges of ACA ordered islands, *i.e.* the boundaries between the ordered phase and the disordered phase, appear frizzy [206], clearly indicating thermal fluctuations at room temperature as shown in Fig. 3. The boundary is roughly perpendicular to the $[1\bar{1}0]$ direction of the substrate. Considering the molecular arrangement in the ordered phase (see Fig. 1), these boundaries are formed by ends of the ACA chains in the ordered phase, so they will be noted as **CE** (represents "chain-end", see Fig. 1) boundaries. The inset shows a boundary roughly perpendicular to the $[11\bar{2}]$ direction, which will be noted as **S** (represents "side") boundaries. For temporal imaging, the STM scan direction is along the direction perpendicular to the boundary orientation, as indicated by white arrows in Fig. 3b. The temporal pseudo-images formed as the STM tip repeatedly scans over a point at the boundary are shown in Figs. 4a and 4b. The vertical axis is time t and the horizontal axis is the position of the point $x(t)$.

The distribution of displacements for one boundary analysis (average over 14 temporal pseudoimages) for **S** boundaries is shown in Fig. 5. The boundary displacements have a Gaussian distribution as required for fluctuations in thermal equilibrium. The boundary width w can be obtained by fitting as shown Fig. 5. From three independent boundary analysis, the average boundary width is 2.04 ± 0.04 nm for **CE** boundaries. For **S** boundaries, the average w = 2.01 ± 0.08 nm by four independent

boundary analysis. The data used to create the distribution shown in Fig. 4, by line scanning along the one scan direction shown in Fig. 3. When data from the opposite scan direction were also analyzed, the results were identical, providing strong confirmation that under the chosen tunneling conditions, the STM scans are not perturbing the thermal distribution at the boundaries.

Given the displacements, *x(t)*, it is straightforward to calculate the time correlation functions *G(t)* and autocorrelation function *C(t)* respectively [37]:

$$G(t) = \langle (x(t+t_0) - x(t_0))^2 \rangle , \quad (1)$$

$$C(t) = \langle (x(t+t_0) - \bar{x})(x(t_0) - \bar{x}) \rangle , \quad (2)$$

Each individual *x(t)* data set is used to calculated individual *G(t)* and *C(t)*. Fig. 6 and Fig. 7 present typical *G(t)* and *C(t)*, which are averages of the correlation functions for more than 10 data sets.

The continuum step model is used to relate the correlation functions to the physical properties of boundary. [11, 66, 69] The results show that the time correlation function can be fitted by the following formula:

$$G(t) = \langle (x(t+t_0) - x(t_0))^2 \rangle = G_0 t^{\frac{1}{n}}, \quad (4)$$

$$G_0 = \left(\frac{2\Gamma(1-\frac{1}{n})}{\pi}\right)\left(\frac{k_B T}{\tilde{\beta}}\right)^{\frac{n-1}{n}} \Gamma_a^{\frac{1}{n}}, \quad (5)$$

where Γ_a is the mobility of the boundary, k_B the Bolzmann constant, Γ the gamma function and $\tilde{\beta}$ the step stiffness. The exponent $n = 2$ when the boundary fluctuations are determined by atomic attachment/detachment in exchange with the disordered phase [12, 36, 207], and $n = 4$ for boundary fluctuations dominated by atom diffusing along the

boundaries [66, 206, 208, 209]. By fitting the time correlation function, shown as the solid red curve in Fig. 6, we find that the exponent $1/n = 0.52 \pm 0.07$. For consistency checking, we average 3 independent measurements for **CE** boundaries, and 4 independent measurements for **S** boundaries. The average value $1/n = 0.516$ for the **CE** boundary and 0.512 for the **S** boundary. This shows that the boundary fluctuations are dominated by uncorrelated events, with the most obvious mechanism being molecular attachment/detachment for both boundaries. Furthermore, $G_0 = 3.76$ nm^2 for **CE** boundaries and 3.70 nm^2 for **S** boundaries. Using Eq. (5), we can roughly calculate: $k_B T \Gamma_a / \tilde{\beta} \approx 11.1$ nm^{4}s^{-1} for **CE** boundaries and 10.8 nm^{4}s^{-1} for **S** boundaries. The significance of these values will be discussed below.

Once we determine that the boundary fluctuations are predominately due to molecular attachment/detachment, we can further analyze the autocorrelation functions as shown in Fig. 7. For the attachment/detachment case, the autocorrelation functions have time dependence:

$$C(t) = C(0)((e^{-t/\tau_c}) - \Gamma(\frac{1}{2}, \frac{t}{\tau_c})(\frac{t}{\tau_c})^{1/2}), \quad (6)$$

$$\tau_c = (\frac{L}{2\pi})^2 \frac{k_B T}{\Gamma_a \tilde{\beta}}, \quad (7)$$

where L is the correlation length (or system size), and τ_c is the correlation time. The fitting curve is shown as the solid red curve in Fig. 7. By fitting C(t), the values for $C(0)$ and τ_c can be extracted. The average value of $C(0)$ is 2.74 nm^2 for **CE** boundaries and 2.42 nm^2 for **S** boundaries. From the Langevin analysis, we know $C(0)$ is proportional to w^2. For comparison, here we calculate $C(0)_{CE}/C(0)_s = 1.13$, and $w^2{}_{CE}/w^2{}_s = 1.03$. These two ratios are in reasonable consistence with each other. The average time constant is $\tau_c =$

3.59 s for **CE** boundaries and 2.73 s for **S** boundaries. Typically the island boundaries we measured had side length from 50 nm to 70 nm. For estimating the values of Γ_a and $\tilde{\beta}$, we use 60 nm as the value of the system size L. Using this value of L in Eq. (7), we can calculate $k_BT/\Gamma_a\tilde{\beta}$ = 0.039 nm^{-2}s for **CE** boundaries and 0.030 nm^{-2}s for **S** boundaries. Combining these values with the values of $k_BT\Gamma_a/\tilde{\beta}$ obtained from the values of G_0 above, we obtain, for **CE** boundaries, edge stiffness $\tilde{\beta}$ = 39.1 meV/nm and edge mobility Γ_a = 16.8 nm^3/s; and for **S** boundaries, $\tilde{\beta}$ = 45.5 meV/nm and Γ_a = 19.0 nm^3/s. (For comparison, using the formula $w^2 = \frac{k_BTL}{12\bar{\beta}}$, with the average w from the Gaussian fitting as shown in Fig. 5, yields $\tilde{\beta}$ = 31.1 meV/nm for **CE** boundary; 32.0 meV/nm for **S** boundary.

Table 1: Synopsis of values (1/n, w, G_o and τ_c) directly determined from the distribution and correlation functions, and the derived values ($\tilde{\beta}$, Γ_a, τ_a) obtained assuming L = 60 nm. All values correspond to T = 300 K.

	CE-boundary (parallel to $[11\bar{2}]$)	S-boundary (parallel to $[1\bar{1}0]$)
1/n	0.516	0.512
W (nm)	2.04 ± 0.04	2.01 ± 0.08
G_o (nm^{2}s$^{-1/2}$)	3.76 ± 0.25	3.70 ± 0.72

τ_c (s)	3.59	2.73
L (average) (nm)	60	60
$a_{//}$ (nm)	1.0008	0.5778
$a_{\perp}$ (nm)	0.5778	1.0008
$\tilde{\beta}$ (meV/nm)	39.1	45.5
(from w^2)	31.1	32.0
Γ_a (nm^3/s)	16.8	19.0
τ_a (s)	0.03	0.02

Also, given the values for the edge mobilities, Γ_a , the average time between molecular attachments/detachment events τ_a can be expressed as [66]:

$$\Gamma_a = \frac{a_{//}^2 a_{\perp}}{\tau_a}, \qquad (8)$$

where $a_{//}$ is the molecular dimension along the boundary direction and $a_{\perp}$ is the molecular dimension perpendicular to the boundary direction. This yields $\tau_a \approx 0.03$ s for **E** boundaries and 0.02 s for **S** boundaries. Using a simple estimate of the attachment rate as $1/\tau_a = \nu \exp(-E_a/k_B T)$, with the frequency factor ν set to 10^{13}/s, yields estimates of the activation energies of 0.67 and 0.68 eV, suggesting strong bond ruptures are needed to reconfigure the boundary edge.

From STM topography images, we can precisely determine the period of ACA molecules in the ordered phase, intermolecular structures, and further build the packing model as we did in our previous work [200], but for the disordered phase, STM is "blind". Fortunately the values of τ_a provide some information about ACA molecules near the phase boundary in the disordered phase. As discussed above, the H bonds do not contribute much to the boundary fluctuations, so the average time between attachments/detachments are closely related to the diffusion rate of ACA molecules on Ag(111). In the ordered phase, ACA molecules are roughly arranged with their long axes along the $[11\bar{2}]$ direction and their short axes along the $[1\bar{1}0]$ direction. In order to attach to **CE** boundaries, ACA molecules need a few final steps along their short axes; but for **S** boundaries, these final steps are along their long axes. Obviously, moving is much easier for the latter than the former. This is likely the reason why the value of τ_a for **CE** boundaries larger than the corresponding value for **S** boundaries.

Theoretical results and discussion

In the ordered phase, ACA molecules connect to each other by strong H bonds along the chains, while between neighboring chains, the interaction should be a quadrupole interaction weaker by a factor of four to six [210]. The asymmetry of the chain bonding in the ordered phase, shown in Fig. 1, would naturally suggest that there should be a substantial difference in the behavior of the two types (**S** and **CE**) of edge boundaries. Thus the similarity of the thermodynamic and kinetic values for the **S** and **CE** steps determined from the experimental results are initially quite surprising, and requires a very interesting physical interpretation, as we now argue. We will use lattice gas models [191,

211] to illustrate the main consequences of the bonding asymmetry, and to understand how the effects of the molecular conformational changes on the substrate interaction can dramatically modify the mesoscopic effects of the asymmetry in the intermolecular interactions.

Considering first the simplest one-component picture where each site on a square lattice is either vacant or occupied by a single ACA molecule, chain-like structures will be favored by anisotropic nearest neighbor interactions in which two adjacent molecules in the chain direction (along the **CE** axis, arbitrarily chosen in the vertical direction in Fig. 1a)) have a large favorable energy $-\varepsilon_{CE}$, while neighbors in the opposite (side) alignment have a higher energy $-\varepsilon_s$, with $\varepsilon_{CE} >> \varepsilon_s$. (In this one-component version of the lattice gas model, which maps onto the usual spin ½ Ising model with anisotropic ferromagnetic coupling between nearest neighbor spins, [209, 212] ACA-substrate interactions can be adsorbed into the chemical potential and play no direct role)

This lattice model yields results that match the intuitive expectations for the asymmetry of the island shapes and step stiffness. End boundaries break strong chain bonds and have a high energy relative to side boundaries, resulting in anisotropic island shapes. The aspect ratio of the island [96, 213-215] is determined by the edge formation free-energies of an island, which are β_{CE} and β_S for edges perpendicular to the **CE** and **S** axes respectively in Fig. 1. While more detailed expressions are available, at temperatures away from the critical temperature the island shape is reasonably approximated by using T = 0 values, thus yielding a rectangular shape with a ratio of lengths given by $L_{ce}/ L_s = \varepsilon_s / \varepsilon_{ce}$. But removal of a molecule from a straight end boundary breaks only weak ε_s bonds, while it breaks ε_{ce} bonds along the side boundary.

Thus boundary fluctuations at finite temperatures are also anisotropic, with larger fluctuations at the end boundary. Moreover this version of the lattice gas model has a large gas density only very near the critical temperature. All these discrepancies with experiment highlight the need for a more realistic model.

We can accomplish this while still staying within a simple lattice gas framework by noting as in Fig. 1 that the strong chain H-bonds require very different and specific head-to-tail orientations of adjacent ACA molecules. We can treat these different orientations as different species of a multicomponent lattice gas, where sites are either vacant or singly occupied by tilted molecular components U ("up") or D ("down"). Now we assume that strong H-bonds form with energy $-\varepsilon^c_{UD}$ only if a U is next to a D in the chain direction. In the side direction, the quadrupolar interactions $-\varepsilon^s_{UD}$, $-\varepsilon^s_{UU}$ and $-\varepsilon^s_{DD}$ are much less favorable. Experimentally (see Fig. 1b), the lateral ordering of the chains provides evidence that the symmetrical side interactions ($-\varepsilon^s_{UU}$ and $-\varepsilon^s_{DD}$) are somewhat more favorable than the unsymmetrical $-\varepsilon^s_{UD}$.

The different molecular conformations (tilted orientations) will have different interaction energies with the substrate. Let us assume that U has a more favorable interaction $-\varepsilon_U$ with the substrate than does D, with energy $-\varepsilon_D$. Then adjacent bonding U-D molecules along the chain direction will gain the favorable intermolecular energy ($\varepsilon^c_{UD} - \varepsilon_{UU}$) relative to a U-U configuration, but at the cost of a higher substrate energy $\varepsilon_D - \varepsilon_U$. This three-component lattice gas model maps onto a generalized version of the Blume, Emery, Griffiths or spin 1 Ising model. There have been many studies of this system in other contexts, though not with parameters expressing the competition between bonding (intermolecular) and substrate (single particle field) terms needed here.

An even better physical description of both the chain and gas phases is achieved by introducing another component G, which represents the dominant species in the gas phase. An isolated G molecule has an optimal (presumably planar) orientation with respect to the substrate, and produces an even lower substrate interaction energy $-\varepsilon_G$, than would either a U or D orientation. The substrate interaction energy ε_G physically could include some relaxation energy of the substrate around an isolated G molecule, some of which could be lost for two adjacent G molecules [211]. This can be accounted for within a lattice gas framework by using a constant ε_G along with an effective intermolecular interaction between a GG pair, $-\varepsilon_{GG}$, that is slightly less favorable than that of a UU or DD pair. Parameter values will be chosen so that the dominant configurations in the solid phase are UD chains ordered in the side direction, but all components can in principle be present in any phase or configuration.

Fig. 8 gives a schematic description of the model. The interaction between adjacent up and down components in the chain direction is the hydrogen bonding energy. Values for the various interaction parameters can be chosen so the following conditions are all satisfied. a) The solid phase consists predominately of an ordered array of UD molecules in the chain direction. Adjacent chains arrange so that lateral rows of UU and DD neighbors are seen. b) The gas phase has a relatively high density with mostly isolated G molecules c) The T=0 boundary energies per unit length along a straight side or end boundary are essentially the same, consistent with roughly square island shapes and similar fluctuations of the side and end boundaries. See Table ? for the values we chose.

We used Monte Carlo simulations to determine properties of this system at finite temperatures corresponding to those of the experiments. In our Monte Carlo simulation [216], we used a 2 dimensional 200×200 lattice. On each site, the state can be up particle U (purple), down particle D (blue), Gas particle G (orange) or vacancy. Each step, we randomly choose 40000 sites, and each site can select its state by calculating all the possible state energies E_i. E_i is determined by the site state itself and all the interactions with the substrate and its 4 neighbors and the possibility to be in state i is determined by $P_i = C \cdot \exp(-E_i / k_B T)$.

Fig. 9 shows an equilibrated Monte Carlo configuration of the lattice gas model where a solid, mainly UD chain island, with both side and end boundaries visible is in equilibrium with a dense vapor of mostly isolated G molecules. The essential feature in getting such configurations is the proper balance between the favorable UD chain intermolecular interaction and U and G substrate interaction and the unfavorable D substrate interaction.

The overall Hamiltonian for the new set of interactions is:

$$H = N_U \varepsilon_U + N_D \varepsilon_D + N_{UD} \varepsilon_{UD} + (N_{UU} + N_{DD}) \varepsilon_{UU} + N_G \varepsilon_G + N_{GG} \varepsilon_{GG} \qquad (11)$$

where the number of molecules with the "up" and "down" tilt configurations are N_U and N_D, with corresponding substrate interactions energies are ε_U and ε_D. The interaction between an up and a down configuration is the hydrogen bonding energy, and is represented as the third term in Eq. 11. The lateral (quadrupole) interactions between chains of molecules is assumed to be the same for up-up and down-down pairs, and is represented in the fourth term of Eq. 11. The contribution of the chemical potential of adsorption, e.g. the free energy cost for adding a molecule to the system as a whole is

given by the last term. The new set of interaction energies allows an immediate insight into the experimental results. Within the model of Fig. 8, the T=0 step energies will be

$$\beta_E = \left(\varepsilon_{UD} + \varepsilon_U\right)/(a_E) \qquad \text{Eq. 12a}$$

$$\beta_S = \left(2\varepsilon_{UU} + \varepsilon_U + \varepsilon_D\right)/a_S \qquad \text{Eq. 12b}$$

where we have defined the "up" configuration as energetically favorable, and a_E and a_S are the unit lengths along the E and S boundary edges respectively.

Conclusion

In summary, this is the first time that time-dependent STM has been used to characterize the boundary properties of phase boundaries in self-assembled monolayers. The boundaries between the ordered and disordered ACA phases on Ag(111) are governed by molecular attachment/detachment diffusion. The values of the boundary stiffness are 39.1 meV/nm for **CE** boundaries and 45.5 meV/nm for **S** boundaries. The values of the boundary mobility are 16.8 nm^3/s and 19.0 nm^3/s, respectively. The corresponding attachments/detachment rate is also extracted, with value 0.03 s for **E** boundaries and 0.02 s for **S** boundaries. In the future, variable temperature measurements can be used to further determine the H bond energy and the molecule-substrate interaction.

Figures

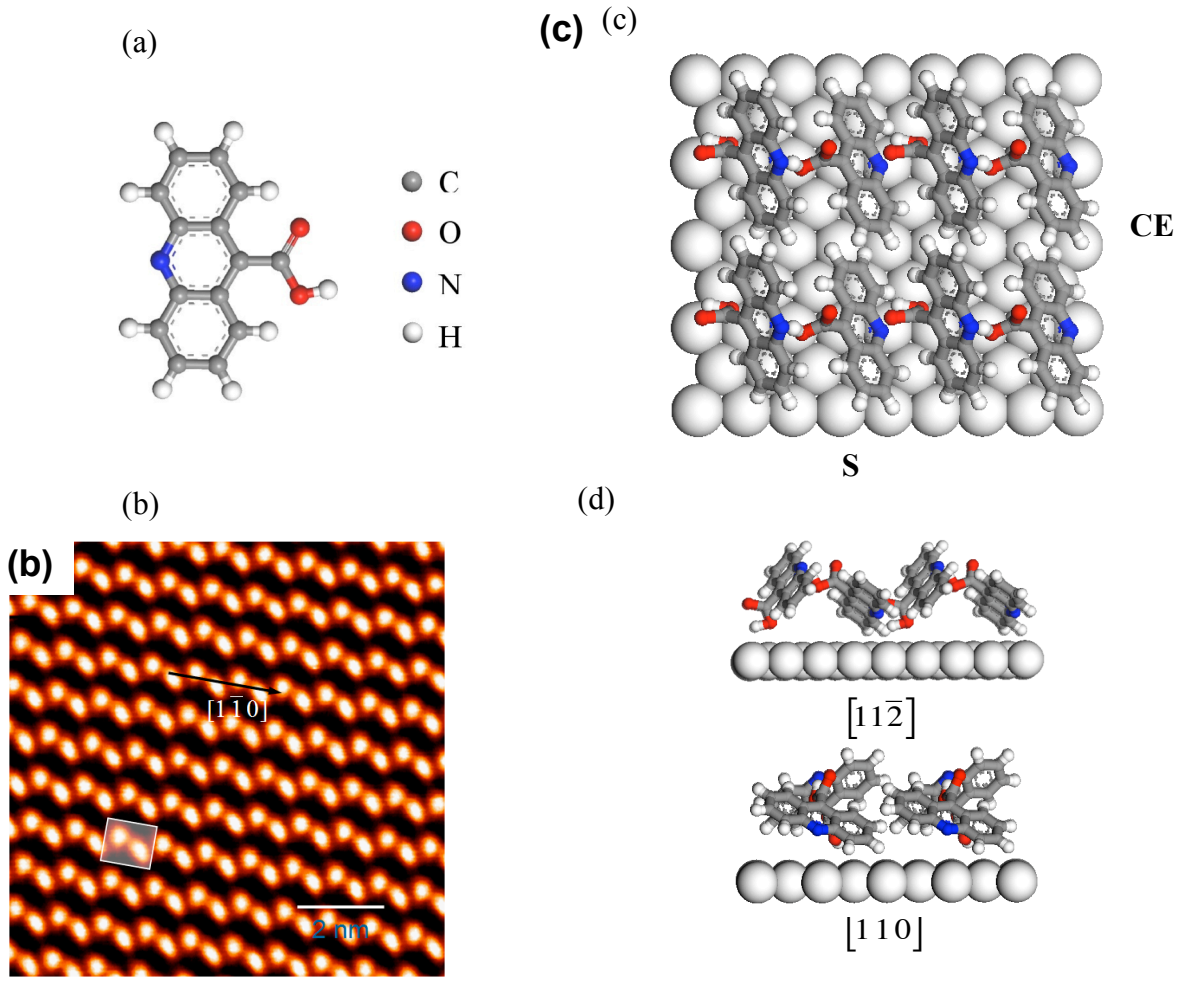

Fig. 1 (Color online) a) Molecular structure of ACA, with two in-plane symmetry axes indicated, in the ordered phase, arrangement of ACA molecules (b) as measured using STM and c) corresponding molecular model. d) Alternating ACA molecules along the hydrogen-bonded chains are tilted with respect to the substrate. Two side views along the S side and CE side respectively.

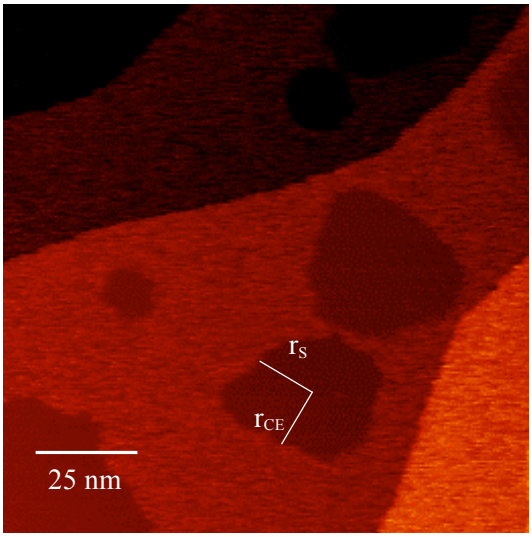

Fig. 2 STM images of ordered islands and sounding disordered phases. r_{CE} and r_S indicate the distance from center to edges, with aspect ratio r_{CE}/r_S close to 1.

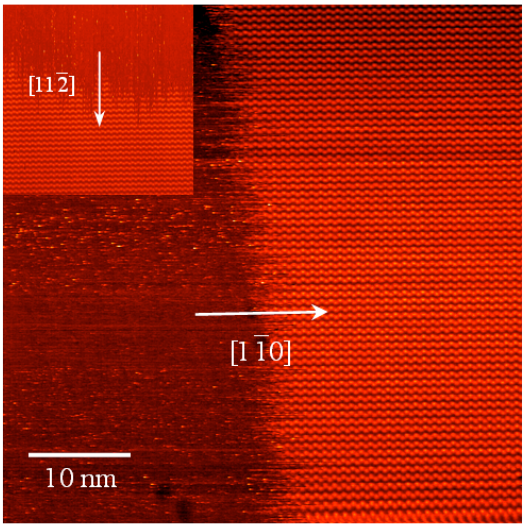

Fig. 3 (color online). STM images of boundaries of ordered and disordered phases. The white arrow indicates the scan directions for the fluctuation measurements. The boundary is perpendicular to the $[1\,\bar{1}0]$ direction and the scan direction is along $[1\,\bar{1}0]$ direction (**CE** boundary); (inset) boundary perpendicular to $[11\bar{2}]$ direction with the scan direction is along the $[11\bar{2}]$ direction (**S** boundary).

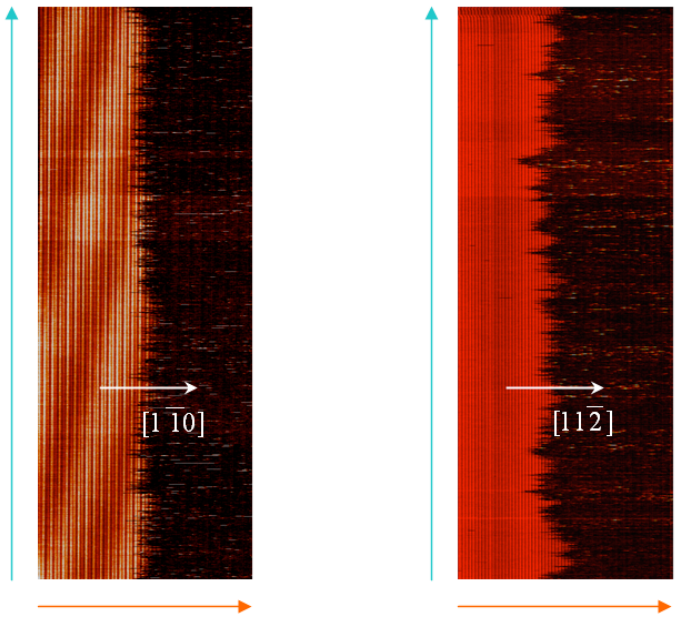

Fig. 4 (color online). Pseudo-images of boundary fluctuations. For both pseudo-images, the line scan size is 50 nm, the line scan time is 51.2 ms, and the total measurement time 102.4 s with 2000 lines. (a) boundary perpendicular to the [1 $\bar{1}$ 0] direction with the scan direction along the [1 $\bar{1}$ 0] direction (**CE** boundary); (b) boundary perpendicular to the [11$\bar{2}$] direction with the scan direction along the [11$\bar{2}$] direction (**S** boundary).

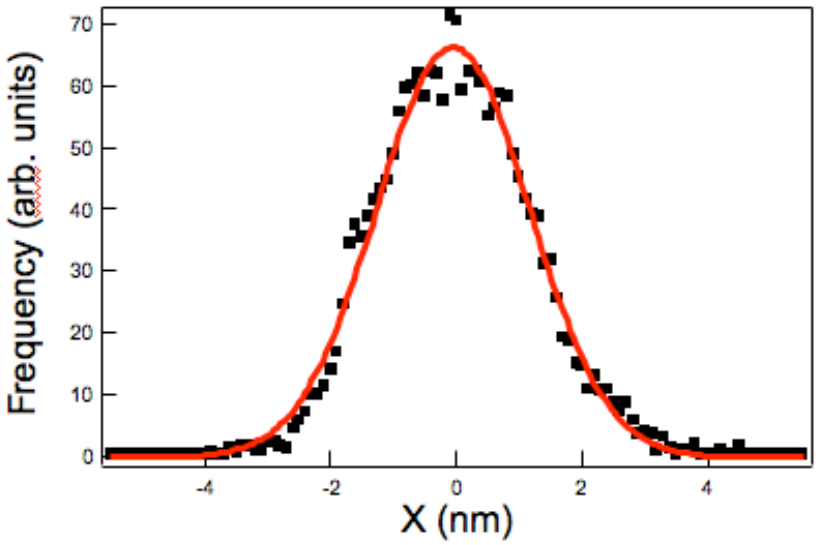

Fig. 5 (color online). Distribution of boundary displacement x(t). The red solid line is the Gaussian fit for the experimental data, $y_0 + A \times e^{-(\frac{x-x_0}{w})^2}$, with best fitting parameters, y_0 = -0.25 ± 0.38, A = 67 ± 1, x_0 = – 0.06 ± 0.01 nm and w = 1.72 ± 0.02 nm. The average position of the step edge for each data set, x-bar, was subtracted prior to forming the distribution.

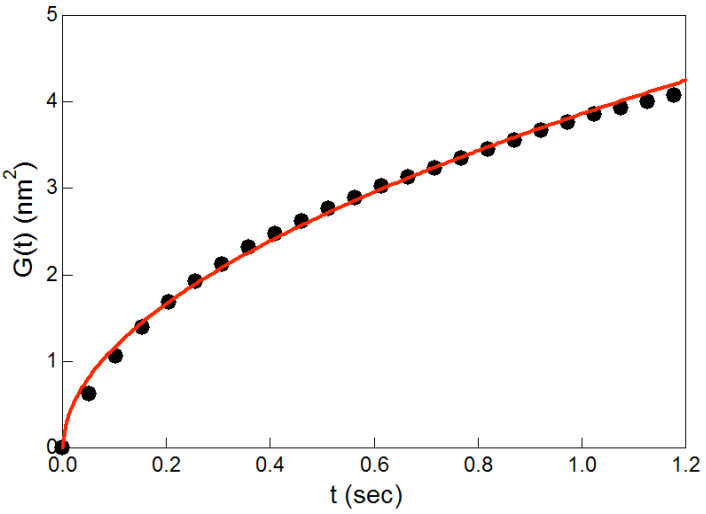

Fig. 6 (Color online). Typical correlation function *G(t)* curve and fit curve. The fit, using Eq. (4), extracts the best fit values, $G_0 = 3.86 \pm 0.28$ nm^2, $1/n = 0.52 \pm 0.07$.

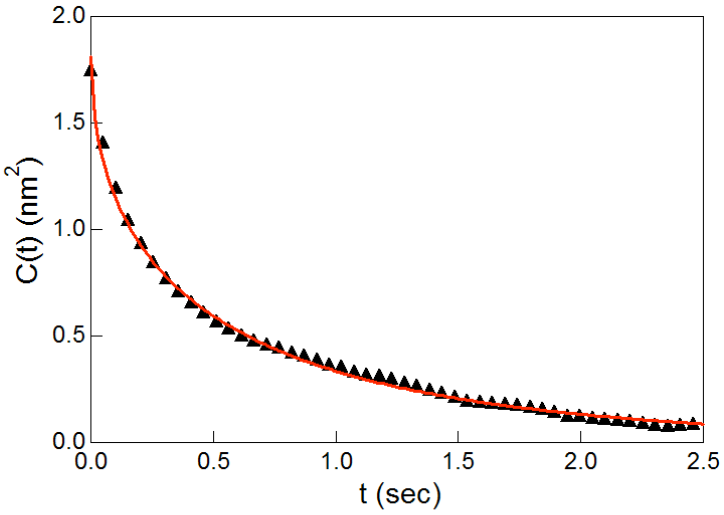

Fig. 7 (Color online). Typical autocorrelation function C curve and fit curve. The fitting, using Eq. (6), extracts the best fit values, $C(0) = 1.81 \pm 0.36$ nm^2 and $\tau_c = 1.77 \pm 0.49$ s.

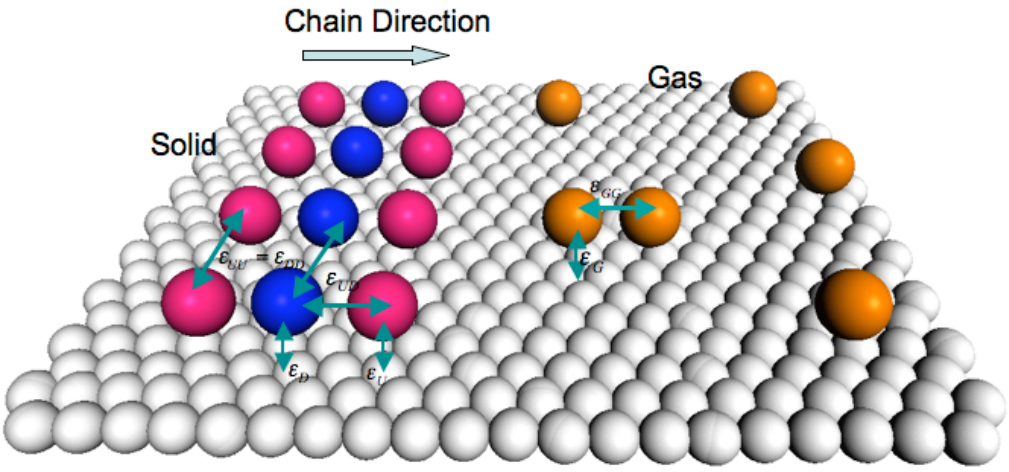

Fig. 8 (Color online). Schematic illustration of molecular system with variable substrate interactions as well as intermolecular interactions.

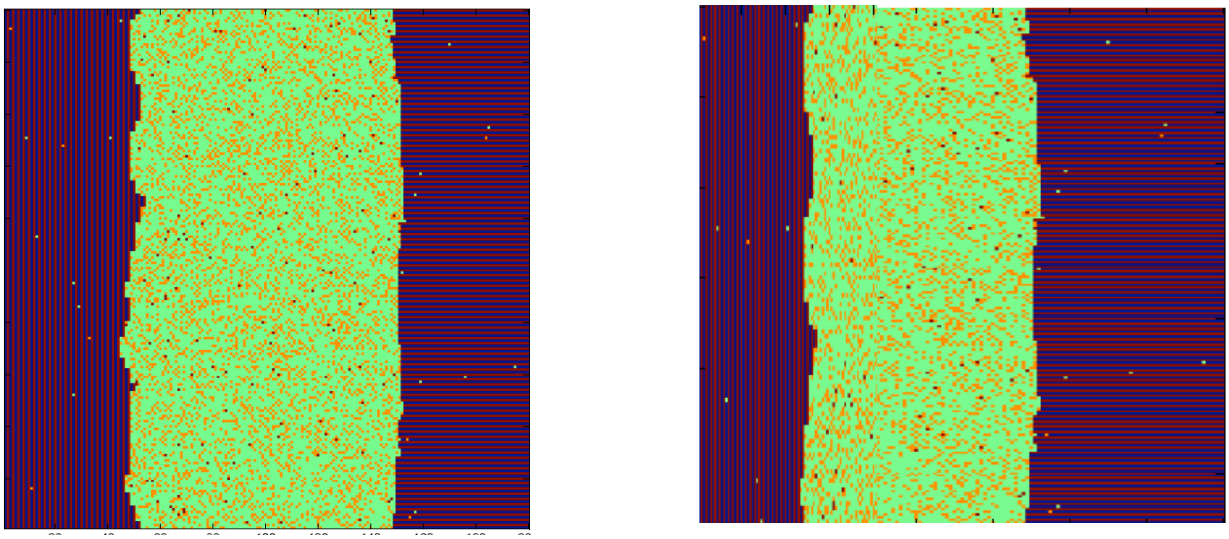

Fig. 9 (Color online). The simulation result, 5000 steps (the left one is original, the right one has been compressed by 57%(nearly 1/sqrt(3)) along the chain direction)

$$\varepsilon_U = 0.39eV, \varepsilon_D = 0eV, \varepsilon_{UD} = 0.30eV, \varepsilon_{UU} = \varepsilon_{UU} = 0.06eV, \varepsilon_G = 0.53eV, \varepsilon_{GG} = -0.015eV$$

Chapter 6 Electromigration on bare and decorated Ag(111) surfaces

In this chapter, we will discuss electromigration on Ag(111) surfaces. Using STM, we can directly track atomic motion driven by current flow. We will discuss how the adsorbates, C_{60}, stabilize the surfaces and how decorated steps and islands change due to wind force.

6.1 Island motion driven by wind force

Introduction

There has been a great deal of theoretical interest in how islands and vacancy-islands move under the influence of an electromigration force. Experimental realization of such experiments is hindered however by the tendency of islands to decay under the elevated temperatures (Joule-heating) that typically occur during an electromigration experiment. Here we have developed a special design to allow quantitative observation of island motion under electromigration.

Experimental

The samples for these electromigration experiments are shown in Fig. 1. The active parts for measurements are the Ag stripes, with width ~ 50 μm and thickness ~ 350 nm. Two electrodes connecting the Ag stripes are also Ag thin films, but thicker (>600 nm) and wider (~1.5 mm). This geometry offers the advantage to apply a high current density on the Ag stripes while keep the temperature not too high. To fabricate these samples, we employed a two-step thermal deposition method. The first step is to thermally evaporate Ag onto a freshly cleaved mica substrate through a mask with slot width 50 μm. The deposition conditions are similar to those we used for our previous Ag thin film growth. Then the electrodes were deposited.

The samples were then transferred into the JEOL treatment chamber. After several Ar^+ sputtering and annealing cycles, atomically clean Ag(111) surfaces can be obtained. In order to generate a desirable surface for the electromigration measurements, we used short time sputtering in the last cycle without annealing. A typical surface morphology is shown in Fig. 2 obtained by 1 keV Ar sputtering for 10 mins without annealing. In Fig. 2, we can see the height of adatom islands or the depth of vacancy islands are about 5 to 8 monatomic layers. Starting with this surface morphology, we run DC current through stripes. After thermal stabilization (usually about 30 to 40 mins), we approach STM tip onto the middle of the stripe and measure the motion of monatomic adatom islands driven by wind force.

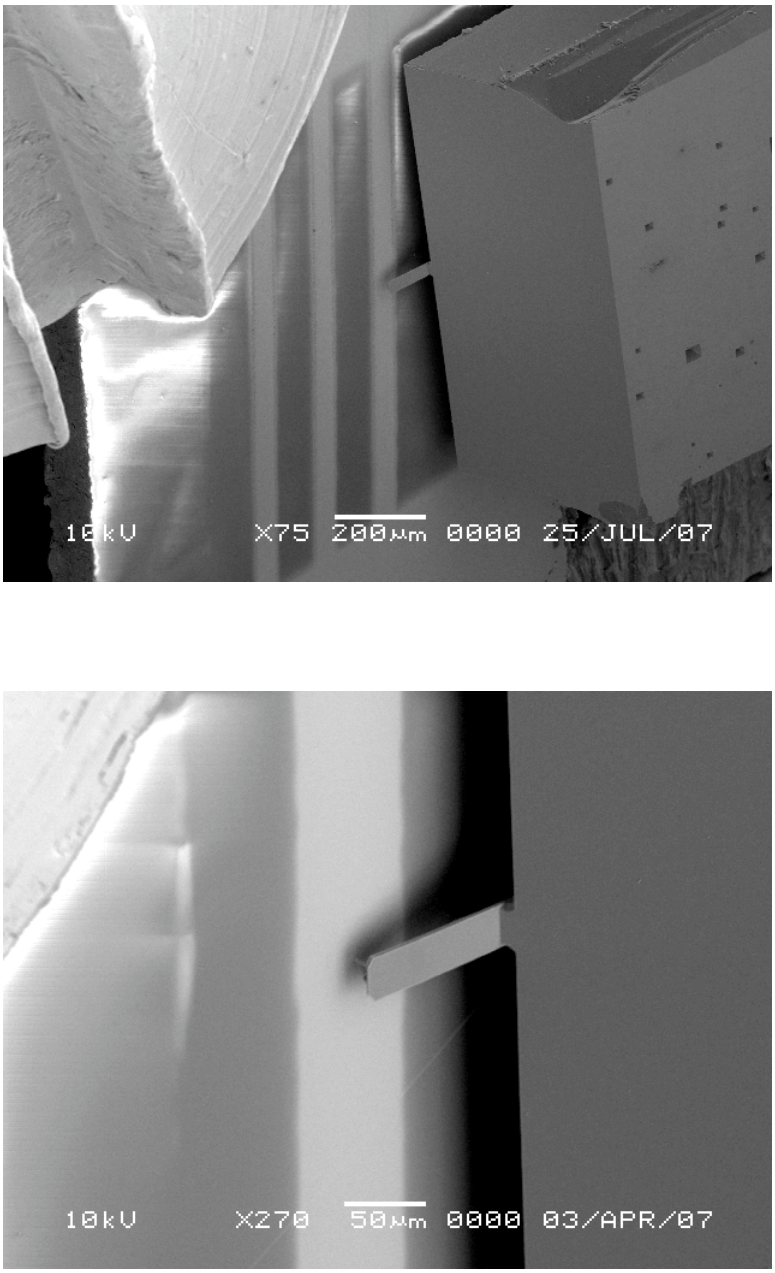

Fig.1 Ag stripes and scanning tip

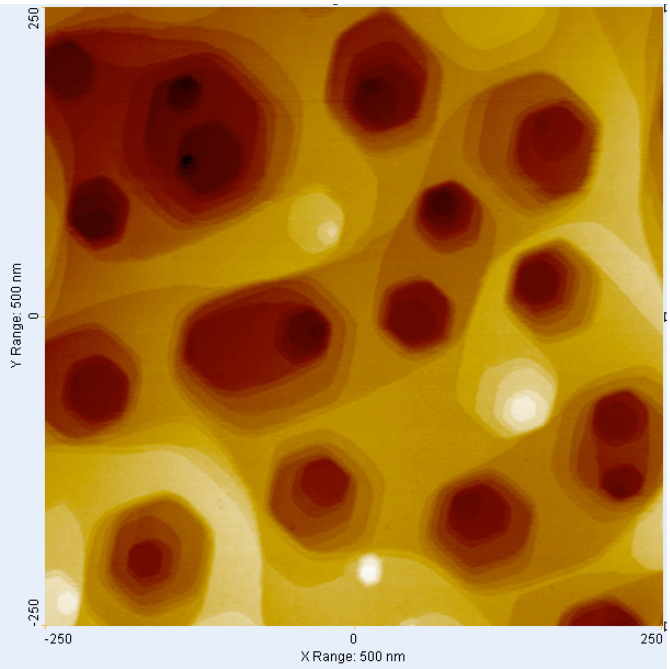

Fig. 2 (color online) Topography image of Ag stripes after sputtering

In experiments, we find that the adatom islands move opposite to the current direction. Associated with the biased motion, the islands also decay. By changing the current direction, we can make an island "U turn" as shown in Movie S1. In order to quantitatively and precisely measure the biased motion of monolayer adatom islands, the first thing to be avoided is the effect from nearby step edges or island edges. Using this strategy, we move adatom islands onto the central area of a large island or a large terrace, and then keep recording the island motion and size change until the islands totally decay by continuously scanning. During the entire measuring process, the measured island is far away from any step edge or island edge (much lager than the critical distance ~ 6 nm pointed out by Morgenstern and Geisen [40, 217]). The fastest scan speed is 60 s per 256 × 256 pixel image and 120 s per 512 × 512 pixel image. The typical tunneling parameters are ~50 pA at sample bias ~ 1.6 V. Under these tunneling conditions the tip-sample

interactions can be negligible for Ag surfaces [25, 32]. Fig. 3 shows four images chosen from a movie series. Using our image processing method, we can calculate the area and determine the center of mass of the measured island in each image.

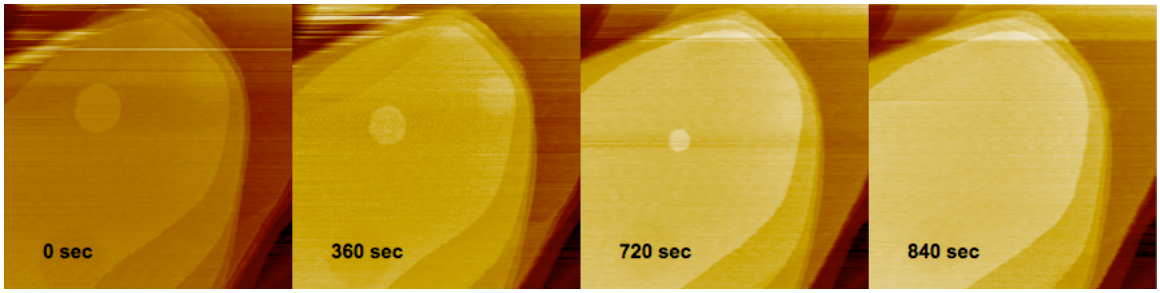

Fig. 3 (color online) Biased motion of an adatom island driven by wind force (54 pA at −1.67 sample bias; scan size 400 × 400 nm^2).

Results and discussions

At current density ~ 6.7 × 10^9 A/m^2, for adatom islands with size ~ 60 nm, the biased motion can be easily seen by comparing two sequential STM images. For comparison, here we present two data sets for two islands measured in exactly the same area (in movie S1). The only difference in driving the motion of two islands is the current direction. The mass center of the islands as a function of time is shown in Fig. 4a. For the island M4, the current is along the Y- direction and for the island M3, the current is along the Y+ direction. The biased motions are clear from the difference in the parallel direction and the perpendicular direction. In the perpendicular direction, there is no obvious biased motion. In the parallel direction, the displacement is up to 90 nm until the islands totally decay. The island motion direction is opposite to the current direction, and along the wind force direction. As we mentioned in Chapter 1, on metal surfaces, the wind force

direction is opposite to the current direction since the carriers here are electrons. These results are the first to confirm the theory prediction that for motion dominated by step-edge diffusion monolayer adatom islands move opposite to the current direction [218]. While islands move in the current-biased direction by current, the island area linearly decreases with time, which is similar to the linear decay behavior of islands on Ag(111) surfaces without current [40]. Comparing the decay rate for the islands as shown in Fig. 4b, we find that even though the islands move in opposite directions, their decay rates are almost same. By fitting the curves, we obtain the decay rate as -5.76 ± 0.11 (nm^2/s) for island M4 and -5.13 ± 0.20 (nm^2/s) for island M3. This is reasonable since the wind force only breaks momentum symmetry, but other crucial conditions to govern the decay rate, like temperature, diffusion barrier, and electron energy, are still identical or mirror-symmetric.

From the displacement results, we can directly calculate the drift velocity of adatom islands. For each data point, the derivative is taken by averaging the slopes of its two adjacent data points, and the result is shown in Fig. 5. In the results we can clearly see that the drift velocity tends to increase as time goes by. The range of velocity is from 0.02 nm/s to 0.12 nm/s. This is the first time in experiments to directly measure the monolayer island motion driven by wind force, even though this has been predicted in a theory some time ago [218].

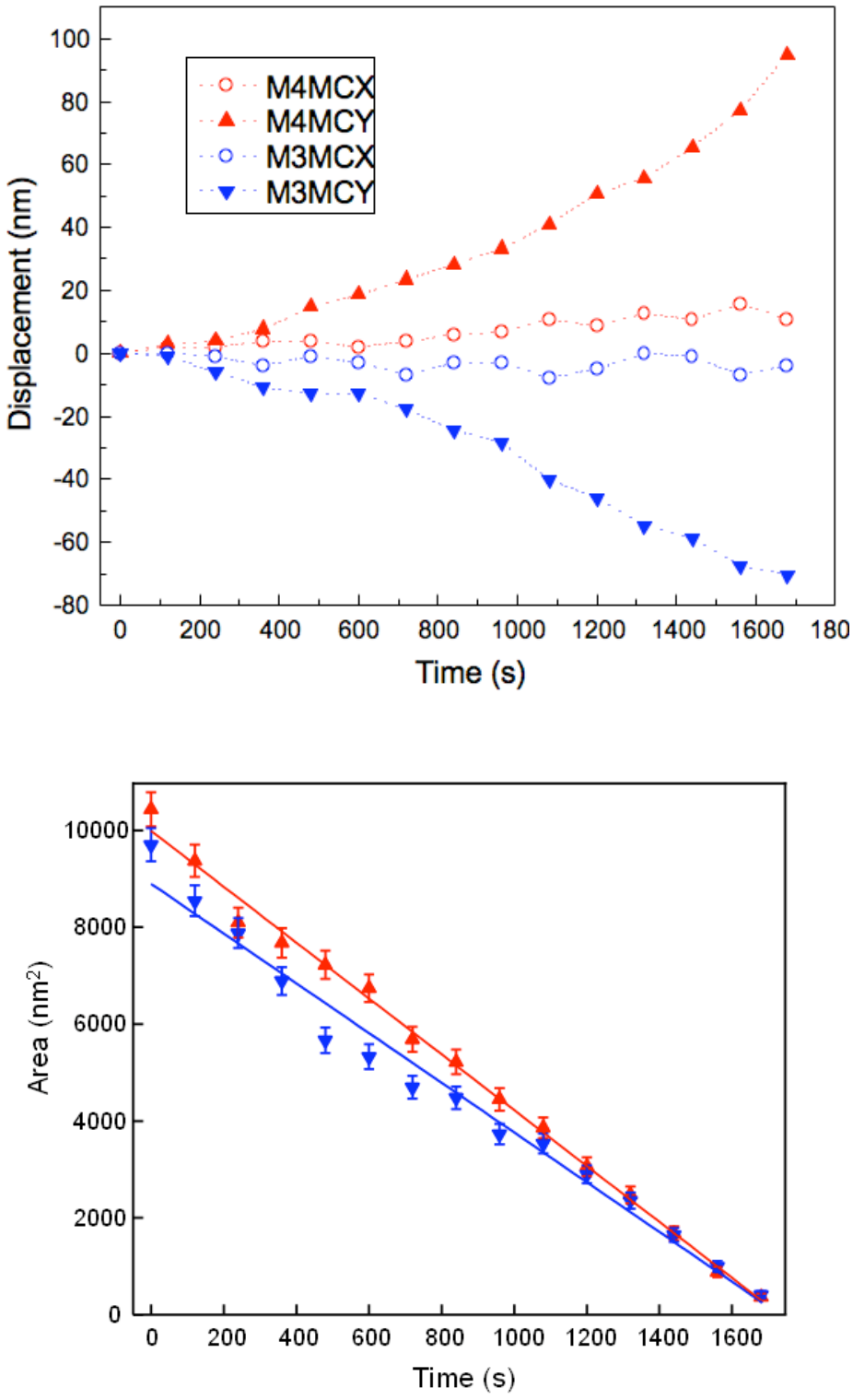

Fig. 4 (a) The displacement of the island mass centers vs. time. Here is the Y direction is parallel to the current direction, and the X direction perpendicular to the current direction. (b) island areas vs. time.

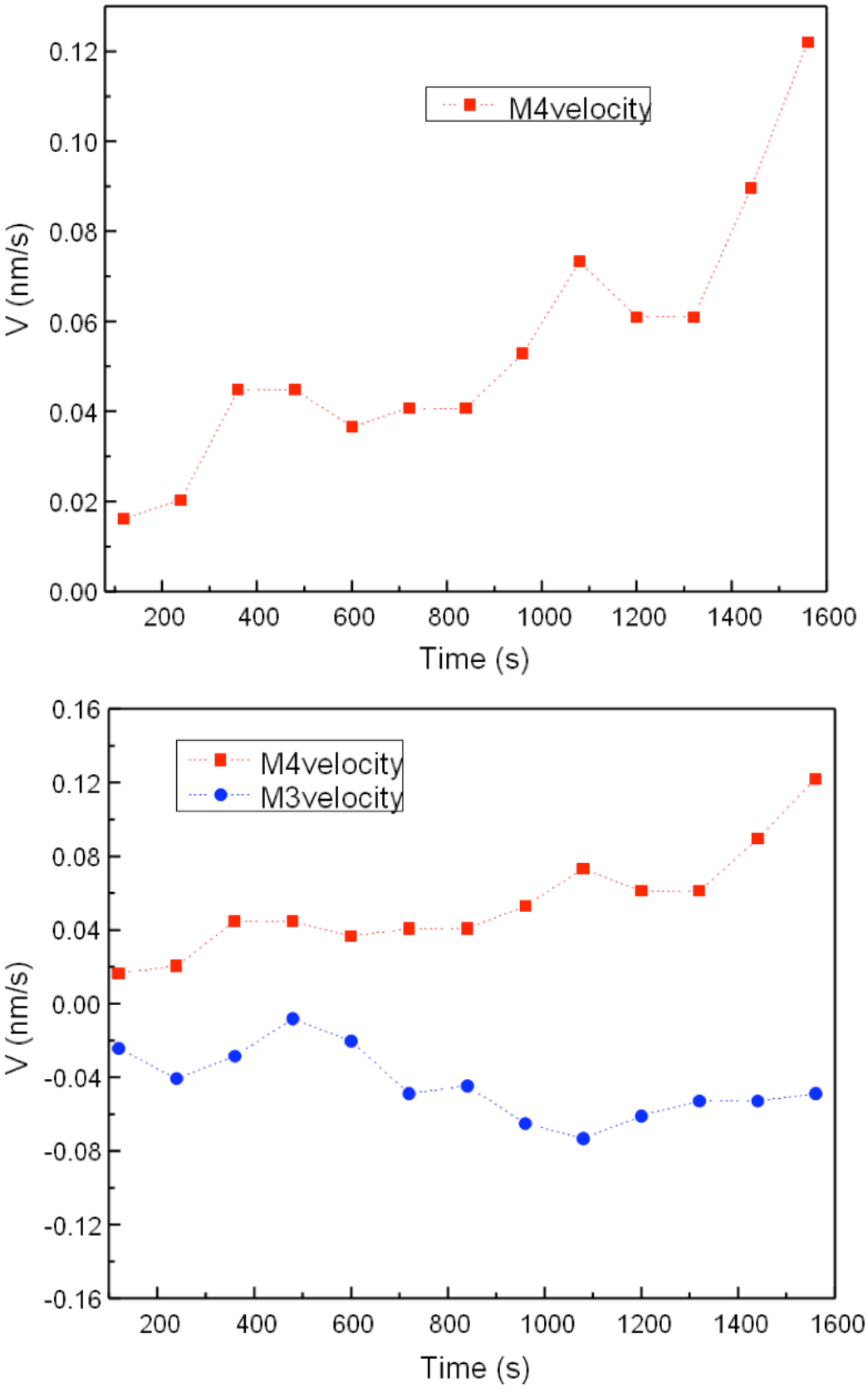

Fig. 5 velocity vs. time.

In Fig. 4, we already see that the islands decay with time. Straightforwardly we can obtain the drift velocity as a function of the island area, and the result is presented in Fig. 6, where we use the effective radius instead of island area. This result clearly indicates that the drift decreases as island size increases. According to the theoretical calculations, the size dependence of the drift velocity is related to the mode of mass transport on surfaces. For the periphery diffusion (PD) limit case $V \propto 1/R$, for the terrace diffusion (TD) limit case is a constant and for the attachment/detachment (AD) case $V \propto R$ [218]. In Fig. 6, the black solid line is the one-parameter fit of the experimental data $V = P1/R$ with $P1 = 1.93 \pm 0.09$ (nm^2/s). As we mentioned above, directly differentiating usually causes huge noise in data, so here our experimental result is in good agreement with the PD limit electromigration in the theoretical prediction. From other experimental observations, we can know that the mode of mass transport is in the step-edge diffusion limit region. First we observe that the vacancy islands move in the direction of the current, and opposite to the adatom islands motions. According to theoretical prediction, this is only possible for the PD limit case. For the TD and AD cases, both adatom and vacancy islands drift opposite to the current direction [218]. Furthermore, we measured the temperature of the sample after doing the electromigation measurement, and the result is shown in Fig. 7. To optimize the conditions for the electromigation measurement, the current in the whole measurement is 0.35 A with sample temperature 318 K. At this temperature, according to Giesen's and our studies on the step fluctuations on Ag(111) [25, 47], we also know that the mass transport is in the PD limit region when temperature is below 450 K.

In theory, the complete formalism of the drift velocity is

$$V = \frac{aD_L F}{k_B T R_0}, \qquad (1)$$

where a is the lattice constant, D_L is the macroscopic step diffusion constant, F wind force, and R_0 the radius. Wind force is a function of electrical field E and the effective valence z^*, $F = z^* eE$. Here the electrical field can be directly calculated from the current and the geometry of the sample. By fitting V(R), we obtain $V^* R_0 = 1.93$ nm^2/s. Through Eq. 1, we obtain the direct relation between z^* and D_L, $D_L = 1.56\times10^6/z^*$ (nm^2/s). Using the value for the z^*=360, obtained in the previous study on the step fluctuations under the wind force [116], the resulting macroscopic step diffusion constant, $D_L = 4.33 \times 10^3$ nm^2/s. From the value of the macroscopic step diffusion constant, we can further calculate the value of the diffusion constant of adatoms along the island edges, D_{st}. The definition of the macroscopic step diffusion constant D_L is $D_L \equiv c_{st} D_{st}$, where c_{st} is the adatom concentration along the island edges, which can be readily calculated, $c_{st} = e^{-2\varepsilon / k_B T}$. The value of kink enegy is 0.1 eV for Ag(111) in UHV [39, 219], so $c_{st} = 6.76 \times 10^{-4}$, and therefore $D_{st} = 6.4 \times 10^6$ nm^2/s.

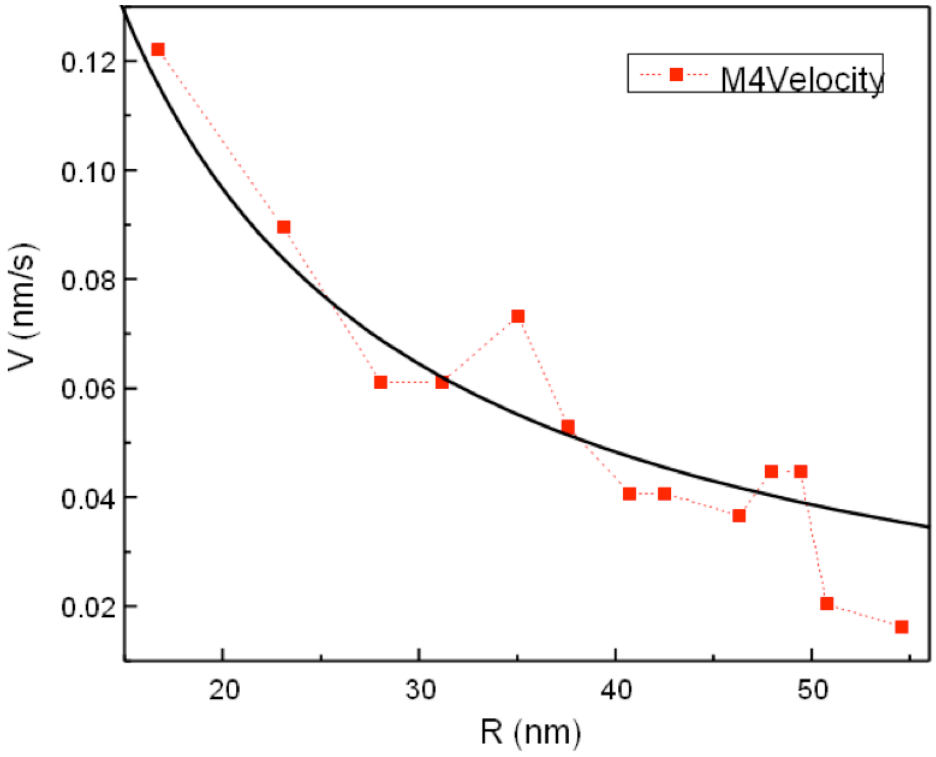

Fig. 6 velocity vs. radius.

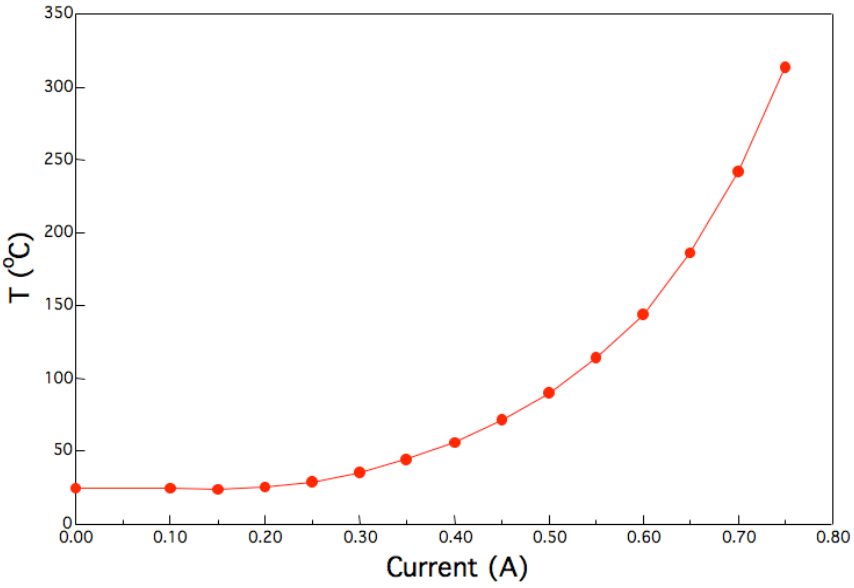

Fig. 7 sample temperature

6.2 Bending of decorated steps

Introduction

After investigating the electromigration on the bare surface of the Ag stripes as described in detail in the first section, we deposit C_{60} onto the surfaces of the Ag stripes. The purpose of this study is to address the effects of adsorbates on electromigration behaviors.

Experimental

The deposition conditions are similar with those described in Chapter 4 [49, 50]. By tuning the deposition temperature and time, the C_{60} coverage can be controlled from submonolayer down to the precise coverage that C_{60} just fully decorates the steps or island edges with almost no C_{60} islands in Fig. 1. shows a topography image of the submonolayer C_{60}, in which the inset is the zoom-in image of a C_{60} monolayer island. Fig. 2a represent steps decorated by C_{60}. We can see two monatomic steps decorated by single C_{60} chains, which are crossed by the marked white line, and the corresponding line profile shown in Fig. 2b.

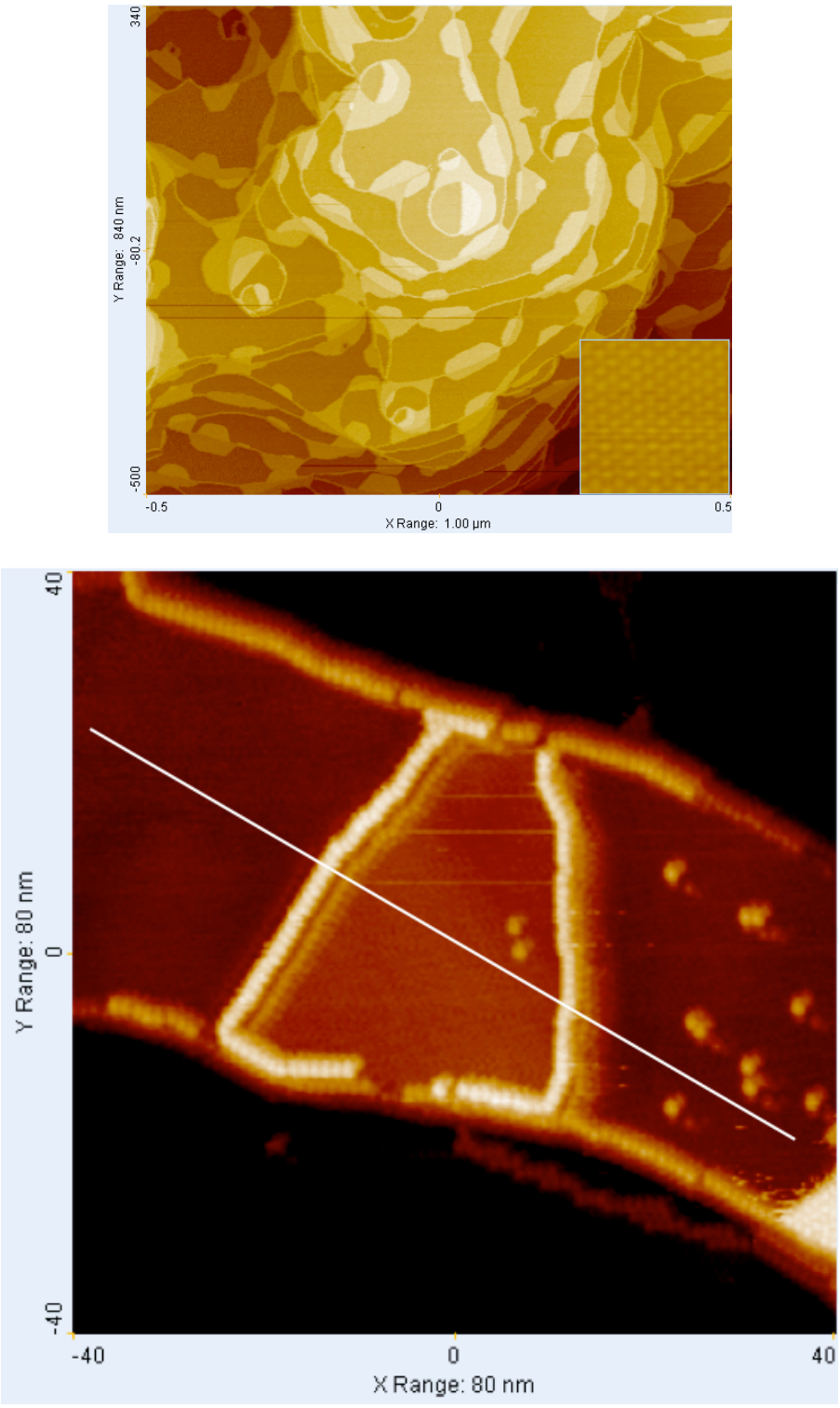

Fig. 1 Topography images of submonolayer C_{60} on Ag(111). Inset is a zoom-in image of a C_{60} monolayer island (1×1 μm^2 and 80×80 nm^2 respectively).

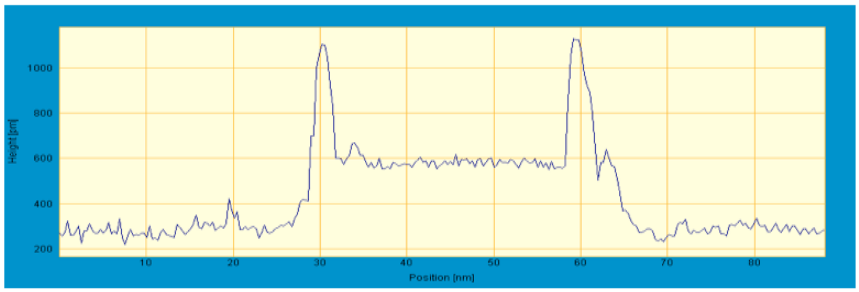

Fig. 2 Line profile of the decorated step marked by a while line in Fig. 1.

Results and discussions

Starting from the decorated surfaces with steps or island edges fully covered by C_{60} but almost no C_{60} monolayer islands, we add DC current through the sample. At 0.35 A current, the typical topography image is represented in Fig. 3. The current direction is in the vertical direction of the figure. Dramatically different form the morphology of the surface without current, here most decorated steps are roughly parallel to the current direction. In experiments we also observe that the steps move from perpendicular to parallel to the current direction in real time.

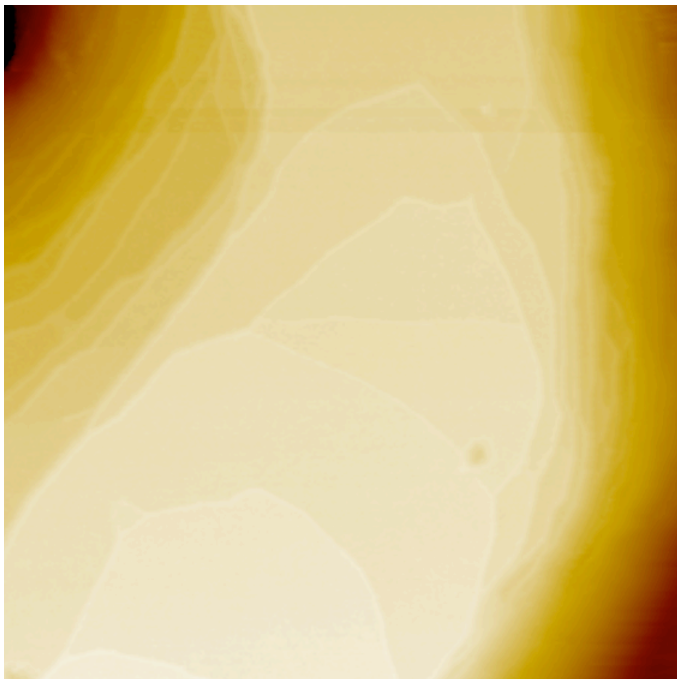

Fig. 3 Topography image under wind force (500 × 500 nm^2).

In order to quantify how the wind force affects the monatomic decorated steps, we focus on pinned steps to study how their curvature is altered by varying current direction. Fig. 4 shows different stable configurations of the same monatomic decorated step when the current through the sample is switched in direction. The arrows in each image indicate the current direction. The current density here is 6.67×10^9 Am^{-2}. We can see that the step consistently bends against the current direction. As we discusseded previously, on metal surfaces, the wind force is opposite to the current direction. The decorated step looks just like it is being blown by a wind force.

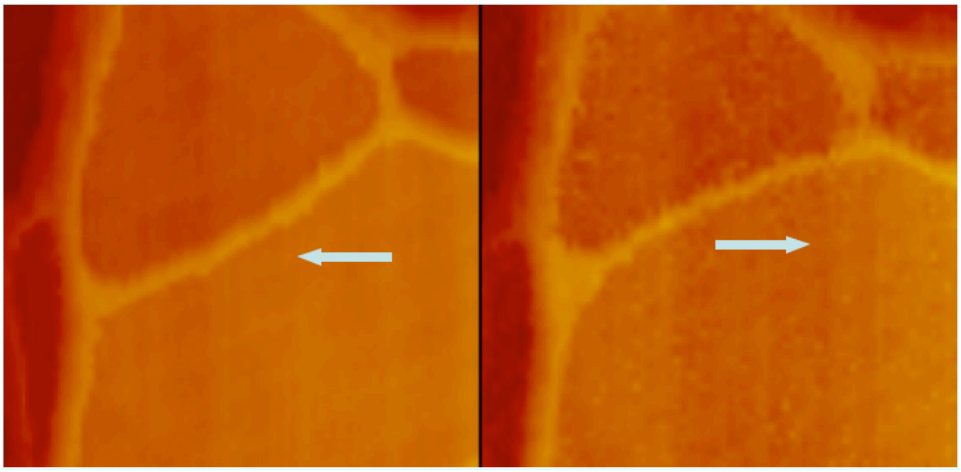

Fig. 4 Bent step due to wind force (86 × 86 nm^2).

In experiments, we observe behavior similar to the decorated island edges on Ag(111) surfaces without current flowing through [50], the decorated steps also fluctuate. Using our image processing method, we can extract the decorated step position from STM images. In order to obtain the equilibrium configuration, we average more than 10 images for each configuration. The results are represented in Fig. 5. The red circle and the blue square are the left and right configurations shown in Fig. 4, respectively. In both cases, the step shape is pretty smooth except at the ends. The ends of the step are connected to large multilayer steps, which together with a few C_{60} molecules in a cluster stabilize the ends of the measured step. These few C_{60} molecules cause the uncertainty in our image processing at the ends.

According to the Gibbs-Thomson effect, different step configurations correspond to different chemical potentials. Here the configuration change is due to the wind force. Using a simple model, we have

$$F \times \Delta x = \Delta \mu, \qquad (1)$$

where F is the wind force, μ the local chemical potential, and x the shift distance along the wind force direction. Consider the current applied here is with the same amplitude but opposite direction, so the reference position can be arbitrary. Then Δx is the displacement between the two configurations, and $\Delta\mu$ is the difference between the two equilibrium shapes. On (111) surfaces, the explicit relation between the local chemical potential and the curvature is

$$\mu = -\frac{\sqrt{3}}{2}\tilde{\beta}a^2 k, \qquad (2)$$

where $\tilde{\beta}$ is the step stiffness and a lattice constant. From our previous study on the decorated island fluctuations, we have $\tilde{\beta}$=0.65 eV/nm [50].

Given the smooth step shape, we can determine the local curvature of the step configurations. The solid lines in Fig. 5 are polynomial fits to the experimental data. The fitting is very well, and main discrepancy comes at the ends, due to uncertainty in the image processing as discussed above. Through the polynomial fits, we then calculate the curvature along the step. By integrating along the whole step, we obtain the resulting wind force, F=0.13 meV/nm. For comparison, using z^*=360 calculated from the step fluctuations under wind force [116], at this current density, the corresponding wind force for a bare Ag step is 0.04 meV/nm. So at the same current density, the wind force acting on the decorated steps is about 3 times the wind force on the bare steps.

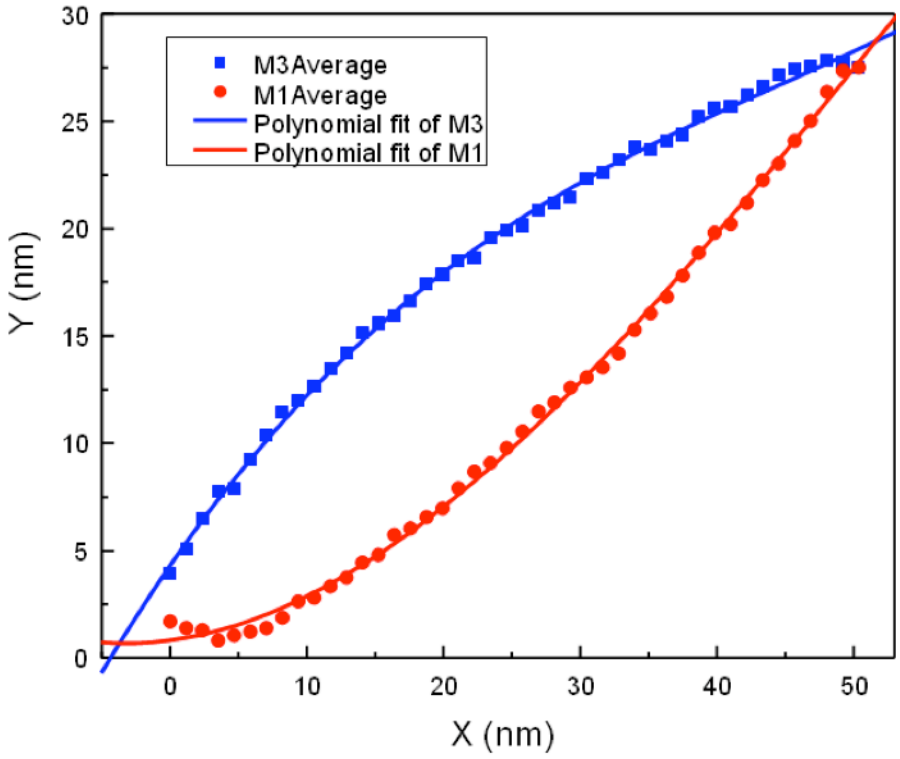

Fig. 5 equilibrium configurations under opposite wind force

Chapter 7 Conclusions and outlook

Mass transport mechanism on nanoscale electronic devices is crucial for their stability and performance. To systematically investigate this problem, at first we develop the concept of the generalized survival probability using steps on Ag(111) as a model and propose a generalized inside survival probability to connect explicitly fluctuations to stability. Then from the pinned steps on Ag(111), the correlation length are directly measured and reveal the effects of surface impurities on step fluctuations. For bare metal surfaces, we also have used STM to image the surfaces of Ag nanowires and related thermal dynamical properties.

In order to study how molecules affect surface mass transport and the dynamics of the metal/molecule interfaces. We have thoroughly investigated C_{60} and Ag(111) system with precise C_{60} coverage control. We have characterized fluctuation properties of segments of step edges partly covered by C_{60}. The distribution of C_{60} at step edges exhibits a step orientation dependence: low-symmetry step edges are more favorable for C_{60} binding. That fluctuations of these "confined" steps is consistent with step-edge diffusion limited fluctuations. Parameters extracted from temporal correlation and autocorrelation analysis consistently indicate that close-packed steps have smaller fluctuation magnitude and higher step mobility than low-symmetry steps. The measured system sizes of step segments with different lengths show at most a weak step-length dependence. C_{60} molecules are not acting as pinning points that constrain mass transport along the step edges. Then we have further explored the dynamics of chains of C_{60} bound

to a circular layer of Ag atoms, which provide a model system for characterizing thermal fluctuations at electrical contacts in nanoelectronic and molecular electronic devices coupling into the electrical signal via changes in the electron transmission probabilities. Both the time constant and squared-amplitude of the fluctuations of the C_{60} ring vary as k^{-2}, where k is the mode of excitation, with room temperature values of $(11.5\ nm^{-2}s)(R/k)^2$ and $(0.009\ nm)(R/k^2)$ respectively, on the circular boundary of radius R. Fluctuations of clean Ag interfaces have a different dependence on k and R, indicating that different mechanisms drive the fluctuations of the C_{60} ring and the underlying Ag step. The substrate boundary and the molecular fluctuation modes will thus contribute distinct frequency signatures, in the range of 1 - 100 Hz and 0.01 - 0.08 Hz, respectively, to any structure-sensitive transport measurement.

Fluctuations of interfacial boundaries in an organic thin film have been measured quantitatively. The molecule studied, ACA, has a rectangular anisotropy in its intermolecular interactions that results in growth of chain-like structures in monolayers on Ag(111). The fluctuations of the boundaries between the ordered chain-like phase and a disordered phase show that the mass transport mechanism on the boundaries is dominated by molecular exchange between two phases. Surprisingly the orthogonal boundaries show little asymmetry in free energies or fluctuation time constants, in distinct contrast to expectations based on simple lattice gas (Ising) models with anisotropic intermolecular interactions. Generalization of the lattice gas model to include the effects of different substrate interactions induced by conformal changes between the molecules in the condensed and 2D gas phases leads to a multi-component Blume-Emery-Griffiths (BEG) model that straightforwardly resolves the apparent discrepancy

with experiment. The model predicts that the novel domain shapes, boundary fluctuations and phase densities seen in experiment arise from a balance between favorable anisotropic pair interactions in the chain phase and less favorable substrate interactions. Furthermore, we have demonstrated a method to fabricate C_{60} overlayers with controlled spacing and chirality by reactive co-adsorption with the ACA. Structural control is achieved by the mismatched symmetries of the co-adsorbates, as well as specific intermolecular and adsorbate-substrate interactions. The resulting supramolecular structure has a C_{60} period nearly three times as large as the normal C_{60} 2-D packing of 1 nm, and exists in enantiopure domains with robust chirality.

Using experimental and theoretical tools for investigating dynamics on macroscopic surfaces, we have explored dynamics on Ag nanoiwres, metal surfaces decorated with organic molecules, metal/molecule interfaces and phase boundaries in organic monolayers. Especially we have tracked adatom motion on surfaces at atomic scale. These studies provide profound insight into the mass transport mechanism for promising nanoscale devices on both OFF and ON status. Naturally, along this direction we can explore thermodynamical properties of more low dimensional structures, for instance, nanowires, molecular devices, and layered materials, graphene or MoS_2. Especially, electromigration phenomena on these kinds of low dimensional materials should be very interesting. In the opposite direction, measuring transport properties may make explicit connections to the thermodynamics on the surfaces, for example, noise. Since now the transport measurements are under the conditions that the devices surfaces are not well known, combining transport and surface properties should be promising and extremely important.

Appendix

A1. Ripple structures on Ag(111) surfaces

The ripple structures on Ag(111) are formed in the areas confined by C_{60} islands or/and C_{60} chains which decorate steps and island edges as shown in Fig. 1. For simplicity, we focus on the ripple structures near the long straight edges of C_{60} islands shown in Fig. 2. These ripples are parallel, with the edges running in the [11-2] direction. The distance between neighboring ripples is ~ 3.75 nm. As shown in the zoom-in image in Fig. 3, in the [11- 2] direction, the atom periodicity is 0.5 nm. Considering the Ag lattice constant is 0.2889 nm, the periodicity of a unit cell is approximately $13 \times \sqrt{3}$. In Fig. 3, individual Ag atom can also be seen vaguely.

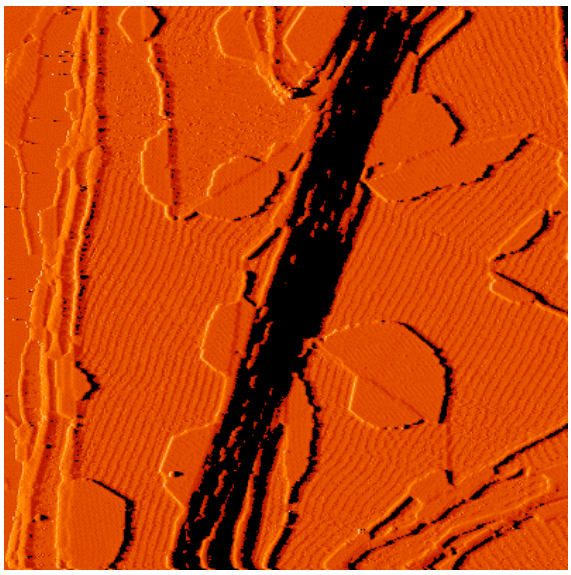

Fig. 1. Differential STM image of ripple structures (204.18 × 204.18 nm, I = 0.10 nA, V = –1.40 V)

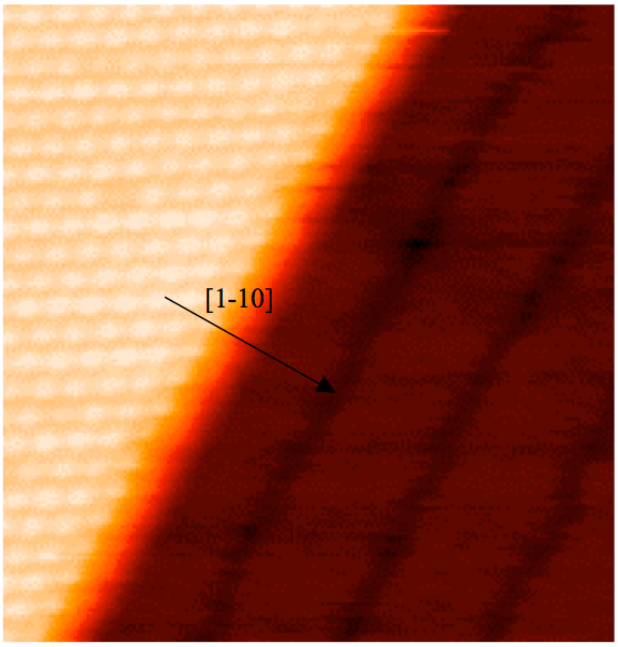

Fig. 2. Ripple structures near the straight edge of a C_{60} island (19.2 × 20.2 nm, I = 0.10 nA, V = –1.5V)

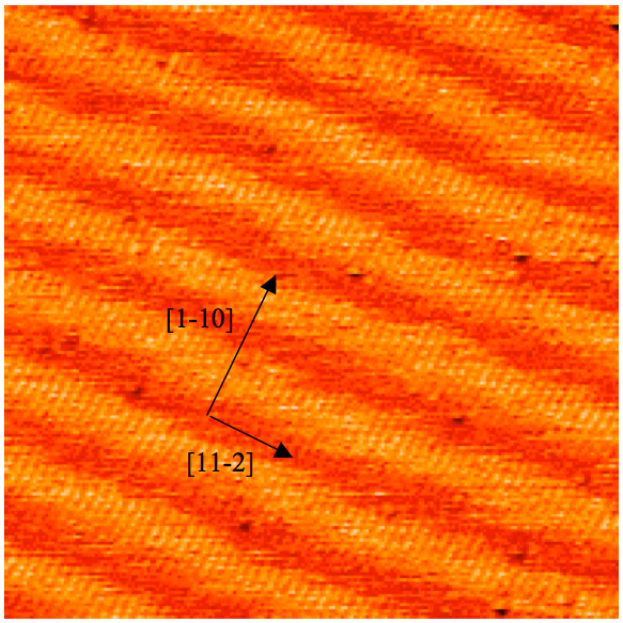

Fig. 3. Vague atomic resolution image of the ripple structure (23.30 × 23.30 nm, I = 0.52nA, V = –0.58V)

Though the mechanism for forming these ripple structures is not very clear, it should be related to surface strain since these ripples are only observed in confined areas.

Recently theoretical calculations of C_{60}/Cu (111) pointed out the Cu-Cu bond length of the triangle right underneath a C_{60} expanded 5-6%(2). It is reasonable to assume a similar behavior here, that the C_{60}-Ag (111) interaction modifies the Ag-Ag bond length of Ag atoms underneath the molecule. Then the expansion of these Ag-Ag bonds would cause strain that triggers the forming of these ripple structures. On the other hand, if we believe these ripple structures are one kind of reconstruction on Ag (111), comparing with the $23 \times \sqrt{3}$ reconstruction of Au (111) (3), (4), we can find some more similar properties. One of them is that local defects sensitively affect the ripple pattern. In Fig. 4 we can clearly see these features.

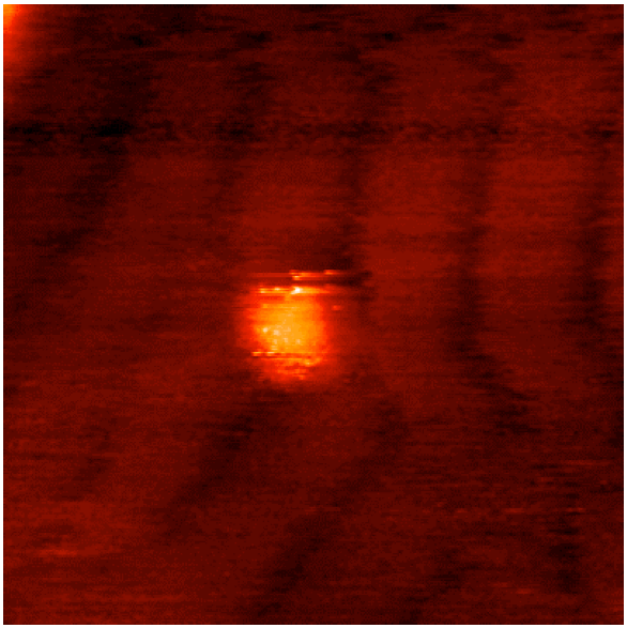

Fig. 4. Ripple structure around a defect (15.9 × 15.9 nm, I = 0.3nA, V = –1.0V)

The ripple structures are dramatically different from surface electron density waves, which are parallel to monatomic steps, monolayer Ag island edges or edges of C_{60} islands, as shown in Fig. 5. The electron density waves always fade away as the distance from the edge increases.

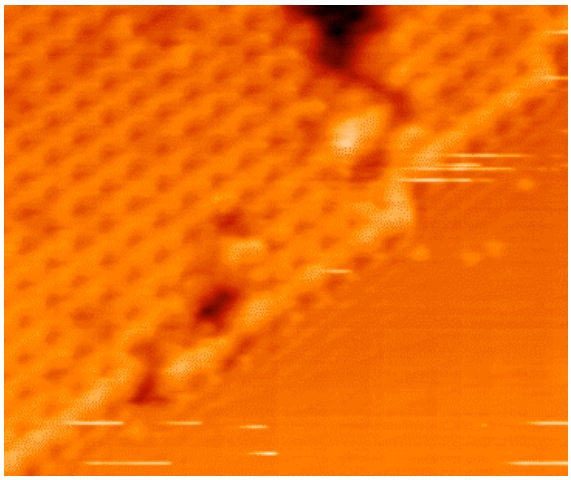

Fig. 5. Electron waves along an edge of a C_{60} monolayer island (16.19 × 13.52 nm, I = 0.10 nA, V = –1.74 V)

In our Ag nanowire (NW) experiments, we also observed similar ripple structure on the bare Ag surface near a Ag NW, as shown in Fig. 6. The ripples are roughly parallel to the Ag NWs. Very surprisingly, the ripples cross over the steps. This observation may further confirm the hypothesis that the ripple structures are due to surface strain.

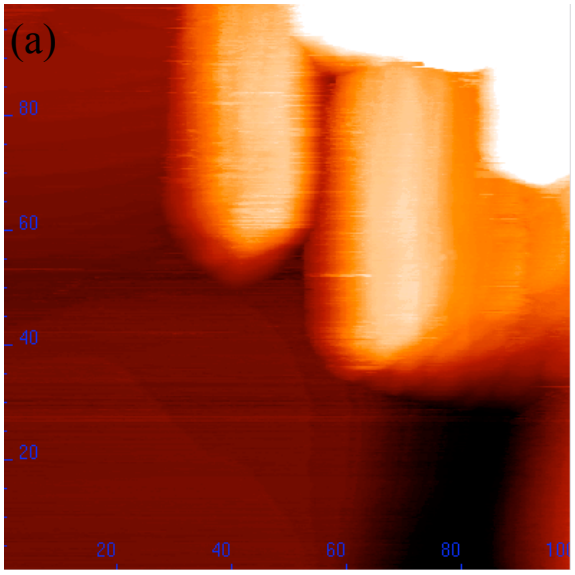

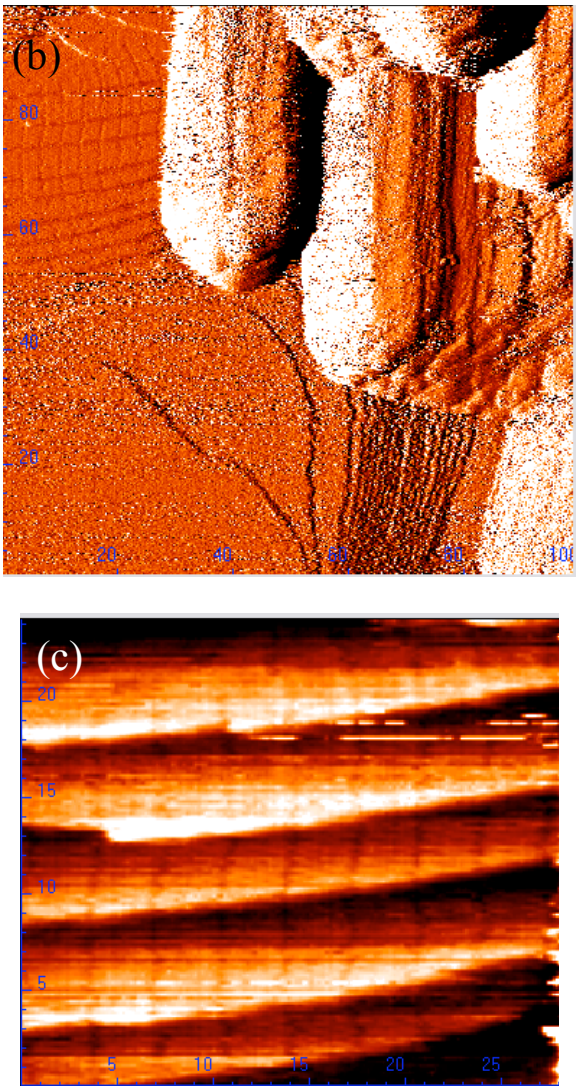

Fig. 6. Ripple structure near a Ag nanowire (100 × 100 nm, I = 30.4 pA, V = –0.91 V) ((a), topography image, (b) corresponding differential image, and (c) zoom-in image in (a)).

References

1. Aviram, A. and M.A. Ratner, *Molecular Rectifiers.* Chemical Physics Letters, 1974. **29**(2): p. 277-283.
2. Park, H., et al., *Nanomechanical oscillations in a single-C-60 transistor.* Nature, 2000. **407**(6800): p. 57-60.
3. Herring, C., *Some Theorems on the Free Energies of Crystal Surfaces.* Physical Review, 1951. **82**(1): p. 87-93.
4. Wortis, M., *Chemistry and Physics of Solid Surfaces*, ed. R. Vanselow and R.F. Howe. Vol. VII. 1988. 367-428.
5. Fisher, M.E., *Walks, Walls, Wetting, and Melting.* Journal of Statistical Physics, 1984. **34**(5-6): p. 667-729.
6. Bartelt, N.C., T.L. Einstein, and E.D. Williams, *The Role of Step Collisions on Diffraction from Vicinal Surfaces.* Surface Science, 1992. **276**(1-3): p. 308-324.
7. Fisher, M.P.A., D.S. Fisher, and J.D. Weeks, *Agreement of Capillary-Wave Theory with Exact Results for the Interface Profile of the Two-Dimensional Ising-Model.* Physical Review Letters, 1982. **48**(5): p. 368-368.
8. Gruber, E.E. and W.W. Mullins, *On Theory of Anisotropy of Crystalline Surface Tension.* Journal of Physics and Chemistry of Solids, 1967. **28**(5): p. 875.
9. Jayaprakash, C., C. Rottman, and W.F. Saam, *Simple-Model for Crystal Shapes - Step-Step Interactions and Facet Edges.* Physical Review B, 1984. **30**(11): p. 6549-6554.
10. Chui, S.T. and J.D. Weeks, *Phase-Transition in 2-Dimensional Coulomb Gas, and Interfacial Roughening Transition.* Physical Review B, 1976. **14**(11): p. 4978-4982.
11. Bartelt, N.C., et al., *The Equilibration of Terrace Width Distributions on Stepped Surfaces.* Surface Science, 1992. **273**(1-2): p. 252-260.
12. Bartelt, N.C., et al., *Brownian-Motion of Steps on Si(111).* Physical Review B, 1993. **48**(20): p. 15453-15456.

13. Wilde, R.E. and S. Singh, *Statistical Mechanics: Fundamentals and Modern Applications*. 1997: Wiley-Interscience.
14. Binnig, G., et al., *Tunneling through a Controllable Vacuum Gap.* Applied Physics Letters, 1982. **40**(2): p. 178-180.
15. Binning, G., et al., *Surface Studies by Scanning Tunneling Microscopy.* Physical Review Letters, 1982. **49**(1): p. 57-61.
16. Muller, E.W., **Das Feldionenmikroskop.* Zeitschrift Fur Physik, 1951. **131**(1): p. 136-142.
17. Smith, D.J., et al., *Dynamic Atomic-Level Rearrangements in Small Gold Particles.* Science, 1986. **233**(4766): p. 872-875.
18. Iijima, S. and T. Ichihashi, *Structural Instability of Ultrafine Particles of Metals.* Physical Review Letters, 1986. **56**(6): p. 616-619.
19. Ondrejcek, M., et al., *Step fluctuation spectroscopy of Au(111) by LEEM.* Surface Science, 2005. **574**(2-3): p. 111-122.
20. Ling, W.L., et al., *Herringbone and triangular patterns of dislocations in Ag, Au, and AgAu alloy films on Ru(0001).* Surface Science, 2006. **600**(9): p. 1735-1757.
21. Binnig, G., et al., *7x7 Reconstruction on Si(111) Resolved in Real Space.* Physical Review Letters, 1983. **50**(2): p. 120-123.
22. Ohtani, H., et al., *Scanning Tunneling Microscopy Observations of Benzene Molecules on the Rh(111)-(3x3)(C6h6+2co)Surface.* Physical Review Letters, 1988. **60**(23): p. 2398-2401.
23. Mugele, F., et al., *The influence of tip-sample interaction on step fluctuations on Ag(111).* Surface Science, 1998. **400**(1-3): p. 80-86.
24. Kuipers, L., et al., *Design and Performance of a High-Temperature, High-Speed Scanning Tunneling Microscope.* Review of Scientific Instruments, 1995. **66**(9): p. 4557-4565.
25. Giesen, M., *Step and island dynamics at solid/vacuum and solid/liquid interfaces.* Progress in Surface Science, 2001. **68**(1-3): p. 1-153.
26. KUK, Y., et al., *O Chemisorption on Cu(110) by Scanning Tunneling Microscopy.* Physical Review B, 1990. **41**(18): p. 12393-12402.

27. Wintterlin, J., et al., *Atomic Motion and Mass-Transport in the Oxygen Induced Reconstructions of Cu(110).* Journal of Vacuum Science & Technology B, 1991. **9**(2): p. 902-908.
28. Wolf, J.F., B. Vicenzi, and H. Ibach, *Step Roughness on Vicinal Ag(111).* Surface Science, 1991. **249**(1-3): p. 233-236.
29. Poensgen, M., et al., *Step Dynamics on Ag(111) and Cu(100) Surfaces.* Surface Science, 1992. **274**(3): p. 430-440.
30. LIU, C.L. and J.B. Adams, *Step and Kink Formation Energies on Fcc Metal-Surfaces.* Surface Science, 1993. **294**(3): p. 211-218.
31. Steimer, C., et al., *Experimental determination of step energies from island shape fluctuations: A comparison to the equilibrium shape method for Cu(100), Cu(111), and Ag(111).* Physical Review B, 2001. **6408**(8): p. art. no.-085416.
32. Bondarchuk, O., et al., *Correlation time for step structural fluctuations.* Physical Review B, 2005. **71**(4): p. 045426.
33. Giesen, M. and G.S. Icking-Konert, *Equilibrium fluctuations and decay of step bumps on vicinal Cu(111) surfaces.* Surface Science, 1998. **413**: p. 645-656.
34. Kuipers, L., M.S. Hoogeman, and J.W.M. Frenken, *Step Dynamics on Au(110) Studied with a High-Temperature, High-Speed Scanning Tunneling Microscope.* Physical Review Letters, 1993. **71**(21): p. 3517-3520.
35. Kuipers, L., et al., *Step and Kink Dynamics on Au(110) and Pb(111) Studied with a High-Speed Stm.* Physical Review B, 1995. **52**(15): p. 11387-11397.
36. Pai, W.W., N.C. Bartelt, and J.E. ReuttRobey, *Fluctuation kinetics of an isolated Ag(110) step.* Physical Review B, 1996. **53**(23): p. 15991-15996.
37. Jeong, H.C. and E.D. Williams, *Steps on surfaces: experiment and theory.* Surface Science Reports, 1999. **34**(6-8): p. 171-294.
38. Morgenstern, K., et al., *Brownian-Motion of Vacancy Islands on Ag(111).* Physical Review Letters, 1995. **74**(11): p. 2058-2061.
39. Morgenstern, K., G. Rosenfeld, and G. Comsa, *Decay of two-dimensional Ag islands on Ag(111).* Physical Review Letters, 1996. **76**(12): p. 2113-2116.
40. Morgenstern, K., et al., *Kinetics of fast island decay on Ag(111).* Physical Review B, 2001. **63**(4): p. 045412.

41. Wulff, G. and M. Kristallogr, Mineral., 1901. **34**: p. 449.
42. Yasunaga, H. and A. Natori, *Electromigration on Semiconductor Surfaces.* Surface Science Reports, 1992. **15**(6-7): p. 205-280.
43. Yang, Y.N., E.S. Fu, and E.D. Williams, *An STM study of current-induced step bunching on Si(111).* Surface Science, 1996. **356**(1-3): p. 101-111.
44. Thurmer, K., et al., *Onset of step antibanding instability due to surface electromigration.* Physical Review Letters, 1999. **83**(26): p. 5531-5534.
45. Park, H., et al., *Fabrication of metallic electrodes with nanometer separation by electromigration.* Applied Physics Letters, 1999. **75**(2): p. 301-303.
46. Taychatanapat, T., et al., *Imaging electromigration during the formation of break junctions.* Nano Letters, 2007. **7**(3): p. 652-656.
47. Tao, C.G., et al., *Generalized survival in step fluctuations.* Physical Review E, 2007. **76**: p. 021601.
48. Tao, C.G., et al., *Surface morphology and step fluctuations on Ag nanowires.* Surface Science, 2007(in press).
49. Tao, C., et al., *STEP FLUCTUATIONS ON AG(111) SURFACES WITH C60.* Physical Review B, 2006. **73**(12): p. 125436.
50. Tao, C., et al., *Metal-Molecule Interface Fluctuations.* Nano Letters, 2007. **7**: p. 1495-1499.
51. Stasevich, T.J., et al., *Impurity decoration for crystal shape control: C60 on Ag(111).* 2007(submitted).
52. Xu, B., et al., *Chiral symmetry breaking in two-dimensional C60-ACA intermixed systems.* Nano Letters, 2005. **5**(11): p. 2207.
53. Tao, C., et al., *ACA boundary fluctuations.* 2007(in preparation).
54. Bardeen, J., *Tunnelling from a Many-Particle Point of View.* Physical Review Letters, 1961. **6**(2): p. 57-&.
55. Landau, L.D. and L.M. Lifshitz, *Quantum Mechanics*. 3 ed. 1981: Butterworth-Heinemann.
56. Chen, C.J., *Introduction to Scanning Tunneling Microscopy*. 1993: Oxford University Press.

57. Wiesendanger, R., *Scanning Probe Microscopy and Spectroscopy: Methods and Applications* 1994: Cambridge University Press.
58. Tersoff, J. and D.R. Hamann, *Theory and Application for the Scanning Tunneling Microscope.* Physical Review Letters, 1983. **50**(25): p. 1998-2001.
59. Tersoff, J. and D.R. Hamann, *Theory of the Scanning Tunneling Microscope.* Physical Review B, 1985. **31**(2): p. 805-813.
60. Stroscio, J.A. and W.J. Kaiser, *Scannng tunneling microscopy*. 1994: Academic Press Limited.
61. Zhirnov, V.V. and R.K. Cavin, *Molecular electronics: Chemistry of molecules or physics of contacts?* Nature Materials, 2006. **5**(1): p. 11-12.
62. Ramachandran, G.K., et al., *A bond-fluctuation mechanism for stochastic switching in wired molecules.* Science, 2003. **300**(5624): p. 1413-1416.
63. Xu, B.Q. and N.J.J. Tao, *Measurement of single-molecule resistance by repeated formation of molecular junctions.* Science, 2003. **301**(5637): p. 1221-1223.
64. Wang, W.Y., T.H. Lee, and M.A. Reed, *Electronic transport in molecular self-assembled monolayer devices.* Proceedings of the Ieee, 2005. **93**(10): p. 1815-1824.
65. Ke, S.H., H.U. Baranger, and W.T. Yang, *Models of electrodes and contacts in molecular electronics.* Journal of Chemical Physics, 2005. **123**(11): p. 114701.
66. Jeong, H.C. and E.D. Williams, *Steps on surfaces: experiment and theory.* Surface Science Reports, 1999. **34**(6-8): p. 175-294.
67. Rost, M.J., S.B. van Albada, and J.W.M. Frenken, *How asymmetric islands become symmetric.* Physical Review Letters, 2001. **86**(26): p. 5938-5941.
68. Kodambaka, S., et al., *Absolute TiN(111) step energies from analysis of anisotropic island shape fluctuations.* Physical Review Letters, 2002. **88**(14): p. 146101.
69. Le Goff, E., L. Barbier, and B. Salanon, *Time-space height correlations of thermally fluctuating 2-d systems. Application to vicinal surfaces and analysis of STM images of Cu(115).* Surface Science, 2003. **531**(3): p. 337-358.
70. Ondrejcek, M., et al., *Step fluctuation studies of surface diffusion and step stiffness for the Ni(111) surface.* Physical Review B, 2006. **73**(3): p. 035418.

71. Redner, S., *A Guide to First-Passage Processes*. 2001: Combridge University Press.
72. Merikoski, J., et al., *Temporal and spatial persistence of combustion fronts in paper.* Physical Review Letters, 2003. **90**(2): p. 024501.
73. Leite, V.B.P., et al., *Single molecule electron transfer dynamics in complex environments.* Physical Review Letters, 2005. **95**(11): p. 118301.
74. Goychuk, I. and P. Hanggi, *Ion channel gating: A first-passage time analysis of the Kramers type.* Proceedings of the National Academy of Sciences of the United States of America, 2002. **99**(6): p. 3552-3556.
75. Chen, J.Z.Y., H.K. Tsao, and Y.J. Sheng, *Diffusion-controlled first contact of the ends of a polymer: Crossover between two scaling regimes.* Physical Review E, 2005. **72**(3): p. 031804.
76. Krug, J., *Power laws in surface physics: the deep, the shallow and the useful.* Physica a-Statistical Mechanics and Its Applications, 2004. **340**(4): p. 647-655.
77. Constantin, M., et al., *Persistence in nonequilibrium surface growth.* Physical Review E, 2004. **69**(6): p. 061608.
78. Constantin, M. and S. Das Sarma, *Mapping spatial persistent large deviations of nonequilibrium surface growth processes onto the temporal persistent large deviations of stochastic random walk processes.* Physical Review E, 2004. **70**(4): p. 041602.
79. Dougherty, D.B., et al., *Persistence exponents for step edge diffusion.* Surface Science, 2003. **527**(1-3): p. L213-L218.
80. Constantin, M., et al., *Infinite family of persistence exponents for interface fluctuations.* Physical Review Letters, 2003. **91**(8): p. 086103.
81. Dougherty, D.B., et al., *Experimental persistence probability for fluctuating steps.* Physical Review Letters, 2002. **89**(13): p. 136102.
82. Krug, J., et al., *Persistence exponents for fluctuating interfaces.* Physical Review E, 1997. **56**(3): p. 2702-2712.
83. Constantin, M., S. Das Sarma, and C. Dasgupta, *Spatial persistence and survival probabilities for fluctuating interfaces.* Physical Review E, 2004. **69**(5): p. 051603.

84. Dougherty, D.B., et al., *Sampling-time effects for persistence and survival in step structural fluctuations.* Physical Review E, 2005. **71**(2): p. 021602.
85. Constantin, M. and S. Das Sarma, *Generalized survival in equilibrium step fluctuations.* Physical Review E, 2004. **69**(5): p. 052601.
86. Baski, A.A. and H. Fuchs, *Epitaxial-Growth of Silver on Mica as Studied by Afm and Stm.* Surface Science, 1994. **313**(3): p. 275-288.
87. Levlin, M. and A. Laakso, *Evaporation of silver thin films on mica.* Applied Surface Science, 2001. **171**(3-4): p. 257-264.
88. Dasgupta, C., in preparation.
89. Majumdar, S.N. and C. Dasgupta, *Spatial survival probability for one-dimensional fluctuating interfaces in the steady state.* Physical Review E, 2006. **73**(1): p. 011602.
90. Dasgupta, C., et al., *Survival in equilibrium step fluctuations.* Physical Review E, 2004. **69**(2): p. 022101.
91. Webb, M.B., et al., *Surface Step Configurations under Strain - Kinetics and Step Step Interactions.* Surface Science, 1991. **242**(1-3): p. 23-31.
92. Men, F.K., W.E. Packard, and M.B. Webb, *Si(100) Surface under an Externally Applied Stress.* Physical Review Letters, 1988. **61**(21): p. 2469-2471.
93. Barabasi, A.-L. and H.E. Stanley, *Fractal Concepts in Surface Growth*. 1995: Cambridge University, Cambridge.
94. Basch, H., R. Cohen, and M.A. Ratner, *Interface geometry and molecular junction conductance: Geometric fluctuation and stochastic switching.* Nano Letters, 2005. **5**(9): p. 1668-1675.
95. Tao, C., et al., *Metal-Molecule Interface Fluctuations.* Nano Letters, 2007. **7**.
96. Giesen, M., C. Steimer, and H. Ibach, *What does one learn from equilibrium shapes of two-dimensional islands on surfaces?* Surface Science, 2001. **471**(1-3): p. 80-100.
97. Duan, X.F., et al., *Indium phosphide nanowires as building blocks for nanoscale electronic and optoelectronic devices.* Nature, 2001. **409**(6816): p. 66-69.
98. Cui, Y. and C.M. Lieber, *Functional nanoscale electronic devices assembled using silicon nanowire building blocks.* Science, 2001. **291**(5505): p. 851-853.

99. Tao, A., et al., *Langmuir-Blodgett silver nanowire monolayers for molecular sensing using surface-enhanced Raman spectroscopy.* Nano Letters, 2003. **3**(9): p. 1229-1233.
100. Hunyadi, S.E. and C.J. Murphy, *Bimetallic silver-gold nanowires: fabrication and use in surface-enhanced Raman scattering.* Journal of Materials Chemistry, 2006. **16**(40): p. 3929-3935.
101. Murphy, C.J., et al., *One-dimensional colloidal gold and silver nanostructures.* Inorganic Chemistry, 2006. **45**(19): p. 7544-7554.
102. Berry, V., et al., *Deposition of CTAB-terminated nanorods on bacteria to form highly conducting hybrid systems.* Journal of the American Chemical Society, 2005. **127**(50): p. 17600-17601.
103. Murphy, C.J., et al., *Anisotropic metal nanoparticles: Synthesis, assembly, and optical applications.* Journal of Physical Chemistry B, 2005. **109**(29): p. 13857-13870.
104. Orendorff, C.J., et al., *Surface-enhanced Raman spectroscopy of self-assembled monolayers: Sandwich architecture and nanoparticle shape dependence.* Analytical Chemistry, 2005. **77**(10): p. 3261-3266.
105. Toimil-Molares, M.E., et al., *Fragmentation of nanowires driven by Rayleigh instability.* Applied Physics Letters, 2004. **85**(22): p. 5337-5339.
106. Ma, D.D.D., et al., *Small-diameter silicon nanowire surfaces.* Science, 2003. **299**(5614): p. 1874-1877.
107. Caswell, K.K., C.M. Bender, and C.J. Murphy, *Seedless, surfactantless wet chemical synthesis of silver nanowires.* Nano Letters, 2003. **3**(5): p. 667-669.
108. Terada, Y., et al., *Pulse injection of carbon nanotubes onto a H-terminated Si(100) surface.* Japanese Journal of Applied Physics Part 1-Regular Papers Short Notes & Review Papers, 2003. **42**(7B): p. 4739-4742.
109. Morgenstern, K., et al., *Kinetics of fast island decay on Ag(111).* Physical Review B, 2001. **63**(4): p. art. no.-045412.
110. Stasevich, T.J., et al., *Adsorbate induced island shape change: C60 on Ag(111).* 2007: p. in preparation.

111. Sun, Y.G., et al., *Polyol synthesis of uniform silver nanowires: A plausible growth mechanism and the supporting evidence.* Nano Letters, 2003. **3**(7): p. 955-960.
112. Feibelman, P.J., *Systematics of Adsorption near a Step.* Physical Review Letters, 1992. **69**(10): p. 1568-1571.
113. Ichimiya, A., et al., *Decay of silicon mounds: Scaling laws and description with continuum step parameters.* Physical Review Letters, 2000. **84**(16): p. 3662-3665.
114. Bid, A., A. Bora, and A.K. Raychaudhuri, *Observation of large low-frequency resistance fluctuations in metallic nanowires: Implications on its stability.* Physical Review B, 2005. **72**(11): p. 113415.
115. Zhang, C.H., F. Kassubek, and C.A. Stafford, *Surface fluctuations and the stability of metal nanowires.* Physical Review B, 2003. **68**(16): p. 165414.
116. Williams, E.D., et al., *Temporal step fluctuations on a conductor surface: Electromigration force, surface resistivity and low-frequency noise.* New Journal of Physics, 2007: p. submitted.
117. Hoogeman, M.S., et al., *Surface energetics and thermal roughening of Ag(115) studied with STM movies.* Physical Review B, 1996. **53**(20): p. 13299-13302.
118. Richards, H.L., et al., *Extraction of step-re pulsion strengths from terrace width distributions: statistical and analytical considerations.* Surface Science, 2000. **453**(1-3): p. 59-74.
119. Tao, C., et al., *Step fluctuations on Ag(111) surfaces with C-60.* Physical Review B, 2006. **73**(12): p. 125436.
120. Yu, B.D. and M. Scheffler, *Anisotropy of growth of the close-packed surfaces of silver.* Physical Review Letters, 1996. **77**(6): p. 1095-1098.
121. Pai, W.W., et al., *Island diffusion and coarsening on metal (100) surfaces.* Physical Review Letters, 1997. **79**(17): p. 3210-3213.
122. Jeong, H.-C. and E.D. Williams, *Steps on surface: experiment and theory.* Surface Science Reports, 1999. **34**: p. 171-294.
123. Altman, E.I. and R.J. Colton, *Determination of the Orientation of C-60 Adsorbed on Au(111) and Ag(111).* Physical Review B, 1993. **48**(24): p. 18244-18249.
124. Sakurai, T., et al., *Adsorption of Fullerenes on Cu(111) and Ag(111) Surfaces.* Applied Surface Science, 1995. **87-8**(1-4): p. 405-413.

125. Altman, E.I. and R.J. Colton, *The Interaction of C-60 with Noble-Metal Surfaces.* Surface Science, 1993. **295**(1-2): p. 13-33.
126. Lu, X., et al., *Spatially mapping the spectral density of a single C-60 molecule.* Physical Review Letters, 2003. **90**(9): p. 096802.
127. Giesen, M., et al., *Frizzed Appearance of Steps in Tunnel Microscopy on Cu(100) and Vicinal Cu(11N) Surfaces.* Journal of Vacuum Science & Technology A-Vacuum Surfaces and Films, 1992. **10**(4): p. 2597-2599.
128. Dasgupta, C., et al., *Survival in equilbrium step fluctuations.* Physical Review E, 2004. **69**: p. 022101.
129. Bartelt, N.C. and R. Tromp, *Low-energy electron microscopy of step mobilities on Si(001).* Physical Review B, 1996. **54**: p. 11731.
130. Stasevich, T.J., et al., *Low-temperature orientation dependence of step stiffness on {111} surfaces.* Physical Review B, 2005. **71**(24): p. 245414.
131. Ondrejcek, M., et al., *Fluctuation spectroscopy of step edges on Pt(111) and Pd(111).* Physical Review B, 2005. **72**(8): p. 085422.
132. Zia, R.K.P., *Exact Equilibrium Shapes of Ising Crystals on Triangular Honeycomb Lattices.* Journal of Statistical Physics, 1986. **45**(5-6): p. 801-813.
133. Pai, W.W., N.C. Bartelt, and J.E. Reutt-Robey, *Fluctuation kinetics of an isolated Ag(110) step.* Physical Review B, 1996. **53**(23): p. 15991-15996.
134. Wang, L. and H. Cheng, *Rotation, translation, charge transfer, and electronic structure of C-60 on Cu(111) surface.* Physical Review B, 2004. **69**(4): p. 045404.
135. Wang, L. and H. Cheng, *Density functional study of the adsorption of a C-60 monolayer on Ag(111) and Au(111) surfaces.* Physical Review B, 2004. **69**(16): p. 165417.
136. Fartash, A., *Orientational Epitaxy of High-Quality C-60 Films on Ag(111).* Physical Review B, 1995. **52**(11): p. 7883-7886.
137. Feibelman, P.J., *Surface-diffusion mechanism versus electric field: Pt/Pt(001).* Physical Review B, 2001. **64**(12): p. 125403.
138. Feibelman, P.J., *Accelerated mound decay at adjacent kinks on Cu(111).* Surface Science, 2001. **478**(1-2): p. L349-L354.

139. Guo, Q., X. Sun, and R.E. Palmer, *Structural dynamics induced by self-assembled monolayers on Au(111).* Physical Review B, 2005. **71**(3): p. 035406.
140. Tans, S.J., A.R.M. Verschueren, and C. Dekker, *Room-temperature transistor based on a single carbon nanotube.* Nature, 1998. **393**(6680): p. 49-52.
141. Guo, X.F., et al., *Covalently bridging gaps in single-walled carbon nanotubes with conducting molecules.* Science, 2006. **311**(5759): p. 356-359.
142. Kushmerick, J.G., A.S. Blum, and D.P. Long, *Metrology for molecular electronics.* Analytica Chimica Acta, 2006. **568**(1-2): p. 20-27.
143. Garner, C.M. and E.M. Vogel, *Metrology challenges for emerging research devices and materials.* Ieee Transactions on Semiconductor Manufacturing, 2006. **19**(4): p. 397-403.
144. Haiss, W., et al., *Precision control of single-molecule electrical junctions.* Nature Materials, 2006. **5**: p. 995-1002.
145. Di Ventra, M., S.T. Pantelides, and N.D. Lang, *First-principles calculation of transport properties of a molecular device.* Physical Review Letters, 2000. **84**(5): p. 979-982.
146. Yu, L.H., C.D. Zangmeister, and J.G. Kushmerick, *Structural contributions to charge transport across Ni-octanedithiol multilayer junctions.* Nano Letters, 2006. **6**(11): p. 2515-2519.
147. Frenken, J.W.M., R.J. Hamers, and J.E. Demuth, *Thermal Roughening Studied by Scanning Tunneling Microscopy.* Journal of Vacuum Science & Technology a-Vacuum Surfaces and Films, 1990. **8**(1): p. 293-296.
148. Schlosser, D.C., et al., *Determination of step free energies from island shape fluctuations on metal surfaces.* Physical Review Letters, 1999. **82**(19): p. 3843-3846.
149. Wen, J.M., et al., *Diffusion of Large 2-Dimensional Ag Clusters on Ag(100).* Physical Review Letters, 1994. **73**(19): p. 2591-2594.
150. Bartelt, N.C., R.M. Tromp, and E.D. Williams, *Step Capillary Waves and Equilibrium Island Shapes on Si(001).* Physical Review Letters, 1994. **73**(12): p. 1656-1659.

151. Schmid, A.K., N.C. Bartelt, and R.Q. Hwang, *Alloying at surfaces by the migration of reactive two-dimensional islands.* Science, 2000. **290**(5496): p. 1561-1564.
152. Khare, S.V. and T.L. Einstein, *Brownian motion and shape fluctuations of single-layer adatom and vacancy clusters on surfaces: Theory and simulations.* Physical Review B, 1996. **54**(16): p. 11752-11761.
153. Szalma, F., H. Gebremariam, and T.L. Einstein, *Fluctuations, line tensions, and correlation times of nanoscale islands on surfaces.* Physical Review B, 2005. **71**(3): p. 035422.
154. Khare, S.V., et al., *Determining absolute orientation-dependent step energies: a general theory for the Wulff-construction and for anisotropic two-dimensional island shape fluctuations.* Surface Science, 2003. **522**(1-3): p. 75-83.
155. Hashizume, T., et al., *Intramolecular Structures of C60 Molecules Adsorbed on the Cu(111)-(1x1) Surface.* Physical Review Letters, 1993. **71**(18): p. 2959-2962.
156. Stasevich, T.J., et al., in preparation, 2006.
157. Mulligan, A., et al., *Going beyond the physical: Instilling chirality onto the electronic structure of a metal.* Angewandte Chemie-International Edition, 2005. **44**(12): p. 1830-1833.
158. Humblot, V., et al., *Local and global chirality at surfaces: Succinic acid versus tartaric acid on Cu(110).* Journal of the American Chemical Society, 2004. **126**(20): p. 6460-6469.
159. Fasel, R., M. Parschau, and K.H. Ernst, *Chirality transfer from single molecules into self-assembled monolayers.* Angewandte Chemie-International Edition, 2003. **42**(42): p. 5178-5181.
160. Spillmann, H., et al., *Hierarchical assembly of two-dimensional homochiral nanocavity arrays.* Journal of the American Chemical Society, 2003. **125**(35): p. 10725-10728.
161. Lorenzo, M.O., et al., *Extended surface chirality from supramolecular assemblies of adsorbed chiral molecules.* Nature, 2000. **404**(6776): p. 376-379.

162. Kuhnle, A., et al., *Chiral recognition in dimerization of adsorbed cysteine observed by scanning tunnelling microscopy.* Nature, 2002. **415**(6874): p. 891-893.
163. Switzer, J.A., et al., *Enantiospecific electrodeposition of a chiral catalyst.* Nature, 2003. **425**(6957): p. 490-493.
164. Gellman, A.J., J.D. Horvath, and M.T. Buelow, *Chiral single crystal surface chemistry.* Journal of Molecular Catalysis a-Chemical, 2001. **167**(1-2): p. 3-11.
165. Sholl, D.S., A. Asthagiri, and T.D. Power, *Naturally chiral metal surfaces as enantiospecific adsorbents.* Journal of Physical Chemistry B, 2001. **105**(21): p. 4771-4782.
166. Horvath, J.D. and A.J. Gellman, *Enantiospecific desorption of chiral compounds from chiral Cu(643) and achiral Cu(111) surfaces.* Journal of the American Chemical Society, 2002. **124**(10): p. 2384-2392.
167. Horvath, J.D. and A.J. Gellman, *Enantiospecific desorption of R- and S-propylene oxide from a chiral Cu(643) surface.* Journal of the American Chemical Society, 2001. **123**(32): p. 7953-7954.
168. Attard, G.A., *Electrochemical studies of enantioselectivity at chiral metal surfaces.* Journal of Physical Chemistry B, 2001. **105**(16): p. 3158-3167.
169. Ray, K., et al., *Asymmetric scattering of polarized electrons by organized organic films of chiral molecules.* Science, 1999. **283**(5403): p. 814-816.
170. Polcik, M., et al., *Circular dichroism in core level photoemission from an adsorbed chiral molecule.* Physical Review Letters, 2004. **92**(23): p. -.
171. Verbiest, T., et al., *Strong enhancement of nonlinear optical properties through supramolecular chirality.* Science, 1998. **282**(5390): p. 913-915.
172. Sheats, J.R., et al., *Organic electroluminescent devices.* Science, 1996. **273**(5277): p. 884-888.
173. Fuhrmann, T. and J. Salbeck, *Organic materials for photonic devices.* Mrs Bulletin, 2003. **28**(5): p. 354-359.
174. Theobald, J.A., et al., *Controlling molecular deposition and layer structure with supramolecular surface assemblies.* Nature, 2003. **424**(6952): p. 1029-1031.

175. de Wild, M., et al., *A novel route to molecular self-assembly: Self-intermixed monolayer phases.* Chemphyschem, 2002. **3**(10): p. 881-885.
176. Sowerby, S.J., W.M. Heckl, and G.B. Petersen, *Chiral symmetry breaking during the self-assembly of monolayers from achiral purine molecules.* Journal of Molecular Evolution, 1996. **43**(5): p. 419-424.
177. Stepanow, S., et al., *Programming supramolecular assembly and chirality in two-dimensional dicarboxylate networks on a Cu(100) surface.* Nano Letters, 2005. **5**(5): p. 901-904.
178. Bondarchuk, O., et al., *Correlation time for step structural fluctuations.* Physical Review B, 2005. **71**(4): p. -.
179. Lu, X.H., et al., *Spatially mapping the spectral density of a single C-60 molecule.* Physical Review Letters, 2003. **90**(9): p. -.
180. Limbach, H.H. and J. Manz, *Hydrogen transfer: Experiment and theory.* Berichte Der Bunsen-Gesellschaft-Physical Chemistry Chemical Physics, 1998. **102**(3): p. 289-291.
181. Barth, J.V., et al., *Stereochemical effects in supramolecular self-assembly at surfaces: 1-D versus 2-D enantiomorphic ordering for PVBA and PEBA on Ag(111).* Journal of the American Chemical Society, 2002. **124**(27): p. 7991-8000.
182. Xu, B., et al., Unpublished.
183. Rissanen, K., *Very Large Container Molecules.* Angewandte Chemie-International Edition, 2005. **44**(24): p. 3652-3654.
184. Hecht, S., *Welding, organizing, and planting organic molecules on substrate surfaces - Promising approaches towards nanoarchitectonics from the bottom up.* Angewandte Chemie-International Edition, 2003. **42**(1): p. 24-26.
185. Sariciftci, N.S., et al., *Semiconducting Polymer-Buckminsterfullerene Heterojunctions - Diodes, Photodiodes, and Photovoltaic Cells.* Applied Physics Letters, 1993. **62**(6): p. 585-587.
186. Kobayashi, S., et al., *Control of carrier density by self-assembled monolayers in organic field-effect transistors.* Nature Materials, 2004. **3**(5): p. 317-322.

187. Donhauser, Z.J., et al., *Conductance switching in single molecules through conformational changes.* Science, 2001. **292**(5525): p. 2303-2307.
188. Halik, M., et al., *Low-voltage organic transistors with an amorphous molecular gate dielectric.* Nature, 2004. **431**(7011): p. 963-966.
189. Barth, J.V., G. Costantini, and K. Kern, *Engineering atomic and molecular nanostructures at surfaces.* Nature, 2005. **437**(7059): p. 671-679.
190. Kozlov, V.G., et al., *Laser action in organic semiconductor waveguide and double-heterostructure devices.* Nature, 1997. **389**(6649): p. 362-364.
191. Einstein, T.L., *Multisite Lateral Interactions and Their Consequences.* Langmuir, 1991. **7**(11): p. 2520-2527.
192. Price, S.L., *Quantifying intermolecular interactions and their use in computational crystal structure prediction.* Crystengcomm, 2004. **6**: p. 344-353.
193. Hooks, D.E., T. Fritz, and M.D. Ward, *Epitaxy and molecular organization on solid substrates.* Advanced Materials, 2001. **13**(4): p. 227.
194. Schunack, M., et al., *Anchoring of organic molecules to a metal surface: HtBDC on Cu(110).* Physical Review Letters, 2001. **86**(3): p. 456-459.
195. Noh, J., et al., *High-resolution STM and XPS studies of thiophene self-assembled monolayers on Au(111).* Journal of Physical Chemistry B, 2002. **106**(29): p. 7139-7141.
196. Lee, S., et al., *Self-assembled monolayers on Pt(111): Molecular packing structure and strain effects observed by scanning tunneling microscopy.* Journal of the American Chemical Society, 2006. **128**(17): p. 5745-5750.
197. Akkerman, H.B., et al., *Towards molecular electronics with large-area molecular junctions.* Nature, 2006. **441**(7089): p. 69-72.
198. Tulevski, G.S., et al., *Attaching organic semiconductors to gate oxides: In situ assembly of monolayer field effect transistors.* Journal of the American Chemical Society, 2004. **126**(46): p. 15048-15050.
199. Xu, B., et al., *Chiral symmetry breaking in two-dimensional C-60-ACA intermixed systems.* Nano Letters, 2005. **5**(11): p. 2207-2211.

200. Xu, B., et al., *Coverage dependent supramolecular structures: C-60 : ACA monolayers on Ag(111).* Journal of the American Chemical Society, 2006. **128**(26): p. 8493-8499.
201. Xu, B., et al., *Morphology selected molecular architecture: Acridine carboxylic acid monolayers on Ag(111).* Journal of Physical Chemistry B, 2006. **110**(3): p. 1271-1276.
202. Wang, X.S., et al., *Terrace-Width Distributions on Vicinal Si(111).* Physical Review Letters, 1990. **65**(19): p. 2430-2433.
203. Wei, J., et al., *Step-Height Mixtures on Vicinal Si(111) Surfaces.* Physical Review Letters, 1992. **68**(26): p. 3885-3888.
204. Thurmer, K., et al., *Step dynamics in 3D crystal shape relaxation.* Physical Review Letters, 2001. **8718**(18): p. -186102.
205. Dougherty, D.B., et al., *Experimental persistence probability for fluctuating steps.* Physical Review Letters, 2002. **89**(13): p. -.
206. Giesenseibert, M. and H. Ibach, *On the Time Structure of Tunneling Images of Steps.* Surface Science, 1994. **316**(1-2): p. 205-222.
207. Lyubinetsky, I., et al., *Dynamics of step fluctuations on a chemically heterogeneous surface of Al/Si(111)-(root 3x root 3).* Physical Review B, 2002. **66**(8): p. -85327.
208. Bondarchuk, O., et al., *Correlation time for step structural fluctuations.* Physical Review B, 2005. **71**(4): p. -045426.
209. Avron, J.E., et al., *Roughening Transition, Surface-Tension and Equilibrium Droplet Shapes in a Two-Dimensional Ising System.* Journal of Physics a-Mathematical and General, 1982. **15**(2): p. L81-L86.
210. Evans, D. and J. Reutt-Robey, 2007(unpublished work).
211. Einstein, T.L., *Interactions between adsorbate particles*. Handbook of Surface Science, ed. W.N. Unertl. Vol. 1. 1996, Amsterdam: Elsevier. 577-650.
212. Williams, E.D., et al., *Thermodynamics and Statistical-Mechanics of the Faceting of Stepped Si(111).* Surface Science, 1993. **294**(3): p. 219-242.
213. Wortis, M., *Equilibrium crystal shapes and interfacial phase transitions.* 1988: p. 367-428.

214. Van Moere, R., H.J.W. Zandvliet, and B. Poelsema, *Two-dimensional equilibrium island shape and step free energies of Cu(001).* Physical Review B, 2003. **67**(19): p. -193407.
215. Kodambaka, S., et al., *Two-dimensional island dynamics: Role of step energy anisotropy.* Surface Science Reports, 2006. **60**(5): p. 55-77.
216. Liu, Q. and J.D. Weeks, 2007(unpublished work).
217. Giesen, M., G.S. Icking-Konert, and H. Ibach, *Interlayer mass transport and quantum confinement of electronic states.* Physical Review Letters, 1999. **82**(15): p. 3101-3104.
218. Pierre-Louis, O. and T.L. Einstein, *Electromigration of single-layer clusters.* Physical Review B, 2000. **62**(20): p. 13697-13706.
219. Baier, S., S. Dieluweit, and M. Giesen, *Step and island dynamics on Cu(111), Ag(111) and Au(100) electrodes in electrolyte.* Surface Science, 2002. **502**: p. 463-473.